UNIVERSITY OF COPENHAGEN

Lea Halser

Neutrino Fluence of Gamma-Ray Bursts for Arbitrary Viewing Angles

Master's Thesis

Date: August 30, 2019

Supervisor: Asst. Prof. Markus Ahlers
University of Copenhagen, Niels Bohr Institute

Master's Thesis

Neutrino Fluence of Gamma-Ray Bursts for Arbitrary Viewing Angles

Date: August 30, 2019

Lea Halser
Supervisor: Asst. Prof. Markus Ahlers
University of Copenhagen, Niels Bohr Institute

Submission Date: August 20, 2019
Date of the Defence: August 28, 2019
External Censor: Prof. Steen Lynge Hannestad

The Niels Bohr International Academy

ABSTRACT

Gamma-ray bursts are one of the most luminous explosions in the Universe. For a short period of seconds, these transient sources at cosmological distances outshine all visible gamma-ray sources in the Universe. The progenitors of gamma-ray bursts are cataclysmic events like the core collapse of massive stars or mergers of neutron stars. Such events are predicted to emit large amounts of energies in the form of gravitational waves, photons, neutrinos, and cosmic rays. The first two of these signals have been observed in coincidence recently and found to originate from a neutron star merger. This detection established gamma-ray bursts as multi-messenger sources. As neutrinos are produced in cosmic-ray photon interactions in gamma-ray burst environments, they would serve as a smoking gun signal for high-energy cosmic rays being accelerated in gamma-ray bursts. Thus, they would reveal one possible source of high-energy cosmic rays, which are still unknown these days. In this thesis, we study the joint gamma-ray and neutrino emission of internal shocks under consideration of the relative orientation of the jet axis to the observer and a defined opening angle of the jet. We focus on top-hat jets, which are the widely used jet models. However, our formalism can be easily extended to general jet structures, as we show in this thesis. We present a simple analytic model that allows rescaling previous model prediction based on on-axis emission.

ACKNOWLEDGEMENTS

I would like to express great thankfulness to my supervisor Markus. Thank you for your endless patience and your enthusiastic guidance. You always found the time to answer all my requests and helped me finding my way throughout this year. I will keep this period of working with you in the best memory.
I would also like to thank the IceCube group in Copenhagen. Thanks that I could be a part of this team, it was a great pleasure for me. Special thanks to all who have proofread this work and have provided helpful feedback: Markus, Timo, Taus, Ida, Ania, Charlotte, and Maga.
With the submission and defence of this work, my time in Copenhagen comes to an end. I thank all people I have met in these two wonderful years at the Niels-Bohr Institute, but also beyond. I can not imagine how this time would have been so inspiring and motivating without you. Many thanks to all my friends back home in beautiful Bavaria, I am looking forward to lifting the "Masskrüge" at the Oktoberfest and to celebrate the reunion!
Timo, I can not describe in words how grateful I am to have you in my life (so I will not try, at least not here ;)).
And finally, thank you and endless love to my family. With your support and belief in me, I have managed to submit this thesis here in Copenhagen. Thank you for all your support, guidance and love.

Copenhagen, August 2019

COMMENT ON THE CONVENTIONS

Unless otherwise stated, we use natural units in this work

$$\hbar = c = \epsilon_0 = \mu_0 = 1\,.$$

From this follows that among other quantities, energy, momentum, mass and time are expressed in powers of electron Volt (eV),

$$1 \text{ eV} = 1.602 \times 10^{-19} \text{ J}\,.$$

One eV corresponds to the energy that an electron receives when when it passes through a potential difference of one Volt. This unit is commonly used in particle physics, e.g. is the mass of a proton $\sim$1 GeV. Furthermore, we use Heaviside-Lorentz units with

$$\alpha = e^2/(4\pi) \simeq 1/137\,.$$

In astrophysical context, parsec (pc) and light year (ly) are typically used as units for distances:

$$1 \text{ pc} = 3.26 \text{ ly} = 3.1 \times 10^{16} \text{ m}\,.$$

One parsec is the distance that corresponds to the adjacent side in a right-angled triangle, where the opposite side is one astronomical unit (1 AU = 1.49×10^{11} m) and the defined angle is one arcsecond. A light year is simply the distance, light travels in one year.

CONTENTS

1 INTRODUCTION

1.1 MULTI-MESSENGER ASTRONOMY

Multi-messenger astronomy revolutionizes classic astronomy, which only observes electromagnetic radiation, It extends the range of observable signals by gravitational waves, cosmic rays, and neutrinos. The detection of gravitational waves and astrophysical neutrinos are great achievements of the last years and herald the advent for a new and promising era of astronomy. The big advantage of multi-messenger astronomy over traditional astronomy is that the additional messengers lighten up the fraction of the high-energy and far-distant Universe, that is opaque to photons, and for which we were blind until just a few years ago.

Classical astronomy with visible light on the night sky has its beginnings more than 5000 years ago, the time of the ancient Babylonians (1895 BC – 539 BC) and Egyptians (3032 BC - 30 BC) [55]. The wavelength range from 380 to 750 nm can be seen with the naked eye but is only a tiny fraction of the electromagnetic spectrum that can be observed with modern technology. For the longest time in history, astronomy relied only on visible light. In the second half of the 20th century, the range of astronomy began to expand with new developments, such as radio astronomy with technology inherited from second world war [55]. With this new technique, astrophysical objects, such as pulsars and quasars were found. As soon as satellites could reach the space above the Earth's atmosphere, the range of wavelengths, which became accessible for astronomers, extended to infrared, UV, X- and γ-rays [55]. By the early 21st century, telescopes cover a range in wavelengths from several meters down to picometer (10^{-12} m) scales. Traditional astronomy with photons is very successful and taught us many things about the Universe, but it has its limitations. For high energies in the PeV range[1], photons travelling through space undergo scattering with the cosmic microwave background (CMB)[2] and produce electron-positron pairs via $\gamma\gamma_{\mathrm{CMB}} \rightarrow e^{+}e^{-}$. Thus, the Universe is not transparent for such high-energetic photons travelling long distances and astronomy based on electromagnetic radiation is blind at these scales [48].

More than a hundred years ago, Victor Hess opened up another new branch of astronomy. He detected ionizing radiation and its increasing flux with altitude in the Earth's atmosphere. This radiation was later found to be caused by cosmic rays [31]. Cosmic Rays (CRs) are ionized, highly-energetic nuclei coming from sources of non-terrestrial origin. They are mostly protons with a small fraction being α-particles and heavier nuclei [34]. Around 1000 CRs per square meter bombard the Earth's atmosphere every second, of which most are coming from sources within our galaxy [34]. They undergo scattering in the atmosphere and produce secondary particles, mostly muons, and mesons, which can be detected as particle showers in large air-shower telescope arrays on the Earth's

1 MeV=10^{6} eV, GeV=10^{9} eV, TeV=10^{12} eV, PeV=10^{15} eV, EeV=10^{18} eV
2 T_{CMB}= 2.73 K, E_{CMB} = 2.4 $\times 10^{-4}$ MeV

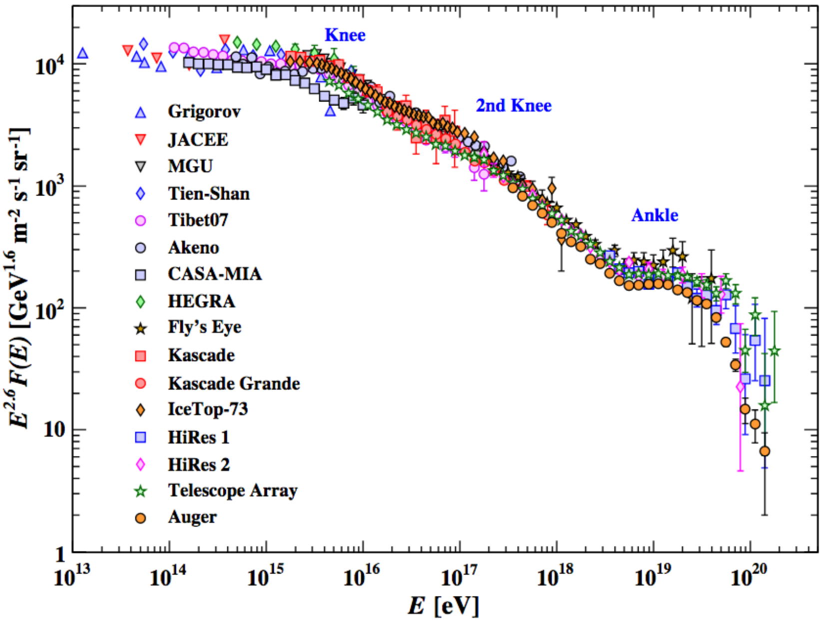

FIG. 1. Cosmic ray spectrum with knee, second knee and ankle feature, spanning the 10 TeV to 100 EeV range. CRs with energies reaching the first knee at $\sim 10^{15}$ eV are of galatic origin, while high-energy CRs above the ankle at $\sim 10^{18}$ eV are believed to be cosmological [59].

surface. The spectrum of CRs detected at Earth, spans over more than 11 orders of magnitude in energy. The most energetic CRs are shown in Fig. 1. The spectrum follows a power-law behaviour with notable features, the *knee*, the *second knee* and the *ankle*. Low-energy CRs, up until the first knee are most likely originating from sources within the galaxy. The area between the first knee and the ankle is rather mysterious. It is assumed that this region can be explained by at least two effects, a change in the nuclei composition of CRs towards heavier elements and propagation effects [34]. Above 10^{18} eV, the gyroradius of the protons is larger than our galaxy, thus they must be produced and accelerated by extra-galactic sources. But, the acceleration mechanisms and sites are unknowns in CR physics, which makes the ultra-high-energy CRs (above 10^{18} eV) one of the most mysterious phenomena in recent days. Finally, the CR spectrum at high energies is limited by interactions with the CMB, which is known as the Greisen-Zatsepin-Kuzmin (GZK) effect and occurs to happen at CR energies above 10^{20} [34]. Due to their charged nature, CRs are deflected by magnetic fields in our galaxy and in the interstellar medium, which makes it impossible to pinpoint back to their sources.

The existence of high-energy CRs is a direct motivation for neutrino astronomy. It is expected that the CRs interact with gas or radiation before arriving at Earth. By this, neutrinos are produced either right at the source (*astrophysical* neutrinos), in interactions with the background light in the Universe (*cosmogenic* neutrinos) or in the Earth's atmosphere (*atmospheric* neutrinos). In such CR-γ interactions, mesons are created primarily, which eventually decay into neutrinos. Neutrinos are not deflected by magnetic fields and also interact only rarely with the background radiation or matter fields. Thus, they propagate undisturbed through space and point back straight to their sources. Therefore, they are of great interest when it comes to the identification of the sources of CR and neutrino acceleration [33]. Neutrinos are the perfect messenger, to observe the high-energy Universe, but due to their extremely weak interactions, it is rather challenging to detect them. Huge detector volumes have to be operated to observe significant fluxes of high-energy astrophysical neutrinos. Only 6 years ago, in 2013, such an successful observation happened for the first time [48]. Additionally, a rather newly available messenger, gravitational waves, entered the field of multi-messenger astronomy in 2015, which allow us to make use of multiple signals and their correlations [6].

The observation of the first gravitational wave signal in 2015 (GW150914) was a great breakthrough in physics [6]. It confirmed Einstein's prediction of the existence of gravitational waves due to the principles of general relativity and was awarded the Nobel-price in 2017. With the two kilometer-scaled L-shaped LIGO and Virgo interferometers, one can measure the effect of propagating gravitational waves, causing compression and stretching of space-time. The detectors are sensitive to length changes in the order of incredible 10^{-19} m, which is only possible due to the great technological achievements combined in the detectors [6, 27]. The first signal in 2015 was found to be caused by a binary blackhole (BH) merger [7]. Not only BH mergers but also a binary neutron star merger has been detected by LIGO, for the first time in 2017 [9]. Gravitational waves are also predicted to come from a neutron star - blackhole merger, but such an event has not been observed yet. Within the first two observing runs between 2015 and 2017 (with a break in observing time 2016), LIGO and Virgo have been observing a total of 10 BH mergers, and one neutron star binary merger [11]. By early August 2019 roughly 20 additional gravitational wave event candidates have been detected within the third run O3, which started in April 2019 [1].

Combining multiple messengers gives us access to an increased amount of knowledge about the sources they are coming from, because the available energy range increased largely [48]. These days are pretty exciting, as we are now able to study diverse high-energy sources actively in terms of two or more different messengers. The most favoured multi-messenger sources are transient or flaring sources, like active galactic nuclei, blazars, gamma-ray bursts, supernovae, and compact binary merger [48].

The two most notable break-through events in multi-messenger astronomy were detected only within one year, 2017. In that year, LIGO detected the first gravitational waves coming from a neutron star binary merger, GW170817. Exciting enough, this event was found to be coincident with the detection of an electromagnetic counterpart, a short γ-ray burst. This burst, GRB 170817A, was detected by the Fermi Gamma-ray Burst Monitor (Fermi GBM) [8]. Only one month later, IceCube sent out an alert to telescopes around the world immediately after detecting the high-energy neutrino candidate IceCube-170922A. The alert triggered the Fermi Large Array Telescope (Fermi LAT), which found a known γ-ray source, the flaring blazar TXS 0506+056. The location of the blazar coincided with the region IceCube determined as the origin of the neutrino. Also the γ-ray telescope MAGIC detected signals corresponding to the source [5].
These two milestone events were the first successful observations in terms of high-energy multi-messenger astronomy. The next steps are just ahead of us, as the improved sensitivity of the gravitational wave detectors and plans for neutrino experiment upgrades will increase the number of detections significantly. Another ground-breaking observation,

the observation of the three messengers simultaneously, is thus surely not far away in the future.

1.2 MOTIVATION AND CONTEXT

One of the most promising sources to be observed in γ-rays, gravitational waves and neutrinos are gamma-ray bursts (GRBs). GRBs are one of the most luminous explosions in the Universe. Possible progenitors are compact mergers, which emit gravitational waves. The resulting central engine from the merger powers emission jets, which emit γ-rays. Also, protons can be accelerated to high energies within the jet, and are thus detectable as high-energy cosmic rays. From the CR-γ interactions in the jet environment, neutrinos are assumed to be produced [64]. While γ-rays and gravitational waves have been detected coincidentally in the GW170817/GRB170817 event [8, 10], CRs and neutrinos are the missing piece. The successful detection of neutrinos would be the "smoking gun" signal for cosmic ray production, as neutrinos can only be emitted from a site where high-energetic hadrons interact with photons.

The gamma-ray and GW event in 2017 triggered intensive follow-up searches for neutrinos [16, 48]. But unfortunately, no neutrinos were found in coincidence with this event. GRB parameters were inferred from the electromagnetic and gravitational wave signals to give upper limits on the neutrino emission. The predicted emission models were all found to be below the detection sensitivity of the involved neutrino experiments IceCube and ANTARES [16]. The non-observation of neutrinos was eventually explained by a large off-axis angle between the emission axis and the line-of-sight. The effect of off-axis emission was studied in [39, 48, 56], among others.

This thesis follows earlier attempts to give a realistic theoretical description of the neutrino flux coming from a GRB source. We attempt to include commonly used GRB physics and make it more general by including off-axis emission and characteristics of the jet properties, such as its opening angle. For our theoretical descriptions, we follow the strategies presented in [16, 21, 57, 65]. We derive a new, simple analytical model that allows rescaling of previous on-axis model predictions. Additionally, we show how these neutrino fluxes would look like if observed on Earth. The work presented in this thesis defines the missing neutrino piece of the GRB puzzle in an improved way. The puzzle itself contains several parts, beginning from the progenitors of GRBs, its central engine which powers the jets and eventually the messengers that can be observed from GRBs: γ-rays, gravitational waves and soon also neutrinos, which probe the existence and acceleration of ultra-high energy cosmic rays. The GRB puzzle with the missing neutrino piece is illustrated in Fig. 2.

Before deriving the mathematical description of neutrino fluxes from GRBs in section 4, we will give a theoretical introduction into neutrino physics (section 2) and the phenomenology of gamma-ray bursts (section 3). After setting up the analytical framework, we use this, to show actual neutrino spectra and compare these with earlier results in section 5. Finally, we make use of our approach to give new predictions for neutrinos from the GW170817 event. Section 6 is devoted to the conclusive summary and a brief outlook on future aspects that would reveal further interesting insights into GRB neutrino physics. A scientific paper on detailed studies of the jet structure, which is following the arguments presented in this thesis, is attached at the end of this work.

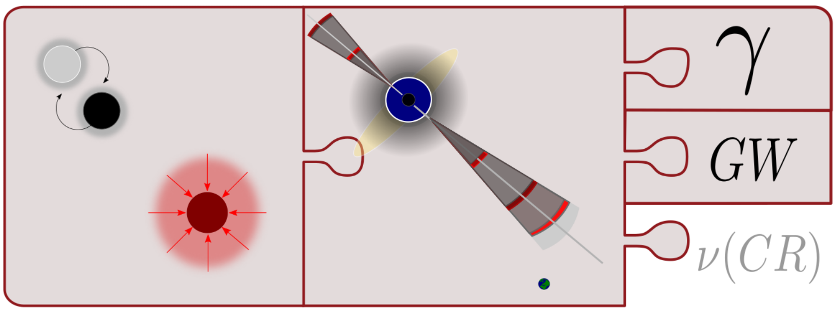

FIG. 2. GRB-puzzle with progenitors (left), the central engine and its emission (center) and the observable signals, γ-rays, gravitational waves (GW) and neutrinoss which probe for cosmic rays. The missing piece in this puzzle are the neutrinos as we have not yet observed them in coincidence with the other messengers.

2 THE MISSING MESSENGER: NEUTRINOS FROM GRB ENVIRONMENTS

Gamma-ray bursts are characterized as extreme environments in multiple ways: high temperatures, high particle densities and the appearance of high energy (HE) particles such as photons and baryons, which eventually lead to HE and ultra HE (UHE) neutrinos and cosmic ray particles. We refer to HE for energies above 10^{18} eV, while UHE describes energies higher than 10^{18} eV. In section 2.1, we first give a brief overview of neutrinos in the Standard Model of elementary particle physics and their properties such as mass, oscillations, and interactions. In S section 2.2, we explain how neutrinos are produced in photo-hadronic interactions in GRB environments. Finally, in section 2.3, we describe the state-of-the-art neutrino detector which is used to look (and wait) for neutrinos from GRBs.

2.1 NEUTRINOS IN THE STANDARD MODEL OF ELEMENTARY PARTICLES

The Standard Model (SM) of elementary particle physics predicts neutrinos to be massless particles. However, experiments showed that neutrino flavours oscillate which gives raise to non-zero neutrino masses. This makes neutrinos one of the most mysterious components of the Standard Model (SM) of elementary particle physics. Neutrinos are neutral leptons that exist in three flavours: electron neutrinos (ν_e), muon neutrinos (ν_μ) and tau neutrinos (ν_τ). They are almost massless and interact only weakly. Due to their small cross sections, neutrinos interact very rarely, and are thus hard to detect and study.

2.1.1 *History of Neutrino Physics*

In 1930, Wolfgang Pauli proposed the existence of neutrinos for the first time. Originally named *neutrons*, the particle was proposed to solve the problem of the seemingly energy-conservation violating β-decay [18]. The β-decay, as we understand it today, is a radioactive process in which an atomic nucleus emits a highly energetic electron via

$$n \to p + e^- + \bar{\nu}_e \,. \tag{2.1}$$

But in 1930, atoms were thought to consist only out of equal numbers of electrons and protons. Therefore, the β decay was assumed to be a two-body decay with only two final state particles, the final nucleus and the emitted electron. Measurements showed that the electron energy spectra from β-decay was continuous and not mono-energetic, as would be expected if the electron was emitted from an atom at rest [18, 51]. To explain this, Pauli suggested that the final decay products of atomic nuclei might not only consist out of protons and electrons (which was the common thought in that period), but also of nearly massless, neutral particles. These particles carry away some of the energy from the β-decay, and thereby cause the continuous energy spectrum that was observed. Two years later, in 1932, James Chadwick discovered a neutral particle and called it *neutron* [18]. Only later it was realized that this particle is too massive to be the neutrino predicted by Pauli. Chadwicks neutron was found to be a strongly interacting component of the atom's nuclei. After this discovery, that atomic nuclei consist out of protons and neutrons, Enrico Fermi suggested, in 1934, that there is indeed a neutral particle present in β-decays. He called this particle the *neutrino*, and it is produced alongside the electron in a decay process [18].

Due to their extremely weak interaction, Fermi proposed that their existence could be investigated by measuring interactions where the final state is completely measurable, e.g. the inverse β-decay $\bar{\nu_e} + p \rightarrow n + e^+$. Neutrinos were discovered via this process by Clyde Cowan and Frederick Reines in 1956. They successfully measured neutrinos from the Savannah River reactor in South Carolina, with a detector consisting of scintillators in a tank of water. The scintillators detected γ-rays from the positron annihilating and the neutron capture on cadmium in the water [18].

Since the 1960s, it was predicted that nuclear fusion processes in the Sun lead to electron neutrinos. In the *pp cycle*,

$$p + p \rightarrow D + e^+ + \nu_e \,, \tag{2.2}$$

$$D + p \rightarrow \ {}^3_2\mathrm{He} + \gamma \,, \tag{2.3}$$

$${}^3_2\mathrm{He} + \ {}^3_2\mathrm{He} \rightarrow \ {}^4_2\mathrm{He} + p + p \,, \tag{2.4}$$

the primary reaction (Eq. 2.2) produces deuterium (D), a positron, and an electron neutrino, which has an energy up to 0.42 MeV [18]. The deuterium interacts again with a proton. In this reaction the light isotope of helium (helium-3 ${}^3_2$He) is produced. The reaction of two of these isotopes creates two protons and a helium-4 isotope. Multiple other processes in the Sun, such as the electron capture of boron-7 (^{7}Be) and the β-decay of boron-8 (^{8}Be), also produce electron neutrinos with energies extending up to 15 MeV [60]. From 1964 onwards, Raymond Davis measured the number of neutrinos coming from the Sun with a radiochemical detector. The detector, based in the Homestake Mine in South Dakota, was a tank, filled with perchloroethylene (C_2Cl_4) [18]. Interactions of electron neutrinos with chlorine atoms in the tank produced radioactive isotopes of argon via inverse β-decay

$$\nu_e + \ {}^{37}_{17}\mathrm{Cl} \rightarrow \ {}^{37}_{18}\mathrm{Ar} + e^- \,. \tag{2.5}$$

The radioactive ${}^{37}_{18}$Ar isotopes were extracted and counted. However, only one third of the predicted amount of neutrinos was detected. This difference in the observed and theoretically predicted amount of neutrinos from the Sun became generally known as the *solar neutrino problem* [18].

A few years after this problem arose, Vladimir Gribov and Bruno Pontecorvo suggested in 1968 that the deficit could be caused by neutrino oscillations. These oscillations change the flavour of a neutrino while the particle propagates through space. If the electron neutrinos changed flavour as they propagated to Earth, the solar neutrino experiments, sensitive only to electron neutrinos, would not detect the whole flux of solar neutrinos.

In the early 2000s, the Sudbury Neutrino Observatory (SNO) confirmed that the total flux of solar neutrinos matched the predictions. This was later interpreted as an indication of neutrino oscillations. SNO was sensitive to the total flux of neutrinos of all flavours via the neutral current (NC) interaction. Additionally, the detector was also sensitive to the distinct ν_e flux via the charged-current (CC) process. Being sensitive to the total flux and one flavour separately was a crucial feature to solve the solar neutrino problem. More information on the experiments and their detection techniques can be found in [18, 60]. The two interactions neutrinos undergo, NC and CC, will be discussed in section 2.1.4.

In 1989, it was ensured that there are exactly three types of active and light neutrino flavours. This was achieved by studying the decay width of the Z^0 boson into the undetectable neutrinos produced in e^+e^- collisions at the Large Electron Collider (LEP) at CERN [18].

The neutrino mass differences and mixing angles, which are needed to guarantee the flavour oscillations, are well-determined parameters in the SM. But the absolute masses and the hierarchy of the masses have so far not been determined. The neutrino sector of the SM contains many unknown aspects, which makes neutrino physics very appealing to the particle physics community. There are great hopes that understanding the full neutrino picture will lead to a deeper understanding of the model describing the elementary particles. The most puzzling questions about neutrinos are whether neutrinos are Majorana or Dirac particles, if there is charge parity (CP) violation in neutrino oscillations, what the absolute masses and their ordering are and how neutrinos gain their mass. These aspects will be discussed in more detail in the following sections.

2.1.2 *The Standard Model of Elementary Particles*

The Standard Model (SM) of particle physics describes the most elementary particles and their interactions with each other. Matter is described by the fermionic (half-integer spin) components, while forces are transmitted by vector-bosons (integer spin). The elementary fermions of the SM are sub-divided into leptons and quarks, based on their charge properties and associated couplings to the bosons, and they exist in three generations. Leptons can further be classified as charged (e^-, μ^-, τ^-) and neutral (ν_e, ν_μ, ν_τ) particles, quarks are categorised into up-type (u, c, t) and down-type (d, s, b) quarks. Every fermion also has an antiparticle with opposite physical charges but the same mass.
The bosons associated with the electroweak force are the massless photon (γ) and the massive Z^0 and $W^\pm$ bosons. The photon couples to charged particles. The $W^\pm$ boson couples only to left-handed multiplets (right-handed anti-multiplets), while the Z^0 lepton couples to left- and right-handed fermions, but with different strength. This chirality-dependence comes from the $V - A$ structure of the charged current weak interaction [60]. Gluons (g) are carriers of the strong force and couple exclusively to quarks. These are the only particles with colour charge in the SM, which is the charge that gluons couple to. With the discovery of the Higgs boson in 2012, the SM was completed. This particle gives mass to the massive bosons through spontaneous symmetry-breaking and to massive fermions through the Yukawa coupling. Only the neutrino mass is not explained by coupling to the Higgs field. The mass of a particle depends on the strength of its coupling to the Higgs field: the heavier the particle, the stronger the coupling [60]. Figure 3 shows all particles of the SM and summarizes important properties.

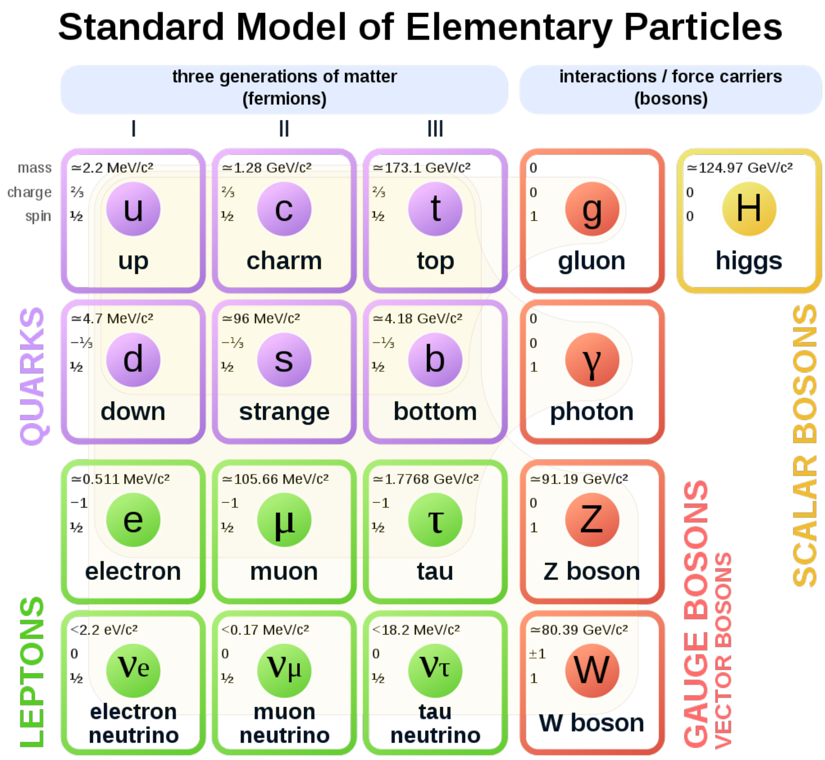

FIG. 3. Standard Model of Particle Physics with 12 fermions, 4 vector-bosons and the Higgs boson [28]. Physical properties as the masses, the electrical charge and spin are given for all particles.

The only fundamental force that is not described by the SM is gravity. Gravitons are predicted to exist but do not appear as a part of the theoretical framework of the SM. Gravity would complete the theory in the sense that all four fundamental forces are included. The coupling strength of gravity is in the order of 10^{-38}, while the weak force is in the order of 10^{-5}, the electromagnetic around 10^{-3}, and the coupling of strong force is at unity at energy scales we are probing. Due to a difference in orders of magnitude of at least 10^{-33}, gravity is negligible when it comes to the description of elementary particles.

The SM is an extremely successful theoretical description of particle physics. It has been in development since the 1950s and has experienced several confirmations and adaptations necessitated by experimental observations. Though largely successful, the SM has some weaknesses which have to be rectified in order to find an “all-inclusive” SM theory. Neutrinos are here of special interest because they only appear as left-handed fermions in the SM and thus do not obtain mass from the Yukawa coupling to the Higgs-field as the other quarks and leptons do in the description of the SM [60]. However, if neutrinos were massless, they would not oscillate, which is contradictory to our experimental results.

2.1.3 *Neutrino Oscillations and Masses*

Neutrinos produced in weak interactions appear in one of three different flavour eigenstates ν_α ($\alpha = e, \mu, \tau$) corresponding to the interacting lepton flavour. The flavour eigenstates are linear superpositions of mass eigenstates and both bases are related via the Pontecorvo-Maki-Nakagawa-Sakata (PMNS) matrix U_{PMNS} [60]

$$|\nu_\alpha\rangle = \sum_i U^*_{\alpha i} |\nu_i\rangle \ . \tag{2.6}$$

This unitary 3×3 matrix is defined by four free parameters, which are the three mixing angles $\theta_{12}, \theta_{23}, \theta_{13}$ and a CP violating Dirac phase δ. It is usually written as [60]

$$U_{\text{PMNS}} = \begin{pmatrix} 1 & 0 & 0 \\ 0 & c_{23} & s_{23} \\ 0 & -s_{23} & c_{23} \end{pmatrix} \begin{pmatrix} c_{13} & 0 & s_{13}e^{-i\delta} \\ 0 & 1 & 0 \\ -s_{13}e^{-i\delta} & 0 & c_{13} \end{pmatrix} \begin{pmatrix} c_{12} & s_{12} & 0 \\ -s_{12} & c_{12} & 0 \\ 0 & 0 & 1 \end{pmatrix} , \tag{2.7}$$

where s_{ij} stands for $\sin(\theta_{ij})$ and c_{ij} for $\cos(\theta_{ij})$. The most recently observed values for these parameters can be found in [30]. Neutrinos could also be Majorana particles, which means they are their own anti-particles. In that case, two additional Majorana phases ϕ_1 and ϕ_2 ($\phi_i \leq 2\pi$) are included in the PMNS matrix and the matrix in Eq. 2.7 has to be multiplied by an additional matrix [18],

$$\begin{pmatrix} 1 & 0 & 0 \\ 0 & e^{i\phi_2/2} & 0 \\ 0 & 0 & e^{i\phi_3/2} \end{pmatrix} . \tag{2.8}$$

The easiest accessible experimental test to probe whether neutrinos are of Dirac or Majorana nature is to study the neutrino-less double β decay. In this process, a nucleon is changing its nuclear charge by two units while emitting two electrons, but no neutrinos [53] via

$$(A, Z) \rightarrow (A, Z + 2) + 2e^- , \tag{2.9}$$

with atomic number Z and mass number A [29]. This process can only be detected, if neutrinos are Majorana particles. In this case, a anti-neutrino from one of the β decays could be absorbed as a neutrino in the other β decay [62]. Therefore, the successful and distinct observation of such a process would clearly reveal neutrinos being Majorana particles. Recently, several experiments are becoming sensitive to their first experimental results and will lead to conclusions within the next years [29].

Let us assume a neutrino of flavour α at time $T = 0$. We can write for the wavefunction

$$|\psi(0)\rangle = |\nu_\alpha\rangle = U^*_{\alpha 1} |\nu_1\rangle + U^*_{\alpha 2} |\nu_2\rangle + U^*_{\alpha 3} |\nu_3\rangle \ . \tag{2.10}$$

With $c = 1$, time and distance L are equal and therefore $L = 0$ at $T = 0$. The wavefunction $|\psi(0)\rangle$ is a superposition of all three mass eigenstates. While it propagates through space, the eigenstates oscillate. When the neutrino is observed after a distance L, the wavefunction collapses and we measure a different neutrino flavour β with a probability of [18]

$$\begin{aligned} P(\nu_\alpha \to \nu_\beta) &= |\langle \nu_\beta | \psi(L) \rangle|^2 \\ &= \left| \sum_i U_{\beta i} e^{-\frac{i m_i^2 L}{2E_\nu}} U^*_{\alpha i} \right|^2 \\ &= \sum_{ij} U^*_{\alpha i} U_{\beta i} U_{\alpha j} U^*_{\beta j} e^{-\frac{i \delta m_{ij}^2 L}{2E_\nu}} \,, \end{aligned} \tag{2.11}$$

where m_i are the absolute neutrino masses, $\delta m_{ij} = m_i^2 - m_j^2$ the mass differences and E_ν is the neutrino energy [18]. The probability of neutrino oscillation depends on the squared neutrino mass differences and not the absolute masses.

In the scope of this work, we consider neutrinos travelling very long distances, as they are produced in GRBs several 10 Mpc away from Earth. With $L \to \infty$ and $\delta m_{ij} = 0$ for $i = j$, Eq. 2.11 can be approximated as

$$\begin{aligned} P(\nu_\alpha \to \nu_\beta) &\simeq \sum_{ij} U^*_{\alpha i} U_{\beta i} U_{\alpha j} U^*_{\beta j} \delta_{ij} \\ &= \sum_i |U_{\alpha i}|^2 |U_{\beta i}|^2 \,. \end{aligned} \tag{2.12}$$

Because of this limit, experiments looking for astrophysical neutrinos from sources at large distances are sensitive to the mixing parameters, but are not sensitive to the neutrino mass differences. With Eq. 2.12 at hand, it is possible to determine the predicted neutrino flavour ratios we measure on Earth, provided the ratio at the source is known.
As we will see in section 2.2, the initial induced neutrino flavour ratio at the GRB source is close to 1:2:0 for $\nu_e : \nu_\mu : \nu_\tau$. With Eq. 2.12, one can calculate, that the ratio changes to roughly 1:1:1 for neutrinos travelling cosmological distances. This comes from the fact that the $\nu_\tau \leftrightarrow \nu_\mu$ mixing is maximal and therefore approximately half of the produced muon neutrinos will end up being detected as tau neutrinos [37, 40]. A common used approximation to derive this is based on the *tribimaximal mixing matrix*, which uses $\sin(\theta_{12}) = 1/\sqrt{3}$, $\sin(\theta_{23}) = 1/\sqrt{2}$, $\theta_{13} = 0$ and $\delta = 0$ in Eq. 2.7 and Eq. 2.12. This gives an exact flavour composition of 1:1:1 for $L \to \infty$. The most recent values from experiments deviate from the ones assumed in the tribimaximal mixing matrix and thus, the flavour composition is not exactly 1:1:1.

The oscillation properties we just presented are valid for neutrinos propagating through vacuum. For neutrinos propagating in matter, deviations from the the vacuum oscillations probabilities are caused by the the Mikheyev–Smirnov–Wolfenstein (MSW) effect. In a medium with large electron density, the electron neutrino (and anti-neutrino) undergoes scattering via neutral-current and charged-current interaction, while the other neutrino flavours only interact via neutral-current interactions with the matter. This causes a difference in the neutrino potential, influencing the neutrino oscillation probabilities [58]. However, this effect is not important for the sake of this project as we assume that the electron densities at the neutrino production sites in GRBs are not large.

The exact neutrino masses are orders of magnitudes smaller than any other elementary particle masses. As they interact extremely weakly, neutrinos are hard to detect, and thus the masses are difficult to determine. Experimental cosmological data suggests that

$$\sum_{i=1}^{3} m_{\nu_i} \lesssim 0.172 \text{ eV}\,, \tag{2.13}$$

which is strongly dependent on the model assumptions [23, 54]. Precision measurements of oscillation properties show that $\delta m^2_{21} \approx 7.5 \times 10^{-5}$ eV^2 and $|\delta m^2_{32}| \approx 2.5 \times 10^{-3}$ eV^2 [59]. The sign of δm^2_{32} is not known. Therefore, the hierarchy of neutrino masses is not determined. Measurements of the endpoint of the electron distribution in tritium β-decay experiments can be used to determine the squared neutrino mass, which has contributions from all three mass eigenstates as [60, 61]

$$m^2_{\nu_e} = \sum_i |U_{ei}|^2 m_i^2\,, \tag{2.14}$$

depending on the PMNS matrix in Eq. 2.7. The Katrin experiment in Karlsruhe has a design sensitivity of 0.2 eV, which will allow precise studies of the electron anti-neutrino mass. Starting in 2020, Katrin will reach its design sensitivity within 3 years of data taking [66].

2.1.4 *Neutrino Interaction in Matter*

Neutrinos interact only weakly in neutral current (NC) and charged current (CC) interactions. Weak interaction is mediated by the neutral Z^0 and charged $W^\pm$ bosons. The two possible vertices for neutrino interactions are [60]

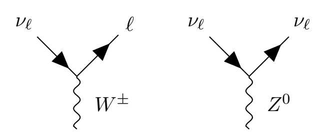

Neutrinos can interact with both leptons and hadrons, but as the cross section of neutrino-nuclei interactions is by far the larger, this will be our focus in the following section. The total CC cross section of neutrinos is a superposition of different processes and is shown in Fig. 4 for neutrinos (left panel) and anti-neutrinos (b).

For neutrinos with energies below 1 GeV, the *quasi-elastic* (QE) CC interaction with nucleons dominates the cross section. In these processes, the neutrino scatters with the nucleon and the proton (or neutron) stays intact. Due to the exchange of a $W^\pm$ boson the proton (neutron) is converted into a neutron (proton) and a lepton of the same flavour as the incoming neutrino is emitted. On quark level, one explains this by the change of an up-type quark into a down-type quark ($\nu_\ell + u \rightarrow \ell + d$) or vice versa. For NC interactions at low energies, the process is denoted as *elastic scattering*, because the exchanged Z^0 boson leaves in the initial nucleus, in its initial quark composition, intact ($\nu + N \rightarrow \nu + N$) [18, 34].

For neutrino energies between 1 and 5 GeV *resonant* (RES) processes dominate the cross section. This process produces an excited state of the nucleus, which is typically a

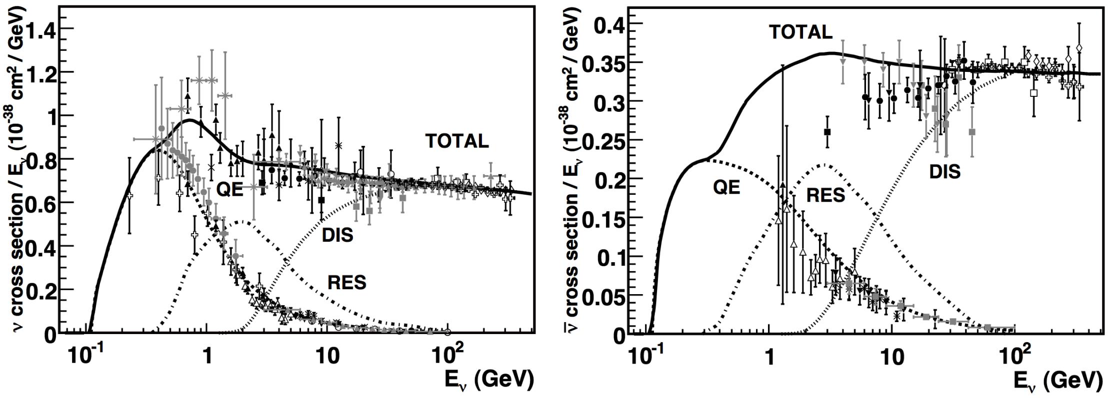

(a) Neutrino cross section

(b) Anti-neutrino cross section

FIG. 4. Total CC neutrino nucleon cross section and individual components: quasi elastic scattering (QE), resonant processes (RES), and deep inelastic scattering (DIS) [32].

baryon state with short lifetime, such as delta resonances (Δ^+). These resonant states decay into mesons [18, 34].

For energies above 5 GeV, neutrinos undergo *deep inelastic scattering* (DIS) with the nucleon. The neutrino energy is large enough to break up the nucleon and a shower of secondary hadrons leaves the vertex as a result of fragmentation. In a NC DIS interaction a neutrino of the same flavour as the incoming neutrino is emitted, while for CC DIS a charged lepton with the same flavour as the initial neutrino is leaving the vertex [18, 34].

The CC cross section for neutrinos is larger than that for anti-neutrinos, as can be seen in Fig. 4. This difference follows from the allowed helicity states for neutrino and anti-neutrino quark interactions. Due to the V-A structure of the CC weak interaction, the left-handed neutrino interacts only with a left-handed quark. Thus, the initial total spin projection sums up to 0. On the other hand, anti-neutrinos appear only in right-handed helicity states. This means, that the initial state includes the right-handed anti-neutrino and a left-handed quark, thus two different helicities. Due to the mixed helicity initial state, an additional $\left(\frac{1}{2}(1+\cos(\theta^*))\right)^2$ term has to be included in the cross section determination for anti-neutrino quark interactions. This additional term leads to a difference of roughly 1/3 between neutrino and anti-neutrino cross section after averaging over the scattering angle [60]. For higher energies, this difference can be neglected, as the neutrino energy is sufficient to break up the proton and to interact with sea quarks of the nucleon, and thus also with anti-quarks [15].

For most experiments that detect high energy neutrinos, the energies are sufficiently high that only deep inelastic scattering needs to be considered. Because of the small cross sections of neutrinos, large detectors are required. In such detectors, the neutrinos interact with the nucleons of the atoms in the detector material.

Even though interactions with hadrons have generally a larger cross section than leptonic interactions, there is one important exception. The *Glashow resonance* describes anti electron-neutrino scattering with an electron, where an on-shell intermediate W^-

boson is produced, $\bar{\nu}_e + e^- \rightarrow W^- \rightarrow \bar{\nu}_i + \ell_i^-$, with $i = e, \mu, \tau$ [20, 35]. For this process to happen, the neutrino energy has to meet the resonance energy of $E_\nu = m_W^2/2m_e =$ 6.3 PeV. The cross section for the leptonic Glashow interaction for a neutrino with this energy is several times larger than the hadronic interaction cross section [32].

2.2 NEUTRINO PRODUCTION IN PHOTO-HADRONIC INTERACTIONS

In 1997, the idea of GRBs as sources for UHE neutrinos was proposed for the first time [64]. The production of neutrinos in GRB environments is assumed to happen mostly due to proton-photon ($p\gamma$) interactions. The dominant process is the creation of a Δ^+ resonance via photon capture of the proton. Δ^+ is an excited state of the proton with a mass of $m_{\Delta^+} \simeq 1232$ MeV and a lifetime of $\tau_{\Delta^+} \simeq 5.63 \times 10^{-24}$s [59]. The resonance decays into a nucleon and a pion with a branching ratio of 99.4%, where the relative ratio between $p + \pi^0$ and $n + \pi^+$ is 2:1. Direct pion-production via $p + \gamma \rightarrow n + \pi^+$ and multipion production has the effect that the probability for the production of a neutral and charged pion channel from the $p\gamma$ interaction becomes approximately equal [67]. The neutrino production from $p\gamma$ interactions appears via

$$\begin{aligned} p + \gamma \rightarrow \Delta^+ &\rightarrow p + \pi^0 \\ &\qquad\quad \hookrightarrow \gamma\gamma \end{aligned} \tag{2.15}$$

$$\begin{aligned} &\rightarrow n + \pi^+ \\ &\qquad\quad \hookrightarrow \mu^+ + \nu_\mu \\ &\qquad\qquad \hookrightarrow e^+ + \nu_e + \overline{\nu}_\mu . \end{aligned} \tag{2.16}$$

Equation 2.15 shows the neutral pion decaying into two photons. This process has a branching ratio of 98.82% and other decay processes as $\pi^0 \rightarrow e^+e^-\gamma$ are strongly suppressed. The resulting proton from the resonance decays into a final state with π^0, and can again interact with a photon, until its energy is too small to create a Δ^+. The required center-of-mass energy for $\Delta^+$to be produced is $s = m_p^2 + 2E_\gamma m_p \simeq m_{\Delta^+}$ in the proton's rest frame. From this we obtain the condition $E_\gamma E_p \simeq 0.32$ GeV for the Δ^+ production in the GRB rest frame.

The other possible decay of Δ^+, shown in Eq. 2.16 produces a charged pion π^+. The positive pion decays with a branching ratio of 99.99% into a anti-muon and a muon neutrino. The pion decay into an $e^+\nu_e$ pair is suppressed due to the fact that the decay width scales with the lepton mass squared, and $m_\mu > m_e$. The muon from the Δ^+ decays into an electron, an electron neutrino, and a muon anti-neutrino. Through the process in Eq. 2.16, three neutrinos are produced.

The Δ^+ resonance is the dominating process for the $p\gamma$ interaction at small photon energies. Figure 5 shows the total $p\gamma$ cross section with its individual contributions for the full energy range. For photon energies below a few GeV, the wavelength of the photon is of the same order of magnitude as the proton. Therefore, the photons couple to the hadron and excited *resonance states* (Δ, N) are formed, of which the Δ^+ is the most dominant. The baryon resonances are most likely to decay hadronically with subsequent

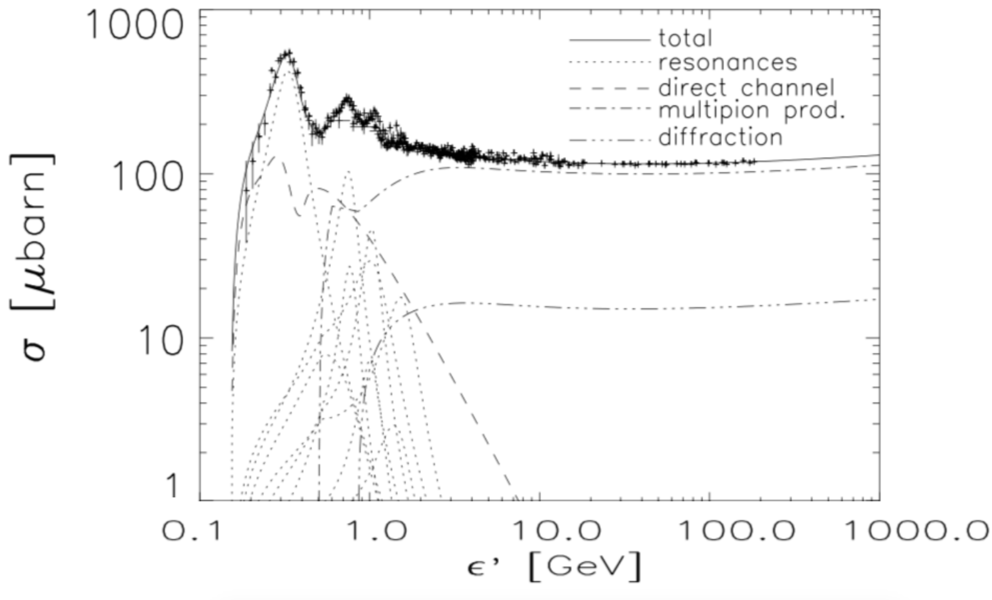

FIG. 5. Total $p\gamma$ interaction cross section with individual components as resonace production, direct pion production, and production of pions via vector mesons (multipion and diffration) as a function of the photon energy [47].

decays into pions and eventually neutrinos, as shown for the Δ^+ resonance in Eq. 2.16 [18, 67].

Direct pion production occurs around the same energy range, but with less contribution than the resonant processes. Pions are directly produced via processes such as $p\gamma \to n\pi^+$ and $p\gamma \to \Delta^{++}\pi^-$. In these processes, the pion is created at the primary vertex together with a baryon [47].

At higher energies, the cross section is dominated by *multipion* production and *diffractive processes*, which describe the inelastic and elastic scattering of vector mesons such as ϕ, ω and ρ via the exchange of quasi-particles. The final states of such processes can involve multiple hadrons, including mesons as pions and kaons. These mesons further decay into neutrinos [47].

As the neutrinos are not only produced through pion production and decay, the ratio of 1:2:0 for $\nu_e : \nu_\mu : \nu_\tau$ is only an approximation. Better results can be achieved with numerical simulations, which include the full $p\gamma$ interaction chain, as we will use in this work.

2.3 Detection of neutrinos with IceCube

Various different methods can be used to detect neutrinos depending on the energy range and the purpose of the neutrino detection. Radiochemical detectors were the first experiments to measure the total rate of neutrinos coming from the Sun via ν_e capture and detecting the decay of the excited atoms. But, they are only practical to measure the total rate of electron neutrinos. Other types of detectors are based on liquid scintillators, which allow for precise determination of location and energy, however, only for low energy neutrinos, e.g. coming from reactors.

Large volume Cherenkov detectors are used for high energy neutrinos. The cross section for neutrino-nucleon interactions is found to be in the order of femtobarn (10^{-39} cm^2) for neutrinos with energies in the TeV to PeV energy range. Combining this with target densities of $N_A \times V/\mathrm{cm}^3$ it can be shown [1], that for the detection of at least one neutrino per year, detector volumes of km^3 sizes are necessary [13]. One stunning example for such a gigantic detector is the IceCube Neutrino Observatory at the South Pole [36].

2.3.1 *Detector Properties*

IceCube is a gigaton Cherenkov detector located near the geographic South Pole on Antarctica. It has been operating in full configuration since 2011. At depths of 1450 to 2450 km below the surface, a total of 5160 detection units are deployed in the clear ice. These digital optical modules (DOMs) are attached to 78 strings with horizontal spacing of 125 m and with vertical distancing of 17 m [4]. IceCube is a multi-purpose detector with several components, which extend the detectors application beyond astrophysical observations. IceTop, which is a detector array located at the surface of IceCube, consists out of 81 stations to detect CR air showers and serves as a veto and calibration component with an energy threshold of 300 TeV. Eight strings with less spacing are deployed in the clearest ice in the center of IceCube. This more densely instrumented detector area, named DeepCore, is sensitive to neutrinos with low energies down to 10 GeV, enabling the study of neutrino oscillations. IceCube itself is sensitive to neutrino energies above 100 GeV [4]. Figure 6 shows the detector schematically with all sub-detectors.

2.3.2 *Event Signatures*

If a neutrino interacts with a nucleon in the ice, it will produce secondary particles through NC or CC interactions. These secondary particles are highly energetic, and travel faster than the speed of light in ice. This leads to the emission of Cherenkov photons, which can be detected with the photo-multiplier tubes of the DOMs in the detector grid. The DOMs register arrival times and the amount of incoming photons. Using the collective data of all the DOMs, particle tracks can be reconstructed, arrival directions estimated and the primary neutrino energy determined. NC interactions result typically in a detectable particle shower for all neutrino flavours, but leptons from CC interactions show different signatures depending on their lepton flavour

The high-energy electron from a ν_e CC interaction in matter radiates a bremsstrahlung photon, which decays into an e^+e^- pair [60]. This process continues and produces a shower of electrons, positrons and photons. The cascade develops until the energy of the

1 Avogadro constant $N_A = 6.022 \times 10^{23}$ mol^{-1}

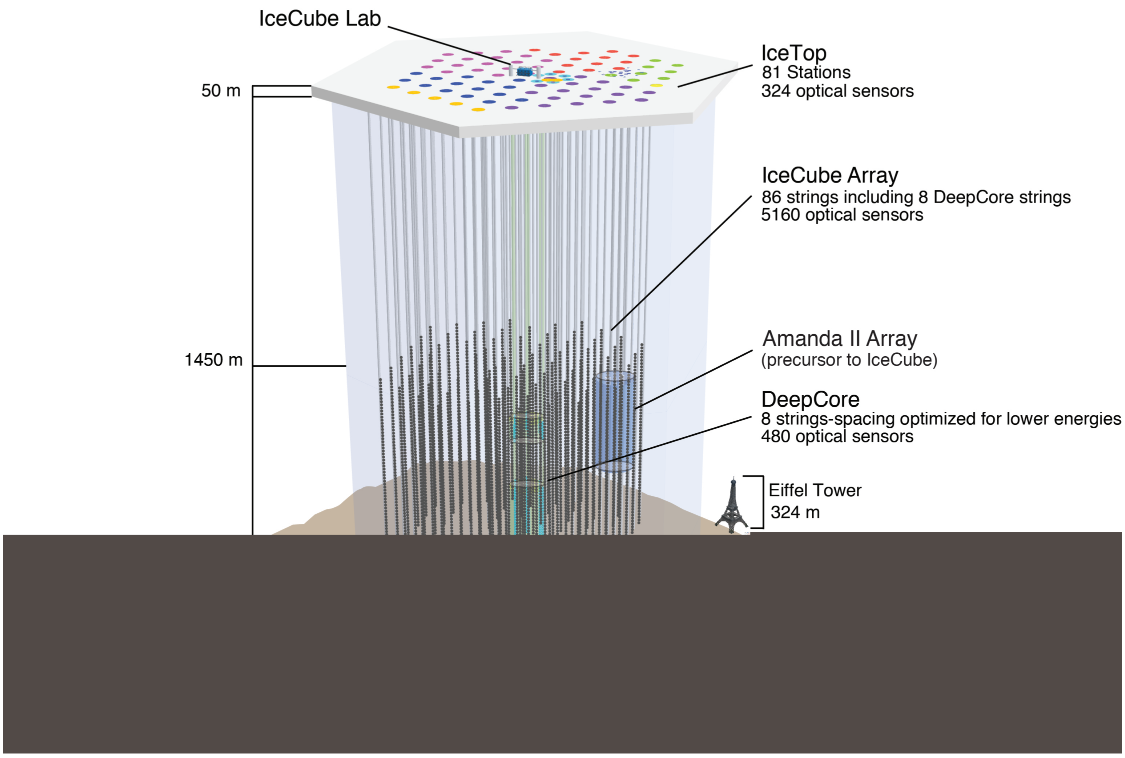

FIG. 6. Illustration of the IceCube detector with the subdetector DeepCore, the precursor detector Amanda and the surface air shower array IceTop. DeepCore is an area within IceCube where the strings are deployed more densely to increase the sensitivity. IceTop detects cosmic ray air showers and is used for calibration activities [36]. Image taken from [26]

particles is below the critical energy for which ionization is the dominant energy loss term [60]. Such a *cascade* event can be seen in Fig. 7b.

For τ leptons from ν_τ CC interactions, a *double bang* event can be registered. One shower is generated by the fragmentation of the nucleon at the interaction point, a second shower after some travel distance of the τ when it decays and produces another cascade of particles. This pattern can only be detected for τ leptons with high-enough energies to travel long enough that the two cascades can be resolved separately in the DOM grid. Due to time-dilation for relativistic particles, the extended lifetime of the tau lepton allows it to travel further. This means that for energies of 1 PeV the tau lepton travels $\gamma c \tau_\tau \approx 50$m [4]. For an illustration of a double-bang event see Fig. 7c.

Muon neutrinos leave tracks that can extent up to several kilometers. They are heavier than electrons and are therefore not subject to strong energy losses via bremsstrahlung. Their penetration length is by far longer and therefore, muons propagating through the ice generate showers along their trajectory until all their energy is deposited in the ice [4]. A *track-like* event is simulated in Fig. 7a.

In summary, one can conclude that all NC interactions and the ν_e CC interaction result in shower-like events, while CC ν_μ events are detected as cascade events, and CC ν_τ as

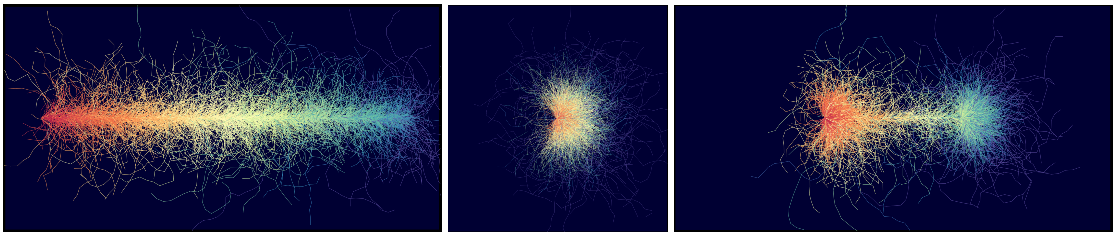

(a) Track-like event (b) Cascade event (c) Double-bang event

FIG. 7. Event signatures from simulation of emitted Cherenkov photons [4]. Each line corresponds to one photon. The colour scheme refers to arrival times: red denotes earlier photons, blue are the ones that are registered at later times.

double-bang events, if their energy is high enough. Examples from simulation are shown in Fig. 7.
The angular resolution for neutrinos is in general better for track-like events than for cascade events. The energy resolution is better for shower events, since all their energy is deposited in the detector, unless they are created at the edges of the detector. The muons might leave the detector or be produced outside of the detector volume and therefore a certain amount of the total energy stays undetected [4].

As mentioned in section 2.1.4, the Glashow resonance enhances the leptonic electron anti-neutrino cross section over its corresponding hadronic cross section. Therefore, such an event is likely to be detected in IceCube and can be identified by its deposited energy matching the characteristic value of 6.3 PeV[20].

High energetic neutrinos events above 100 TeV benefit from the fact that the background rate is negligible. For lower energies, the main background events are caused by neutrinos and muons from CR interactions in the Earth's atmosphere. The Earth is constantly bombarded with CRs, which are mainly protons. They interact in the atmosphere and produce pions and kaos, which decay into neutrinos. IceCube detects events at a rate 10^{11} per year [4]. Most of these events are found to be muons from atmospheric interactions. Every one in a million event is caused from an actual neutrino event. Of these roughly 10^5 high-energy neutrino events, most are induced by CR interactions in the atmosphere [4]. The atmospheric background decreases with increasing event energy, which makes high energy neutrinos from astrophysical sources very clean in terms of background. Every year, a total in the order of 10 high-energy neutrino events is detected [25].

2.3.3 *Astrophysics with IceCube*

In 2011 and 2012, two extra-galactic neutrino events in IceCube with energies above the PeV scale were observed for the first time [3]. Initially only a hint, they were later interpreted as evidence of high-energy neutrinos from extra-galactic sources [2]. Until 2013, a total of 28 high-energy neutrino events, covering energies between 30 and 1200 TeV were identified, which marked the discovery of an astrophysical neutrino flux on Earth.

Up to these days roughly 10 high-energy neutrinos yearly with energies up to several PeV have been reported by the IceCube Collaboration [25]. Among these events was the notably successful detection of a neutrino from a blazar. In 2017, IceCube detected a very high energy neutrino with an energy of 290 TeV. The neutrino observatory was able to localize the source and sent alerts to telescopes around the Earth. Following the alert, the neutrino was found to originate from the blazar TXS 0506+056 [5]. This coincident observation of a neutrino with γ-rays from an identified source was an important milestone for multi-messenger astronomy. This source, the Sun, and the supernova explosion SN1987A in the Large Magellanic Cloud in 1987 [22] are the only known astrophysical sources of high-energy neutrinos so far. In addition to GRBs, it is believed that galactic supernova remnants and extra-galactic structures like active galactic nuclei (AGN) and galaxies with intense star-formation are also sources of high energy astrophysical neutrinos.

3 GAMMA-RAY BURSTS

Gamma-Ray Bursts (GRBs) are the most luminous explosions in our Universe. GRBs are transient sources, which emit an enormous amount of energy within a few seconds. During their emission period, they are the brightest objects in the Universe. This energy is emitted in the form of γ-rays, GWs, neutrinos and possibly CRs. While γ-rays and GWs have been detected successfully, no CR or neutrino observation has been linked conclusively to a GRB event. The emission of gravitational waves was confirmed by the detection of the coincidental observation of the gravitational wave event GW170817 and the short γ-ray bust GRB170817A. Even though multiple neutrino experiments were carefully looking for neutrinos, no neutrino-observation corresponding to GW170817 was identified. The detection of neutrinos from GRBs would not only reveal great insights about the physics of GRBs, but would also add another milestone to multi-messenger astronomy.

3.1 DISCOVERY OF GRBS

GRBs were detected for the first time during the cold war in the late 60's by the series U.S. military satellites *Vela* as short bursts of highly energetic γ-rays coming from outer space [42, 67]. The satellites were operated to detect nuclear detonations caused by nuclear tests in the Soviet Union and were therefore equipped with X-ray and γ-ray detectors. In 1967, the satellites detected signals, which could not be identified as spectra from nuclear weapons. It turned out that the first GRB from an astrophysical source was detected [67].

The following historical summary draws heavily from the sources [46, 67]. Since the 1990s, several space-based missions were launched with the aim to bring light into the nature of GRBs. One of the first of such missions, the Burst and Transient Source Experiment (BATSE) instrument launched 1991 on board of NASA's Compton Gamma-Ray Observatory (CGRO), brought first important insights into GRBs. The γ-ray flashes were found to be isotropically distributed across the sky. From this observation, it was concluded, that their sources are extragalactic, at cosmological distances. A major insight was that GRBs can be divided into two categories based on their duration: long and short duration bursts, with a distinctive time scale of around 2 seconds. Figure 8 shows the distribution of durations for 1234 detected GRBs in the first five years after CGRO was launched [45]. During its 9 years of active operating time, BATSE detected and catalogued a total of 2704 GRBs.

With the *Beppo*-SAX satellite, launched six years later in 1997, it was possible to measure the redshift and determine the host galaxy of a GRB. Therefore, it was possible to confirm that GRBs signals are coming from cosmological distances. Afterglow emission was studied in more detail during this period and constraints on the physics in GRBs

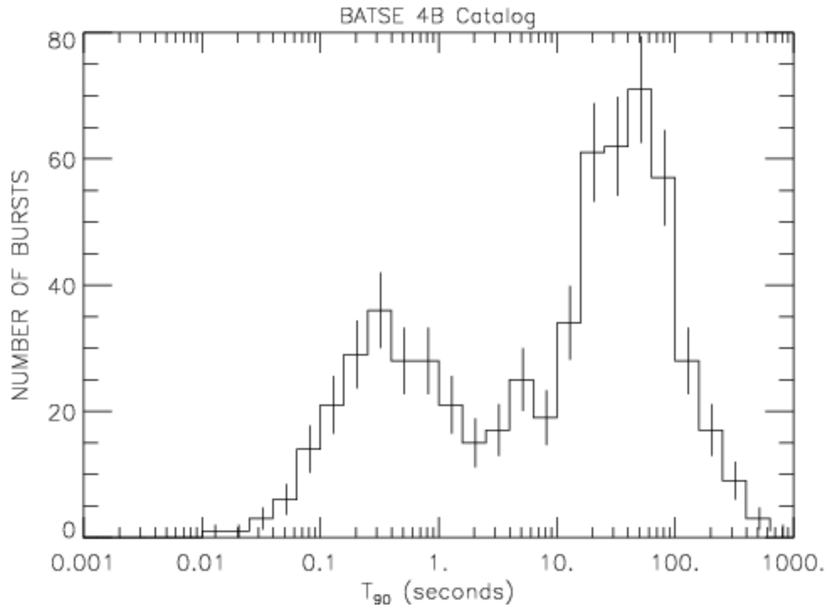

FIG. 8. Distribution for the duration (in seconds) of 1234 GRBs detected with the BATSE instrument on board the CGRO satellite [45]. Short GRBs are distributed around 0.3 seconds, while long GRBs are $\sim$ 30 seconds on average. The two categories are overlapping at $\sim$2 seconds. This set of data is from the BATSE 4B catalogue [50].

could be set. A great success was the identification of sources emitting long GRBs with supernovae Type Ic, which correspond to the death of massive stars [67].

In 2004, the Swift satellite was launched into space and is still operating. The mission has so far been extremely successful in terms of GRB decoding. It became clear that short and long GRBs do not have the same sources, but also that their distinction can not be made as clear as assumed previously. With Swift, GRB afterglows could finally be observed very precisely and the sources localized. Specifically, it became possible to measure the prompt γ-ray burst followed by the transition phase and afterglow. X-ray flares following the primary prompt γ-ray emission gave first hints that the central engine has a longer emission period than it was expected. Swift also measured the most distant GRB so far, at a redshift of 9.4.

In 2008, another telescope to detect high energy γ-ray emission from GRBs was launched by NASA: the Fermi satellite. Fermi made even more detailed and wider observations of γ-ray spectra possible, revealing informations about their features and thus setting constraints on the theoretical models. Fermi and Swift are the most important experiments for GRB physics at present.

50 years after their discovery, GRBs are still one of most mysterious phenomena in astrophysics. Several theoretical models make the attempt to explain the full picture of GRBs, but so far no model is clearly favoured by observations. One critical piece that is missing, is the presence of cosmic rays in GRBs. The predicted GRB astronomy in

terms of neutrinos with experiments such as IceCube will serve as a smoking gun signal for cosmic rays in GRB environments in the near future.

3.2 PHENOMENOLOGICAL DESCRIPTION

All currently studied GRB models have in common that there are at least two categories of progenitors: The merger of two compact objects and the collapse of a massive star ($m_{\mathrm{Star}} > 8M_{\odot}$) at the end of its lifetime. Furthermore, all models agree that the emission of GRBs is highly relativistic and collimated. Since it can be inferred from γ-ray emission, it is also commonly assumed that the afterglow emission of GRBs is mostly due to synchrotron radiation [67].

In this thesis we restrict the treatment of our model predictions to the fireball model with internal shocks. In the following, we give an overview of the timeline of a GRB event according this model.

At least two possible GRB progenitor scenarios are hypothesized to exist: Firstly, the merger of compact objects (see Fig. 9 (1)), secondly the core collapse of massive stars (see Fig. 9 (2)). In the case of a merger, it is assumed that either two neutron stars (NS) or a black hole (BH) - NS binary system merge [46, 67]. When the two objects merge, the cataclysmic event is accompanied by an energy release in the form of gravitational waves. This signal can be measured on Earth with gravitational wave detectors like LIGO and Virgo. A central compact object, presumably a BH, with a surrounding accretion disk is formed as a result of the event. It is also possible that a fast rotating NS is formed first. This NS will eventually also collapse into a BH. The BH is called the central engine of the GRB. Accretion from the thick gas torus surrounding the central engine powers the GRB emission. The emission is jet-like along the spin axis of the BH (Fig. 9 (3)).

At the end of their life times, the cores of massive stars become incapable of balancing the gravitational force by their radiation pressure and consequently they collapse into a proto-NS, which can lead to the second GRB progenitor scenario. The gravitational energy released in this core-collapse can power GRB emission, which is emitted in jets along the rotation axis of the NS. Such core collapse events are associated with Type Ic supernovae. Supernovae of this type are characterized by a lack of helium (He) and oxygen (H) signatures in the spectrum. Therefore, only massive stars that have already lost their H and He components are candidates. Wolf Rayet stars are one example for such astrophysical objects [67]. Wolf Rayet stars lose mass due to strong stellar winds, which strip away H and He.

Prompt emission is released in the moment of the cataclysmic event. This release can be detected in terms of gravitational waves and thermal neutrinos. Almost 99% of the released energy leaves during this initial emission period. The small fraction of the gravitational energy is thought to be dissipated into the region above and below the spinning central object. This creates a *fireball*, which is an optically thick plasma with very high temperature and consists out of electrons, protons, photons and magnetic fields [46]. It is powered by the central engine and starts to expand adiabatically with increasing velocity. This expansion happens along the spin axis of the BH in relativistic jets. This is

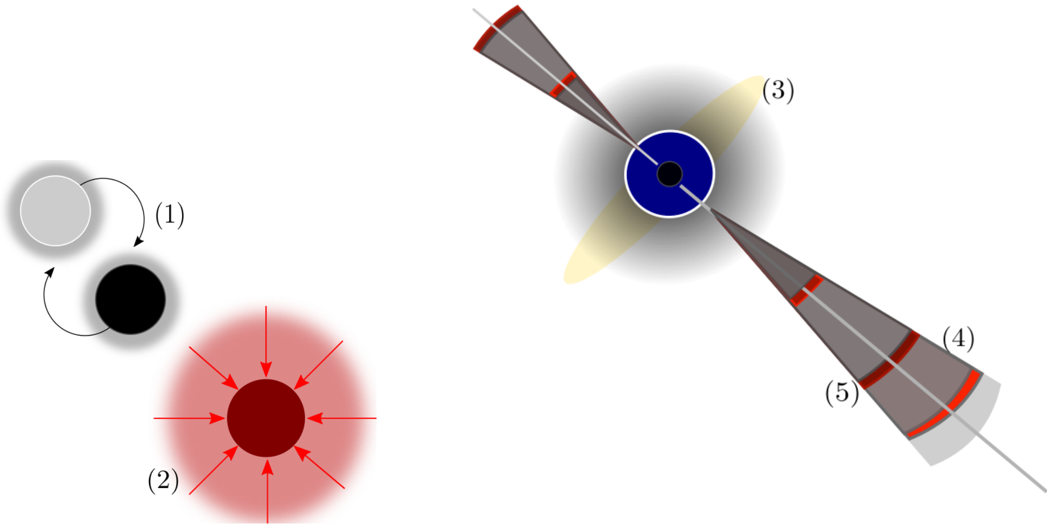

FIG. 9. Possible Progenitors (left) and remnant central engine (right), powering the GRB. Progenitors are NS-BH merger (1), NS-NS merger or a core collapse of a super massive star (2). In the process of the cataclysmic event a central engine (3), BH or NS, is formed. The ejecta, powered by the accretion disc is emitted relativistically in jets (4). At shock fronts (5) particles are accelerated, and neutrinos and synchrotron gγ-rays are produced.

illustrated in Fig. 9 (4). The central engine is driven by the accretion disc over a large time scale. During this period the emission of plasma is not continuous. One can imagine the outflow in terms of individual shells with a finite thickness and variations in energy and velocity with respect to each other (Fig. 9 (5)).

The velocity of the expanding plasma is expressed in terms of the Lorentz factor Γ. Figure 10 shows the evolution of the Γ factor with increasing distance r from the central engine. After a shell is emitted from the central engine, the velocity increases until a saturation radius r_s is reached, where most of the initial thermal energy is converted into kinetic energy. After this point, the shell is in a so called *coasting phase* with constant velocity. Individual shells start to collide due to their different velocities, which arise from variations in Γ from the central engine. As we will discuss in more detail in section 3.3, shock fronts are created at the collision sites. Charged particles are accelerated along these *internal shocks* and energetic electrons emit γ-rays via synchrotron radiation. For these γ-rays to become visible, the internal shocks have to be created above the photosphere. The photospheric radius r_{ph} marks the region from which on the fireball becomes transparent to photons and thermal γ-rays are emitted. These non-thermal γ-rays can be detected on Earth. Due to interactions between the accelerated high energy protons with photons, neutrinos are produced, via the photo-hadronic processes we discussed in section 2.2. The high-energy CRs and neutrinos are emitted and should be detectable on Earth.

The shells lose some of their energy due to the transformation of their kinetic energy into γ-rays, neutrinos and CRs. As a consequence, the velocity decreases slightly at the radius r_{is}, where internal shocks start to form. In the last phase, the jet accumulates matter ahead of it while propagating through the space. Eventually, the amount of matter will become so large that again a new shock front is created. This type of interaction with the

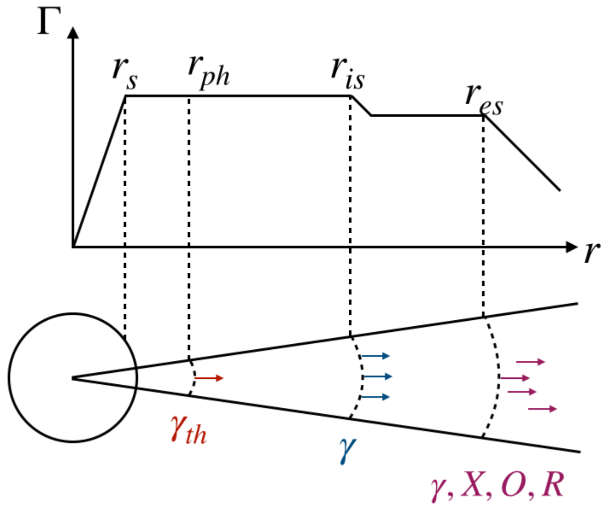

FIG. 10. Behaviour of the lorentz factor Γ as a function of distance to the central engine, expressed as radius r. Until the saturation radius r_s Γ grows linearly, followed by a constant phase, the coasting phase, where the fireball expands adiabatically. At the radius r_{ph} the fireball becomes optically transparent for thermal photons. Above the photosphere internal shocks at r_{is} cause protons to accelerate and synchrotron radiation is emitted. This brings energy loss with it and therefore Γ decreases slightly. After some constant phase the jet accumulated large amount of matter in front of it and an external shock is formed due to which γ and X-rays as well as photons in the optical and infrared range are emitted. The plot was reproduced after [46].

circumburst medium is described by *external shocks* and is responsible for GRB afterglow emission. In external forward shocks, particle acceleration transforms the remaining energy into γ- and X-rays, optical, and infrared photons. With the decreasing velocity the shock and thus the acceleration strength reduces and the photon spectra fade out slowly [67]. The broad-band afterglow can be detected over a long period of multiple weeks to months. The transition phase between the prompt emission due to internal shocks and the afterglow emission is not precisely distinct. Late time central engine activities can cause internal shocks at the same time as the afterglow emission while the forward shock already starts to accelerated particles [67].

3.3 FERMI ACCELERATION IN RELATIVISTIC SHOCKS

High-energy protons are assumed to interact with photons and produce neutrinos. In the plasma of the relativistically expanding fireball, protons are expected to accelerate via first order Fermi acceleration. This acceleration in the magnetized plasma is of statistical nature and can be explained as follows [19, 34]. due to the collision of two expanding shells a plane shock front is created. Before the collision, the two shells move with different velocities β_1 and β_2. The shell which is emitted at a later point in time than the first shell moves faster with $\beta_2 > \beta_1$. At the collision point, a discontinuity in pressure density and velocity is created, that propagates faster than the speed of sound, creating a shock front.

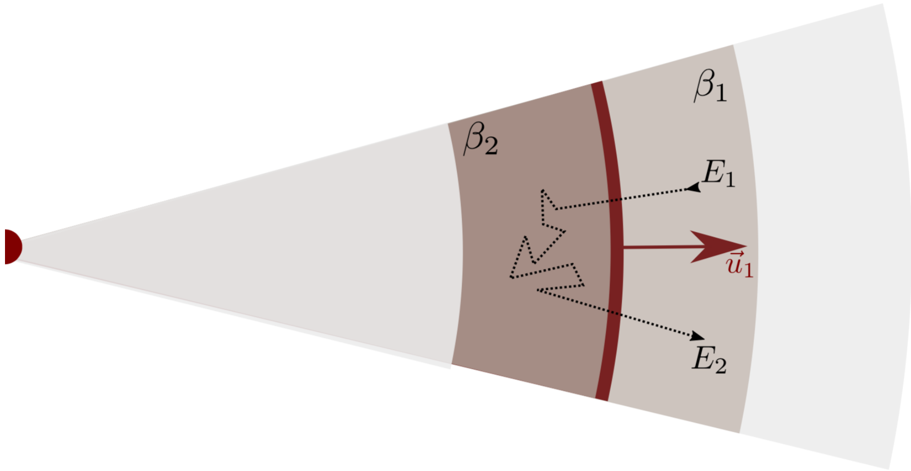

FIG. 11. Collision of two shells with different velocities and statistical Fermi acceleration along the shock front. The red arrow indicates the velocity of the shock front $\vec{u}_1$. A charged particle with initial energy E_1 will gain energy by "scattering" in magnetic fields and leave the medium with β_1 (upstream) with energy $E_2 > E_1$.

In Fig. 11 the two shells and their collision site (dark red thick line), the shock front, are illustrated. In the observer frame, the shock front moves with velocity $\vec{u}_1$ towards the right. The medium with β_1 is called the upstream, the medium "behind" the shock front the downstream. In this picture, a shock can be viewed within three reference frames: from the view of the upstream frame (β_1), the downstream frame and the shock frame.

In the shock frame, the upstream moves towards the left (towards the shock front) with $-\vec{u}_2$, for which $\vec{u}_1 > |\vec{u}_2|$. The downstream moves towards the left with $-\vec{V} = -(\vec{u}_1 - |\vec{u}_2|)$. As viewed from the downstream frame, the upstream moves towards the left and particles crossing the shock scatter randomly (denoted by the dashed line). If a particle from the upstream medium at $r > r_{\text{shock}}$ crosses the shock front ("encounters") into the downstream, it will gain energy in the magnetized plasma due to "scattering" in the magnetic fields. After random scattering it has some probability that it scatters back into the other side of the shock front. This entering and exiting the shocked medium is counted as one "cycle" and brings a net energy gain, which is proportional to the shock front velocity. Therefore, this type of acceleration mechanism is called *first order* Fermi acceleration. For the upstream frame view, the downstream moves towards the right. Also in this case, incoming particles scatter randomly in the upstream medium and gain energy.

Fermi acceleration serves as an explanation for the power-law spectrum of CRs we observe. Assuming that the energy gain due to Fermi acceleration is proportional to energy allows us to write $\mathrm{d}E/\mathrm{d}t = E/t_{\text{gain}}$ with the acceleration timescale t_{gain}, which in this case is the inverse Lamour radius. Furthermore, the loss of particles leaving the acceleration zone is proportional to the number of particles via $\mathrm{d}N/\mathrm{d}t = -N/t_{\text{loss}}$, where t_{loss} is the loss time-scaling. These two relations can be used to write $\mathrm{d}N/\mathrm{d}E = -\frac{t_{\text{gain}}}{t_{\text{loss}}} N/E$ and thus

$$N(E) = N_0 \left(\frac{E}{E_0}\right)^{-\frac{t_{\text{gain}}}{t_{\text{loss}}}}, \tag{3.1}$$

from which we can infer the CR spectrum as

$$\frac{\mathrm{d}N}{\mathrm{d}E} \propto E^{-\frac{t_{\text{gain}}}{t_{\text{loss}}}-1} \,. \tag{3.2}$$

For diffuse shock acceleration in strong shocks in can be shown, that $t_{\text{gain}} = t_{\text{loss}}$. In this case, Eq. 3.2 leads to a spectral index of 2 for the CR spectrum at the source [34].

3.4 GRB PARAMETERS FROM NON-NEUTRINO OBSERVATIONS

GRBs were detected for the first time in the late 60s. Since then most of our knowledge about GRBs is inferred from electromagnetic observations. With the first successful coincident detection of gravitational waves and γ-rays it has become possible to connect the origin of high energetic γ-rays with the origin of GWs. Since this benchmark observation, we use GWs as a second messenger to gain information about GRBs. The two messengers, photons and GWs, are extremely helpful when it comes to the prediction of neutrinos originating from the same source. The observable flux of neutrinos on Earth can be predicted based on theoretical assumptions and parameters describing the GRB, which are obtained from non-neutrino observations. Before diving into the derivation of the prediction, we will have a detailed look on the parameters that are used and inferred from measurements of electromagnetic and gravitational wave signals.

Time scales: T_{90}, t_{var}

The duration of a GRB is represented by T_{90} [s]. This time scale is measured as the period in which 90% of the total γ-ray flux is registered by the detector [63]. This time measurement is strongly dependent on the detector: not only the energy range of the detector, but also its sensitivity may account for different T_{90} values measured by different detectors [67]. From the distribution of T_{90} it can be inferred that GRBs appear in two categories: short (less than 2s, centred around 0.3s) and long (centred around 20s) GRBs [63]. As already discussed previously, the two duration categories arise from different progenitors: short GRBs are related to binary mergers, while long GRBs are caused by core collapse events of massive stars. Another important time scale in the treatment of GRBs is the variability time-scale t_{var}. It is determined by fluctuations within the light curve and is interpreted as the time interval between collisions of different shells emitted from the central engine. T_{90} and t_{var} are related via the number of collisions

$$t_{\text{var}} \cdot N_{\text{coll}} = T_{90} \,. \tag{3.3}$$

Energy Fluence: $\mathcal{F}_\gamma$ [erg/cm^2]

The energy fluence is defined as the time-integrated energy flux per unit area. For Fermi observations the photon fluence $\mathcal{F}_\gamma$ is integrated over the time scale of T_{90} and the detector area.

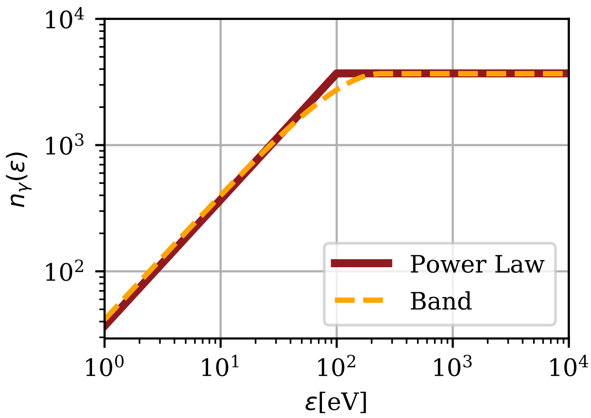

FIG. 12. Comparison between the Band spectrum (yellow dashed line) and power spectrum (red line) for the observed photon spectrum n_γ. The used parameters for these plots are: ϵ_{break} = 100 eV, α=0.5, β=2.0.

Redshift: z

The redshift z is a cosmological consequence of the expansion of the Universe, and denotes the degree to which light has been redshifted during propagation. The earlier in time the light was emitted, the larger is z. Therefore, z is indirectly used as a distance measure. It can be determined from features in the γ-ray spectra, such as characteristic emission and absorption lines, where it leads to shifted features in electromagnetic spectra for distant astrophysical sources [55]. The theoretically most distant observable photons have a redshift of ∼1100. This corresponds to the time at which the Universe began to be transparent for photons, now observed as the microwave background.

Photon Spectrum: n_γ

The spectral photon density of a GRB detection in γ-rays is usually parametrized as a Band spectrum [17]

$$n_\gamma(\epsilon) \propto \begin{cases} (\epsilon/\epsilon_0)^{-\alpha} e^{-\epsilon/\epsilon_0} & \epsilon < \epsilon_{break} \\ (\epsilon/\epsilon_0)^{-\beta} e{-\beta + \alpha}(\beta-\alpha)^{\beta-\alpha} & \epsilon > \epsilon_{break}\,, \end{cases} \tag{3.4}$$

or simplified as a broken power law spectrum

$$n_\gamma(\epsilon) \propto \begin{cases} (\epsilon/\epsilon_{br})^{-\alpha} & \epsilon < \epsilon_{break} \\ (\epsilon/\epsilon_{br})^{-\beta} & \epsilon > \epsilon_{break}\,; \end{cases} \tag{3.5}$$

where ϵ is the photon energy, $\alpha \simeq 0-2$ and $\beta \simeq 1-4$ are spectral indices, ϵ_{br} the break energy and $\epsilon_0 = \epsilon_{br}/(\beta-\alpha)$ [67]. An illustrative example of such a spectrum and the two different parametrizations in comparison can be seen in Fig. 12. The Band spectrum is smoother around the break energy. The approximated broken power law spectrum shows nevertheless a good correspondence. The observed photon spectrum n_γ depends on the energy range covered by the telescope ($\epsilon_{\text{min}}^{\text{instr.}}$, $\epsilon_{\text{max}}^{\text{instr.}}$), which usually differs from the true intrinsic cutoff energies (ϵ_{min}, ϵ_{max}) of the spectrum. Therefore a normalization factor is defined as

$$N = \left(\int\limits_{\epsilon_{\text{min}}}^{\epsilon_{\text{max}}} \mathrm{d}\epsilon\epsilon \frac{\mathrm{d}n}{\mathrm{d}\epsilon_\gamma} \right) \Bigg/ \left(\int\limits_{\epsilon_{\text{min}}^{\text{instr.}}}^{\epsilon_{\text{max}}^{\text{instr.}}} \mathrm{d}\epsilon\epsilon \frac{\mathrm{d}n}{\mathrm{d}\epsilon_\gamma} \right) . \tag{3.6}$$

All quantities associated with the photon spectrum, as the fluence, have to be corrected. For the initially observed input value for the fluence $\widehat{\mathcal{F}}_\gamma$ one obtains the true fluence F_γ by correcting for the instrumental limitations through

$$\mathcal{F}_\gamma = \widehat{\mathcal{F}}_\gamma N \, . \tag{3.7}$$

In the following theoretical descriptions we assume a perfect telescope, which means we assume no difference between instrumental and true energy cutoffs of the spectrum and thus apply no correction factor N. For actual neutrino predictions based on observational parameters, we will apply the correction factor.

Lorentz Factor: Γ

The Lorentz factor is defined as

$$\Gamma = \frac{1}{\sqrt{1-\beta^2}} \, , \tag{3.8}$$

where $\beta = v/c$ is close to one for highly relativistic objects with $v \sim c$. One consequence of a relativistic moving emitter is, that emission is boosted along the direction of motion. The so-called *Doppler boost* describes, that initial isotropic emission in the rest frame of the fast-moving ejecta is boosted along the direction of flight for an observer in a laboratory frame. We will discuss this phenomenon in more detail in the next chapter. The experimental determination of the Lorentz factor Γ is neither very precise nor trivial. Many different methods have been proposed and used to obtain information about Γ (e.g. the opacity method, afterglow onset method, photosphere method and others, see [67] for more details). For all the above-mentioned models, the determination of Γ is made indirectly through theoretical modelling, and thus the resulting value depends heavily on one's model of choice [67]. The Γ values for GRBs typically vary between 10^2 to 10^3.

4 ON-AXIS NEUTRINO PREDICTIONS FROM GRBS

The acceleration of high-energy CRs in the extreme environments of GRBs could be established by the successful detection of neutrinos in neutrino observatories as IceCube and ANTARES. Neutrinos from GRBs are predicted for more than 20 years [64], but have not been observed yet. For advanced studies and searches for such high energetic neutrinos, it is necessary to have model predictions of neutrino spectra as functions of energy. Such spectra depend on individual GRB parameters, which are obtained from non-neutrino observations of electromagnetic and gravitational wave signals. The assumed models used for the prediction of spectra are tested by possibly observations. The current non-observations of neutrinos are used to exclude models and constrain assumptions that are made within model definitions. The main work of this thesis focuses on the development of such model predictions by including phenomena as off-axis emission and extension of the jets, study their effects on earlier prediction models and ideally will help to find and interpret the eagerly awaited neutrino signal from a GRB.

In this chapter, we go through the theoretical derivation of the neutrino flux predictions based on the internal shock fireball model. We firstly walk through all calculations that have to be done to set the resulting neutrino flux together: transformations between reference frames (section 4.1) and internal GRB quantities (section 4.2), such as the optical depth in the GRB frame, synchrotron losses of secondaries and the proton flux in the GRB. All these quantities are combined in the neutrino flux determination in section 4.2.4, which is initially done for the on-axis case for simplicity. We also comment on the effect of neutrino oscillations (section 4.2.5). Afterwards, we introduce the IceCube software FIREBALLET, which is used to calculate the actually neutrino spectra (section 4.3). Additionally we set up three reference GRB models to calculate the neutrino spectra, which will come handy in terms of comparison of results obtained in this thesis, but also with literature (section 4.3.2).

4.1 REFERENCE FRAMES AND TRANSFORMATIONS

In the approach to sort observed quantities in the correct relation to its source frame, three different reference frames are used to describe GRBs phenomenologically:

- The source or stellar frame K^*, laboratory frame
- The Earth's observer frame K, observer frame
- The GRB jet or shock frame K', co-moving frame

The reference frames and their relations to each other are shown in Fig. 13.

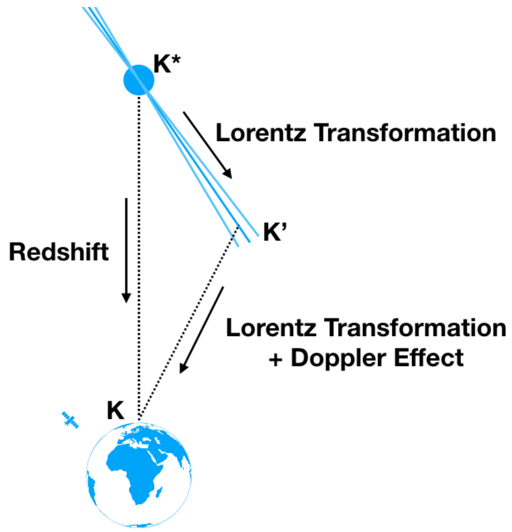

FIG. 13. The three different reference frames related to the source, jet and observer. Also shown are the transformations that have to be taken into account when changing from one to another frame.

The co-moving GRB-frame K' moves relativistically (with velocity $v = \beta c \sim c$, where $\beta = v/c$) along the jet axis away from the source frame K^*. Thus, to change from the source frame of the central engine to K' one applies a Lorentz transformation. For distances in the spatial and time-coordinates, one can write out the usual Lorentz transformation from special relativity [43], where $\Gamma = 1/\sqrt{1-\beta^2}$ is the Lorentz factor:

$$\begin{pmatrix} \mathrm{d}t' \\ \mathrm{d}r'_{\shortparallel} \end{pmatrix} = \begin{pmatrix} \Gamma & -\Gamma\beta \\ -\Gamma\beta & \Gamma \end{pmatrix} \cdot \begin{pmatrix} \mathrm{d}t^* \\ \mathrm{d}r^*_{\shortparallel} \end{pmatrix} , \tag{4.1}$$

$\mathrm{d}r^*_{\shortparallel}$ and $\mathrm{d}r'_{\shortparallel}$ denote the spatial coordinates parallel to the direction of the boost. From the second equation in Eq. 4.1 we obtain

$$\mathrm{d}r'_{\shortparallel} = \Gamma(\mathrm{d}r^*_{\shortparallel} - \beta \mathrm{d}t^*) \, . \tag{4.2}$$

To measure a length interval in the co-moving frame, we express the term in the rest frame K^*. Measuring the two ends of a length scale, e.g. a rod, at the same point in time, $\mathrm{d}t^* = 0$ gives

$$\mathrm{d}r'_{\shortparallel} = \Gamma \mathrm{d}r^*_{\shortparallel} \, , \tag{4.3}$$

which describes length contraction in special relativity.

Now, lets consider the first equation in Eq. 4.1, from which we want to derive the relation of time intervals in the two frames. In the first equation,

$$\mathrm{d}t' = \Gamma(\mathrm{d}t^* - \beta \mathrm{d}r^*_{\shortparallel}) \, , \tag{4.4}$$

we insert the second equation from Eq. 4.2. We measure the time interval in the co-moving frame at a fixed point and therefore we set $\mathrm{d}r'_{\shortparallel} = 0$. This leads to the relation of time dilation [24, 67]

$$\mathrm{d}t' = \Gamma(\mathrm{d}t^* - \beta \mathrm{d}r^*_{\shortparallel}) = \Gamma \mathrm{d}t^*(1-\beta^2) = \frac{1}{\Gamma}\mathrm{d}t^* \, . \tag{4.5}$$

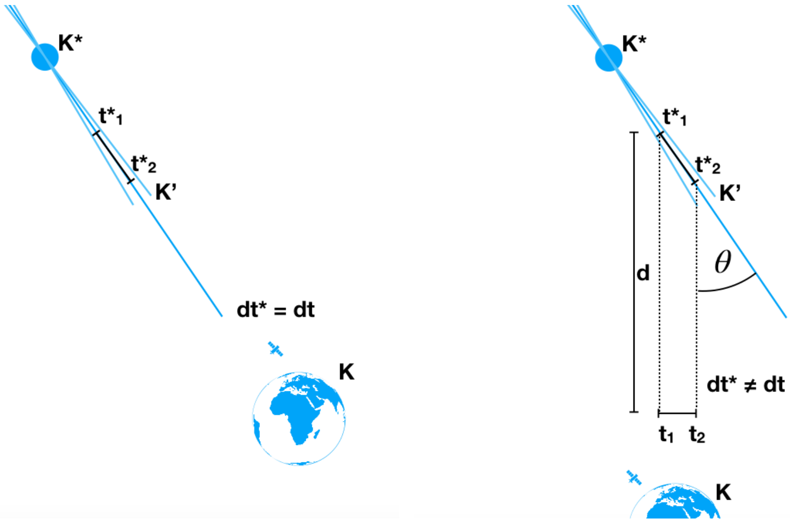

(a) On-axis constellation, where the GRB-frame is within the line-of-sight of the observer.

(b) Off-axis constellation, where an additional time delay effect has to be taken into account, arising from the non-zero angle θ_v.

FIG. 14. Different source - shock - observer constellations, which require different treatments when formulating transformation relations. The time difference between the two photons is measured in the source frame (emission) and the observers frame (detection).

The observer and the source frame are in general the same reference frame, except the additional factor $(1+z)$ for the cosmological redshift. Instead, when going from the co-moving GRB frame to the observer frame, one has to consider a time delay for an observer positioned at Earth. Consider the following [46]: Two emission points emit photons at times t_1^* and t_2^* and distances $r_1 = r_1^*$ and $r_2^* = r_2$ to the source. The distance from the emitter to the source in spatial coordinates is the same for the source and Earth observer frame, $\mathrm{d}r = \mathrm{d}r^*$. But for the difference in time this is not a general valid statement, $\mathrm{d}t \neq \mathrm{d}t^*$. The difference arises from the time delay effect, also known as the Doppler effect. While $\mathrm{d}t^*$ describes the difference in time between the emission of two photons, $\mathrm{d}t$ describes the difference in arrival at Earth (the observer) of the two photons, see Fig. 14a and Fig. 14b.

One has to infer the arrival times as follows, where $\gamma_{1,2}$ denotes two photons, emitted in the source frame K^* at times t_1^*, t_2^*, with $\mathrm{d}t* \neq 0$. The emission of the first photon happens at a distance d to Earth:

$$\begin{aligned}
&\gamma_1 \text{ emitted at } \; r_1^* = r_1, t_1^*, \text{ arrives at time } \; t_1 = t_1^* + \frac{d}{c}\,, \\
&\gamma_2 \text{ emitted at } \; r_2^* = r_2, t_2^*, \text{ arrives at time } \; t_2 = t_2^* + \frac{d}{c} - \beta\cos(\theta_v)\mathrm{d}t^*\,.
\end{aligned}$$

The additional factor d/c accounts for the time it takes a photon to travel the distance d. The factor $\beta\cos(\theta_v)\mathrm{d}t^*$ considers an emission jet, that is not aligned with the Earth's line of sight. This factor reduces to $\beta\mathrm{d}t^*$ for an on-axis observation, where the angle between the jet-direction and the Earth's line of sight is zero.

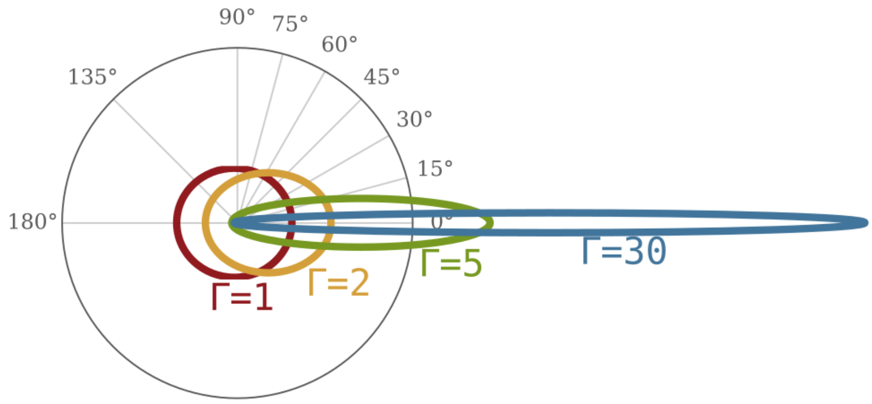

FIG. 15. Lorentz boost for different Γ factors: 30, 5, 2, and 1 (which corresponds to perfectly isotropic emission). An on-axis observer with $\theta_v = 0$ observes a boost of $\sim 2\Gamma$. An off-axis observer with $\theta_v \neq 0°$, experiences a reduced Doppler boost, dependent on the viewing angle, $\mathcal{D} = 1/\Gamma(1 - \beta\cos(\theta_v))$.

With this and Eq. 4.5 we derive the general expression for the transformation between the GRB frame and the observer's frame:

$$\begin{aligned} \mathrm{d}t = t_2 - t_1 &= (t_2^* + \frac{d}{c} - \beta cos(\theta_v)\mathrm{d}t^*) - (t_1^* + \frac{d}{c}) \\ &= (1 - \beta cos(\theta_v))\mathrm{d}t^* \\ &= \underbrace{(1 - \beta cos(\theta_v))\Gamma}_{\mathcal{D}^{-1}} \mathrm{d}t' \,, \end{aligned} \tag{4.6}$$

where in the last step the Doppler factor $\mathcal{D}$ is given as

$$\mathcal{D}(\theta_v) := \frac{1}{\Gamma(1 - \beta\cos(\theta_v))} \,. \tag{4.7}$$

An approximation for large Γ factors ($\Gamma \gg 1$) and small off-axis angles ($\theta_v \to 0$) gives [21]

$$\mathcal{D}(\theta_v) \approx \frac{2\Gamma}{1 + \theta_v^2\Gamma^2} \,. \tag{4.8}$$

For an observer, positioned in line with the GRB jet ($\theta_v = 0$), the Doppler factor reduces to the simple expression $\mathcal{D}(0) = 2\Gamma$, which is the maximal value of $\mathcal{D}$. Nevertheless, standard on-axis calculations of neutrino predictions are usually done with a Doppler factor of Γ [21, 46], which is the Doppler factor for a special case. We consider for a moment the denominator in Eq. 4.8. For a specific *critical viewing angle* θ_v of $1/\Gamma$, the denominator reduces to 2 and therefore, $\mathcal{D} \to \Gamma$. For smaller viewing angles than $1/\Gamma$, the 1 dominates and we will obtain a 2Γ approximation. For all viewing angles above $1/\Gamma$, the Doppler factor reduces to values below Γ. The angle $1/\Gamma$ describes a critical angle, which will become important later on.

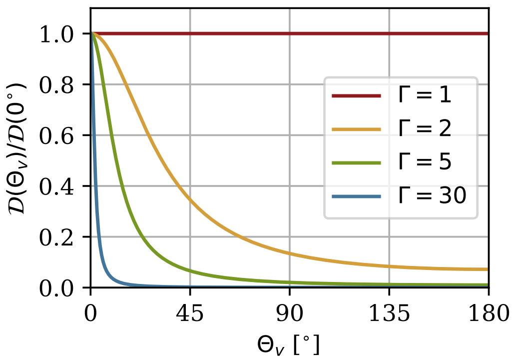

FIG. 16. Doppler factors, $\mathcal{D}$, as a function of the viewing angle θ_v, for the same Γ factors as visualized in Fig 15. The Doppler factors are normalized to their on-axis values, which correspond to $\sim 2\Gamma$.

Isotropic emission in the co-moving frame is boosted along the direction of motion for an observer in the rest frame of the Earth by the factor $\mathcal{D}$. This is shown in a geometric visualization in Fig. 15. The red circle with Γ=1 denotes isotropic emission. This emission gets more boosted for higher Γ, which means a more relativistic outflow. For a viewing angle deviating from 0°, the boost factor reduces. This is also illustrated in Fig. 16. This figure shows how the Doppler factor, normalized to its on-axis value, $\mathcal{D} \sim 2\Gamma$, decreases with increasing off-axis angle θ_v. For high Γ factors, the suppression is stronger than for small Γ.

The general Doppler factor, given in Eq. 4.6, prepares the basis for transforming diverse general quantities from the observer's frame into the GRB co-moving frame and vice versa [46, 67]

$$\mathrm{d}t = \mathcal{D}^{-1}\, \mathrm{d}t' \,, \tag{4.9}$$

$$\mathrm{d}r = \mathcal{D}\, \mathrm{d}r' \,, \tag{4.10}$$

$$\mathrm{d}V = \mathcal{D}\, \mathrm{d}V' \,, \tag{4.11}$$

$$\nu \sim \frac{1}{\Delta t} \Rightarrow \nu = \mathcal{D}\, \nu' \,, \tag{4.12}$$

$$E \sim \frac{1}{\Delta t} \Rightarrow E = \mathcal{D}\, E' \,. \tag{4.13}$$

For the solid angle, $\mathrm{d}\Omega$, we decompose $\mathrm{d}\Omega$ into azimuthal and zenith components, $\mathrm{d}\mu \mathrm{d}\phi$, where $\mu = \cos(\theta_v)$. In the description of general relativity, massless particles are moving along null-curves, which are defined as $c^2 \mathrm{d}t^2 - \mathrm{d}r^2 = 0$, and therefore $\mathrm{d}t^2 = \mathrm{d}r^2$ in our units [24]. For null-curves, the relation $\mathrm{d}t = \mathrm{d}r$ is valid in every frame, also in the GRB frame: $\mathrm{d}t' = \mathrm{d}r'$. With this assumption, one can derive an expression for $\cos(\theta_v)$ (find the full derivation in APPENDIX A) as a function of θ'_v, the angle in the GRB frame and β, the shock velocity

$$\cos(\theta_v) = \frac{\cos(\theta'_v) + \beta}{1 + \beta \cos(\theta'_v)} \,. \tag{4.14}$$

For $\mu = \cos(\theta_v)$ we calculate the differential

$$\begin{aligned}
\mathrm{d}\mu &= \mathrm{d}\left(\frac{\mu' + \beta}{1 + \beta\mu'}\right) \\
&= \frac{(1 + \beta\mu')(\mathrm{d}\mu') - (\mu' + \beta)\beta\mathrm{d}\mu'}{(1 + \beta\mu')^2} \\
&= \frac{1}{\Gamma^2}\frac{1}{(1 + \beta\mu')^2}\mathrm{d}\mu' \\
&= \mathcal{D}^{-2}\mathrm{d}\mu' \,.
\end{aligned} \tag{4.15}$$

We have $\mathrm{d}\phi = \mathrm{d}\phi'$, since a boost does not affect the orthogonal direction, in this case $\mathrm{d}\phi$. With this and Eq. 4.15 we obtain the relation for the angular distribution between the GRB and observer frame

$$\mathrm{d}\Omega = \mathcal{D}^{-2}\mathrm{d}\Omega' \,. \tag{4.16}$$

The general relations, given in Eqs. 4.9-4.13 and Eq. 4.16, can now be used to derive the internal quantities, which have to be calculated in the GRB-frame but are based on measurements in the observer frame. Therefore, the measured quantities need to be transformed correctly into the GRB frame before further calculations can be done. These calculations will eventually lead to an estimate of the neutrino spectrum.

The internal shock *fireball* model predicts neutrinos coming from GRBs, produced in γ-CR interactions. It assumes a relativistically expanding outflow, the *fireball*, consisting out of electrons, positrons, photons, baryons and magnetic fields [46]. Protons accelerate due to Fermi acceleration, while γ-rays are mostly produced as synchrotron radiation. The high-energy protons and photons interact within the fireball environment and are expected to produce neutrinos mainly due to pion production and their decay. In the next sections in this chapter, we are deriving piecewise the components of the predicted neutrino spectrum. This will use primarily GRB parameters from non-neutrino observations, such as T_{90}, $\mathcal{F}_\gamma$, t_{var}, $n_\gamma(\epsilon)$, z and Γ, which we introduced in section 3.4. With these measured parameters at hand, it is possible to infer GRB internal quantities, such as the optical depth $\tau_{p\gamma}$, the maximal proton energy E_{pmax} and the order of synchrotron losses and neutrino production efficiency. The components are building on non-neutrino measurements in the Earth frame and have to be transformed correctly into the GRB jet frame.

The *isotropic equivalent luminosity* for the photons L_γ^{iso} [erg s^{-1}] is the rate at which a source emits energy in form of electromagnetic radiation. Isotropic equivalent means that the emission is assumed to be isotropic. L_γ^{iso} is used to characterize GRBs and is related to in the observer frame measured quantities as [67]

$$\frac{\mathcal{F}_\gamma}{T_{90}} = \frac{L_\gamma^{\mathrm{iso}}}{4\pi d_L^2}\,. \tag{4.17}$$

If the sources are centred within a sphere, whose radius corresponds to the *luminosity distance* to Earth d_L, we observe the luminosity per unit area ($4\pi d_L^2$) as the flux (Φ[erg s^{-1} cm^{-2}] $=\mathcal{F}_\gamma/T_{90}$) on the LHS in Eq. 4.17. These cosmological parameters and the observed redshift of the GRB are used to define the luminosity distance d_L in a flat Robertson-Walker metric

$$d_L(z) = (1+z)\int\limits_0^z \frac{1}{H(z)}\mathrm{d}z\,. \tag{4.18}$$

The integrand $\int_0^z \frac{1}{H(z)}\mathrm{d}z$ is also known as the *co-moving distance* d_C [55]. Therefore, one can also write $d_L(z) = (1+z)d_C$. Another important distance scale is the so-called *angular diameter distance* d_A, which is related to d_L via $d_L = (1+z)^2 d_A$. We will introduce the angular-distance again in section 5.1.

In a flat universe one can calculate the luminosity distance d_L of the source with the Hubble parameter $H(z) = H_0\sqrt{(\Omega_\Lambda + \Omega_m(1+z)^3)}$, where Ω_Λ and Ω_m are the density parameters for dark energy (Λ) and matter (m, sum of dark and baryonic matter). The Hubble parameter describes the current rate of our Universe's expansion and is approximately 68 km s^{-1} Mpc^{-1} [59]. For a flat universe, the density parameters have to sum up to one [24]

$$1 = \Omega = \Omega_\Lambda + \Omega_m + \Omega_R\,, \tag{4.19}$$

where Ω_R denotes the radiation density parameter, which is negligible in our current dark energy dominated universe. The most current values, measured by the Planck collaboration are $\Omega_m = 0.308 \pm 0.012$ and $\Omega_\Lambda = 0.692 \pm 0.012$ [59], which satisfy Eq. 4.19 within their uncertainties.

The relation of the burst duration T_{90} and the luminosity L_γ^{iso} is defined via the *isotropic energy* E_γ^{iso}, which has an important role, when estimating the energy density in the GRB frame. E_γ^{iso} is the total amount energy (in terms of electromagnetic radiation), emitted during the entire burst period T_{90}

$$E_\gamma^{\mathrm{iso}} = L_\gamma^{\mathrm{iso}} T_{90}\,. \tag{4.20}$$

The luminosity for one unit emitting element in the GRB jet frame (later called *blob*) is defined as

$$\begin{aligned} L'_\gamma &= \frac{\mathcal{D}^{-1} E_\gamma}{\mathcal{D} T_{90}} \\ &= \mathcal{D}^{-2} L_\gamma\,. \end{aligned} \tag{4.21}$$

For a point source, which corresponds to an isotropic emitting element (*blob*), one is more interested in the isotropic equivalent luminosity L_γ^{iso}. The emission is isotropic in the co-moving GRB-frame, but the observer in the rest frame sees emission only in one direction. L_γ^{iso} describes the luminosity under the assumption, that the emission is isotropic in the observer's frame as well. The luminosity given in Eq. 4.21 is multiplied by $\int \mathrm{d}\Omega = 4\pi$ and with Eq. 4.16 we find [67]

$$L_\gamma'^{\mathrm{iso}} = \mathcal{D}^{-4} L_\gamma^{\mathrm{iso}}\,. \tag{4.22}$$

In section 3 we showed, that the γ-CR interactions determines the neutrino production, and thus the spectrum. Therefore, special interest goes to the target photon energy density (U'_γ) and the proton energy. For the density, we firstly define the energy within one shock, instead of the entire burst. The reason for this is, that we have a way to measure the volume that corresponds to the interaction region of one shock front. We can use time scales to connect the energy in the entire burst with the sub-shell energy. While the time scale T_{90} describes the entire burst emission time, meaning multiple shell collisions and shock fronts forming, t_{var} expresses the duration in which interactions are happening at one single shell. Thus, the ratio t_{var}/T_{90} corresponds to the ratio in energies $E_\gamma'^{\mathrm{shock}}/E_\gamma'^{\mathrm{iso}}$. We find in the jet frame

$$E_\gamma'^{\mathrm{shock}} = \frac{t_{\mathrm{var}}}{T_{90}} E_\gamma'^{\mathrm{iso}}\,. \tag{4.23}$$

The emission region is approximated by the *dissipation radius,* r_{dis}. This radius is defined in the source frame K^* and describes the distance of the collision from the central engine, as this is the site where protons start to accelerate via Fermi acceleration [12]. The dissipation radius r_{dis} results from the *catch up* problem [67]: Two shells with different velocities (Γ_1, Γ_2 and $\Gamma_2 > \Gamma_1$) are emitted by the central engine caused by Γ variations in the emission from the central engine. The two shells have a time separation of $\Delta t = t_{\mathrm{var}}/(1+z)$, where Δt is measured in the stellar frame and t_{var} in the observer frame. At the collision time $t_{\rm col}$, the second (faster) shell catches up with the first one and they collide. We can write [67]

$$(\beta_2 - \beta_1) t_{\rm col} = \beta_1 \Delta t \,.$$

The collision radius, $r_{\rm dis}$ can therefore be expressed as (for $\Gamma_{1,2} \gg 1$)

$$r_{\rm dis} = \beta_2 c t_{\rm col} = \frac{c\Delta t}{\frac{1}{\beta_1} - \frac{1}{\beta_2}} = \frac{c\Delta t}{\frac{1}{2\Gamma_1^2} - \frac{1}{2\Gamma_2^2}} \,.$$

Following [67] and assuming $\Gamma_2 = \xi \Gamma_1$ with $\xi > 1$ we obtain for the collision (dissipation) radius

$$r_{\rm dis} = \frac{2\xi^2}{\xi^2 - 1} \Gamma^2 \Delta t \gtrsim 2 t_{\rm var} \frac{\Gamma^2}{(1+z)} \,. \tag{4.24}$$

In our formulation, we assume the collision radius equivalent to the dissipation radius which marks the site where energy is dissipated into kinetic energy, due to the Fermi acceleration. Other models coincident e.g. the radius of the photosphere with the dissipation radius, which is the distance to the central engine from which photons can escape the fireball due to its decreased opacity.

The volume, in which we define the photon energy density, can be assumed to be an infinitesimal thin shell, Δr, with radius $r_{\rm dis}$. The thickness of the shell, Δr is approximated by $\Delta r \sim \Delta t \sim t_{\rm var}/(1+z)$, the time scale of the shell. Therefore it follows for the volume in the stellar frame:

$$\Delta V^* \simeq \Delta\Omega r_{\rm dis}^2 \Delta r = \Delta\Omega \left(2 t_{\rm var} \frac{\Gamma^2}{(1+z)}\right)^2 \left(\frac{t_{\rm var}}{1+z}\right) \,. \tag{4.25}$$

The volume is transformed into the GRB frame as $\mathrm{d}V' = \Gamma \mathrm{d}V^*$.

Now we can write out an expression for the *internal photon energy density*, U'_γ as energy per volume. Note that we derive the density under the assumption we observe on-axis emission ($\mathcal{D} \to \Gamma$) at this point. By this, we reproduce the well-known result [64]

$$\begin{aligned} U'_\gamma = \frac{E'^{\rm shock}_\gamma}{V'_\gamma} &= \left(\frac{t_{\rm var}}{T_{90}}\right) \frac{T^*_{90}}{V^*} \Gamma^2 L'^{\rm \ iso}_\gamma \\ &= \left(\frac{t_{\rm var}}{T_{90}}\right) \frac{T_{90}}{(1+z)} \frac{(1+z)}{\Delta\Omega r_{\rm dis}^2 t_{\rm var}} \Gamma^2 \left(\frac{L^{\rm iso}_\gamma}{\Gamma^4}\right) \\ &= \frac{1}{\Gamma^2} \frac{L^{\rm iso}_\gamma}{4\pi r_{\rm dis}^2} \,. \end{aligned} \tag{4.26}$$

The last step assumes $\Delta\Omega = 4\pi$. This relation was used by John Bahcall and Eli Waxmann for the first discussion of neutrino production in the internal shock model in 1997 [64]. For now, we restrict our derivation to the on-axis case as we will derive a more general formula under the assumption of off-axis emission and a finite jet opening angle in section 5. We will show, that the results can be reduced to the one we obtain here for specific cases.

The observed photon spectrum in the GRB frame $n'_\gamma(\epsilon') = n_\gamma(\epsilon(1+z)/\mathcal{D})$ is given as number of particles per detector area and time. The spectrum multiplied with ϵ' and integrated over $\int \mathrm{d}\epsilon'$ results in the internal energy density. Equation 4.26 serves as normalization

$$U'_\gamma = \int \mathrm{d}\epsilon' \epsilon' n'_\gamma(\epsilon') = \frac{1}{\Gamma^2} \frac{L_\gamma^{\mathrm{iso}}}{4\pi r_{\mathrm{dis}}^2} \,. \tag{4.27}$$

4.2.1 *Optical Depth*

The optical depth describes how often $p\gamma$ interactions occur, compared to the interaction region size and thus is a measure for the neutrino production.
With the photon spectrum and its normalization in Eq. 4.27 we have everything to determine the angular-averaged $p\gamma$ interaction rate in the GRB co-moving frame, as a function of the proton energy, E'_p [64]

$$\frac{1}{t'_{p\gamma}(E'_p)} = \frac{1}{2} \int_{-1}^{1} \mathrm{d}\cos(\phi') \int \mathrm{d}\epsilon' (1 - \beta\cos(\phi')) n'_\gamma(\epsilon') \sigma_{p\gamma}\left(\frac{\epsilon' E'_p}{m_p}(1 - \beta\cos(\phi'))\right) , \tag{4.28}$$

where $\sigma_{p\gamma}$ is the $p\gamma$ inelastic cross section as a function of the photon and proton energy (ϵ' and E'_p respectively) and ϕ' is the interaction angle between the initial proton and photon in the proton's rest frame. The expression is integrated over all interaction angles, as well as over all photon energies [12]. The inverse of Eq. 4.28, $t'_{p\gamma}$ is the $p\gamma$ interaction time scale.

To eventually calculate the optical depth, we compare the interaction time scale with the *dynamical timescale*

$$t'_{\mathrm{dyn}} = r_{\mathrm{dis}}/\Gamma \,. \tag{4.29}$$

This time scale corresponds to the interaction region size, where the Γ factor accounts for the transformation between the GRB jet and the stellar source frame, in which r_{dis} is defined. The optical depth, $\tau_{p\gamma}$, is obtained as the ratio between the interaction time scale and the dynamical time scale

$$\tau_{p\gamma}\kappa = \frac{t'_{\mathrm{dyn}}}{t'_{p\gamma}} \,. \tag{4.30}$$

The additional factor $\kappa \in [0, 1]$ is the *inelasticity* of the $p\gamma$ interaction and gives the amount of energy loss of the leading nucleon, in this case the proton. The inelasticity κ is roughly 0.2 for the $p + \gamma \to \Delta^+$ resonant process [47], but can be larger for multi-pion processes at higher energies.
The higher the interaction rate for a constant interaction region, the higher the optical depth. A high optical depth means, that the GRB environment is opaque and less transparent to photons. With increasing optical depth, more neutrinos are produced due to the increase of $p\gamma$ interactions and the consequent pion production process.

As an additional comment on relativistic motion, we discuss why outflow jets of GRBs are found to be emitted at relativistic velocities. This becomes apparent when considering the *compactness problem*: The observed photons from GRBs are at such high energies, that they are expected to undergo electron-positron pair production and therefore, they should not be detectable. But since we observe such high energetic γ-rays, the optical depth in GRB environments has to be below the unity bound, above which no photons are able to escape from the GRB environment. This paradox can be solved by introducing relativistic motion. Due to the transformation from the Earth frame into the GRB frame, the optical depth is decreased by the Γ factor and makes it possible for photons to escape within the GRB frame and show high energies in the Earth frame at the same time [67].

4.2.2 *Synchrotron Losses*

The production of neutrinos in GRB environments is mainly due to the decay of pions, muons and other hadrons (e.g. kaons). Since these particles are charged, they undergo synchrotron losses in the magnetic fields of the GRB environment before decaying [44]. A consequence of this are features in the neutrino spectra at high energies [12, 47]. A typical neutrino spectrum with synchrotron losses is shown in Fig. 17a. The neutrino production at high energies above 10^7 GeV shows steeply falling suppression features in its behaviour. This steep decrease in the number of produced neutrinos occurs in multiple steps, corresponding to the different secondaries and their lifetimes. The mean life-time of the secondary particles are 2.2×10^{-6}s for muons, 2.6×10^{-8}s for charged pions and 1.24×10^{-8}s for kaons [59]. Secondaries with a short lifetime are affected less by synchrotron losses. We conclude from this, that muons cause the first steep decrease in the spectrum. Without synchrotron losses, the neutrino spectrum behaves very smooth as shown in Fig. 17b. The initial steep increase originates from the photon spectrum, the cut-off from the proton spectrum. Studies showed that a simple power-law with two breaks neglects important features, such as the discussed synchrotron losses [38]. The spectrum without synchrotron losses in Fig. 17b is achieved by setting the magnetic field strength for the synchrotron loss calculations to zero. In this case, the suppression of neutrino production at higher energies is only due to the maximal proton energy that can be reached in the GRB environment. We conclude that the overall shape from a neutrino spectrum is mostly dominated by the target and proton spectrum, while the synchrotron losses add characteristic features. As mentioned, the first steep fall in Fig. 17b is caused by the suppression of neutrinos from muons. The following “steps” in the spectrum are not as easy to determine, because it is most likely the combined effect of synchrotron losses and the overall suppression of high energetic neutrino due to the maximum proton energy.

In the next chapter, we will see that the proton spectrum as a function of energy is proportional to an exponential cut-off at the maximal proton energy. This cut-off energy marks the decrease in the neutrino spectra in Fig.17.

The energy losses caused by synchrotron radiation depend on the magnetic field strength in the GRB jet. We can infer the energy of the magnetic field from the photon energy density, given in Eq. 4.27, by introducing new parameters: The *bolometric energy fraction* of the magnetic field (ϵ_B), electrons (ϵ_e) and protons (ϵ_p) as well as the *baryonic loading* ($f_e = \epsilon_e/\epsilon_p$). Bolometric means integrated over all wavelengths and the baryonic loading

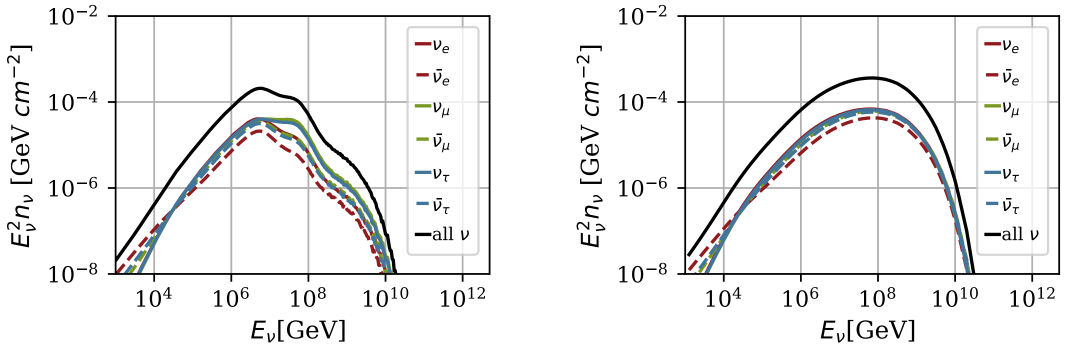

(a) Default GRB spectrum with synchrotron losses.

(b) Default GRB spectrum without synchrotron losses.

FIG. 17. Comparison of neutrino spectrum with consideration of synchrotron loses of secondary particles (right) and without synchrotron losses (left). The synchrotron losses cause the suppression of neutrino production at higher energies. Notable effects occur in steps, which depend on the lifetime of the secondary particles. The suppression for neutrinos without synchrotron losses depends only on the maximal reachable proton energy (see section 4.2.3).

is the ratio between baryonic (protons, neutrons) and non-baryonic (leptons, photons) components in the GRB. We use that ϵ_e and ϵ_B are defined as $U_B/U_e = \epsilon_B/\epsilon_e$ and $U_e \simeq U_\gamma$, under the assumption that the non-baryonic components of the GRB have the same energy density. With $U'_B = B'^2/2$ we write

$$\begin{aligned} B' &= \sqrt{2\frac{\epsilon_B}{\epsilon_e}U'_\gamma} \\ &= \sqrt{2\frac{\epsilon_B}{\epsilon_e}\frac{1}{\Gamma^2}\frac{L_\gamma^{\rm iso}}{4\pi r_{\rm dis}^2}} \\ &= \sqrt{2\frac{\epsilon_B}{\epsilon_e}\frac{1}{\Gamma^2}\frac{L_\gamma^{\rm iso}}{4\pi}\frac{(1+z)^2}{4\Gamma^4 t_{\rm var}^2}} \,. \end{aligned} \tag{4.31}$$

The synchrotron loss of charged particles in a magnetic field of the strength B' per time interval dt in the GRB frame and averaged over all possible magnetic field orientations is given as [44, 52]:

$$-\frac{dE'}{dt'} = \frac{16\pi}{9} Z^4 \alpha^2 \frac{E'^2 B'^2}{m^4} \,, \tag{4.32}$$

where E' and m are energy and mass of the particle and Z is the proton number - which equals to one for protons. α is the fine structure constant ($\sim 1/137$ in our units) and B' is given in Eq. 4.31. The energy loss is more drastic for light particles ($\propto 1/m^4$) and therefore influences the secondary pions ($m_\pi \sim 140$ MeV), kaons ($m_K \sim 500$ MeV) and muons ($m_\mu \sim 105$ MeV) more than protons ($m_p \sim 1$ GeV) [59]. As we already discussed, also the life-time of the particles plays a crucial role for synchrotron losses. The higher the energy of the particle, the stronger the synchrotron loss. This means in specific for the protons in the GRB environment, that above a certain maximal energy the loss due to synchrotron losses might be stronger than the gain from acceleration. Synchrotron loss is one of the restrictive mechanisms which can limit the maximal proton energy in the GRB frame as we will see in the next section.

4.2.3 *Proton Flux*

Neutrinos are produced in the interaction of protons with γ-rays and other hadrons. The successful observation of a neutrino flux coming from a GRB would serve as a "smoking-gun" signal for the acceleration of CRs. We assume, that CRs are dominated by protons. The proton spectrum follows a power-law function with exponential cutoff and spectral index γ. We formulate an ansatz accordingly

$$n_p(E_p) \propto E_p^{-\gamma} e^{-E_p/E_{p,\max}}\,. \tag{4.33}$$

Combining the power law and exponential cut-off with the photon spectrum we introduced in section 3.4 explains already roughly the shape of the neutrino spectrum with its two breaks, originating from the photon and the proton part of the spectrum. All additional features can be explained by synchrotron losses as just discussed.

With the baryonic loading f_e the proton energy density at the source is estimated as $U_p' = U_e'/f_e$. If protons would not undergo interactions and deflections on their way from the GRB source to Earth, one could approximate the proton energy density according to the photon density $U_p' = U_\gamma'/f_e$. This serves as a normalization for the spectrum Eq. 4.33. Following the procedure for the internal photon energy density (Eq. 4.27), one integrates the proton spectrum multiplied by the energy for the proton energy density

$$\int \mathrm{d}E_p' E_p' n_p'(E_p') = \frac{1}{f_e} U_\gamma'\,. \tag{4.34}$$

Besides the integral spectral index γ, $E_{p,\max}$ is the only other unknown parameter in Eq. 4.33. The spectral index we are using is the index at the source and is assumed to be 2.0. This value is inferred from Fermi acceleration. For the CR spectrum we observe at Earth, which is shown in Fig. 1, one measures a spectral index of 2.7 instead. This difference of roughly 0.7 is due to propagation effects, which cause the proton spectrum to become softer.

To determine $E_{p,\max}$, we compare the proton's energy gain due to Fermi acceleration with energy loss effects. Loss effects are synchrotron radiation, losses due to the $p\gamma$ interaction themselves and adiabatic losses of the expanding shell, which can be estimated by the dynamical time scale. Not all these effects depend on the proton energy E_p', but

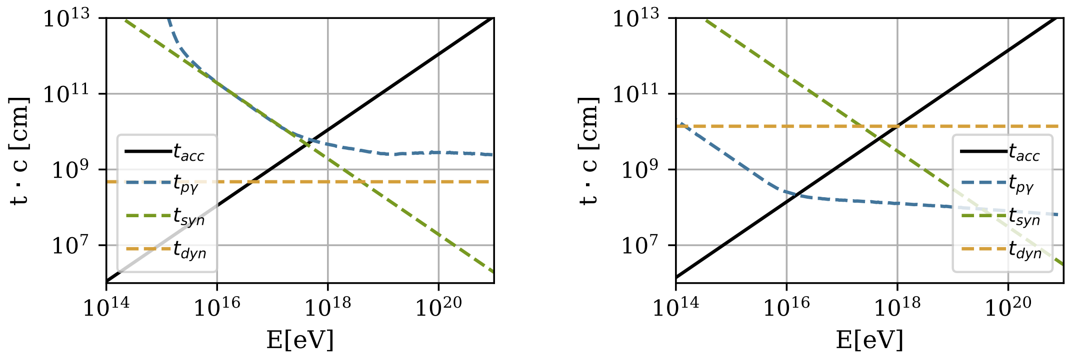

(a) The competing time scales for Γ=316. In this case the time scale denoting the losses due to the size of the acceleration region is the strongest limitation and therefore marks $E_{p,\max}$ at $\sim 4.5 \times 10^{16}$ eV.

(b) Time scales for Γ=10. Here the time scale denoting the $p\gamma$ interaction wavelength is the strongest limitation and determines $E_{p,\max} \sim 1.13 \times 10^{16}$ eV.

FIG. 18. Variation of the time scales in the GRB frame for two different sets of GRB parameters. The timescales are multiplied by c and therefore expressed as length scales.

they can all be expressed in terms of a time scale [41]. We summarize the time scales for completeness

$$t'_{\mathrm{acc}} = \frac{1}{\eta}\frac{1}{4\pi\alpha}\frac{E'_p}{B'}\,, \tag{4.35}$$

$$t'_{adi} = t'_{\mathrm{dyn}} = \frac{r_{\mathrm{dis}}}{\Gamma} = \frac{2\Gamma t_{\mathrm{var}}}{1+z}\,, \tag{4.36}$$

$$t'_{\mathrm{syn}} = \frac{9}{16\pi}\frac{1}{\alpha^2}\frac{m_p^4}{E'_p B'^2}\,, \tag{4.37}$$

$$t'_{p\gamma} = \frac{t'_{\mathrm{dyn}}}{\tau_{p\gamma}\kappa}\,. \tag{4.38}$$

The time scale $t'_{p\gamma}$ was found in Eq. 4.30, t'_{dyn} in Eq. 4.29 and t'_{syn} is obtained from Eq. 4.32 via $t'_{\mathrm{syn}} = E'/\frac{\mathrm{d}E'}{\mathrm{d}t'}$ [41]. The acceleration time scale is approximated as the inverse gyroradius for the proton in Heaviside-Lorentz units. The factor η describes the acceleration efficiency.

To find the maximal proton energy we solve the following equation for E'_p, which compares the time scale corresponding to energy gain with the time scales of energy losses

$$\frac{1}{t'_{\mathrm{acc}}} = \frac{1}{t'_{\mathrm{dyn}}} + \frac{1}{t'_{\mathrm{syn}}} + \frac{1}{t'_{p\gamma}}\,. \tag{4.39}$$

To get intuition for the dominating energy loss effect, we compare the loss time scales (Eq. 4.36- 4.38) separately with t'_{acc} in Eq. 4.35 via $t'_{\mathrm{acc}} = t'_{\mathrm{loss}}$ and solve for $E_{p\max}$. By doing this, we find three maximal proton energies corresponding to the three loss terms. The minimal energy of those three gives an approximation for the overall $E_{p,\max}$ determined in Eq. 4.39.

The individual time scales and their dependency on the energy in the GRB frame are shown in Fig. 18 for two different sets of GRB parameters. The choice of GRB parameters and thus the internal quantities have a large effect on the nature of the dominating loss effect. The point of intersection with the acceleration time scale line (black line) determines the maximal proton energy that the individual loss effects allow. The minimum of these maximum proton energies approximates $E_{p,\mathrm{max}}$. The time scales in Fig. 18, are multiplied with c to show length scales rather than time scales. For the dashed yellow curve, which is t_{dyn}, we get a value for the interaction radius in which neutrinos can be produced. This is constant over time.

4.2.4 *Neutrino Flux*

Finally, the neutrino spectrum in the GRB frame for a neutrino of flavour α is given as a combination of all quantities and effects we discussed [12, 14]

$$n'_{\nu_\alpha}(E'_\nu) \simeq \sum_\beta P_{\alpha\beta} \int \mathrm{d}E'_p \left(\frac{1-e^{-\kappa\tau(E'_p)}}{\kappa}\right) \frac{\mathrm{d}N_{\nu_\beta}}{\mathrm{d}E'_\nu}(E'_p, E'_\nu) n'_p(E'_p)\,, \tag{4.40}$$

where $P_{\alpha\beta}$ is the oscillation probability matrix, $\frac{\mathrm{d}N_{\nu_\beta}}{\mathrm{d}E'_\nu}$ determines the production of neutrinos with energy E'_ν as a function of the proton energy E'_p and n'_p is the proton flux from Eq. 4.33 (in the GRB frame). The term, which depends exponentially on the optical depth, accounts for an increase of neutrinos with higher internal photon densities, thus higher opacity. For large opacities with $\tau(E'_p) \gg 1$, this term reduces to $1/\kappa$ and the neutrino spectrum follows the proton spectrum only limited by $1/\kappa$. For small opacities with $\tau(E'_p) \ll 1$, the neutrino spectrum is proportional to the product of the proton spectrum and the optical depth, as the exponential term reduces to $\tau(E'_p)$. The integration over the proton's energy results in the neutrino spectrum, which consequently depends only on the neutrino energy. To calculate the neutrino spectrum of flavour α at the source, the sum over the oscillation probability matrix $P_{\alpha\beta}$ is neglected. The resulting spectra of neutrinos from this calculation have already be shown for exemplary cases in Fig. 17 and Fig. 19.

To understand Eq. 4.40 better consider the simplified case, for which neutrinos are only produced from decaying pions (and thus $\kappa \sim 1/5$), no synchrotron losses are incorporated and $\tau(E'_p) \gg 1$. For neutrinos from pion decay, we assume that the pion carries the fraction κ of the protons initial energy, as this is defined as the energy loss of the proton. Furthermore, we reckon that all four final state particles from the pion and following muon decay carry the same amount of energy. This means that $E'_\nu = \kappa E'_p/4$, which can be used to constrain the proton energy for the neutrino production as

$$\begin{aligned} \frac{dN_\nu}{dE'_\nu}(E'_p, E'_\nu) &= K_\pi \delta(E'_\nu - \frac{\kappa E'_p}{4}) \\ &= \frac{4}{\kappa}\delta(E'_p - \frac{4E'_\nu}{\kappa})\,. \end{aligned} \tag{4.41}$$

The factor K_π determines the fraction of charged pions compared to neutral pions and is in our case approximated to be 1/2. Note again, that this is only an approximation and looks somewhat more complicated when including synchrotron losses. Now, let us write out the the spectrum for one neutrino flavour α

$$\begin{aligned} n'_\nu &\simeq \int \mathrm{d}E'_p \frac{1}{\kappa} K_\pi \frac{4}{\kappa} \delta(E'_p - \frac{4E'_\nu}{\kappa}) n'_p(E'_p) \\ &= \frac{4K_\pi}{\kappa^2} \, n_p(\frac{4E'_\nu}{\kappa}) \, . \end{aligned} \tag{4.42}$$

Multiplying both sides of Eq. 4.42 with E'^2_ν and using $E'_p = 4E_\nu/\kappa$ gives the well known result [41, 64]

$$\begin{aligned} E'^2_\nu n_\nu &\simeq \frac{K_\pi}{4} \left(\frac{4E'_\nu}{\kappa}\right)^2 n_p(\frac{4E'_\nu}{\kappa}) \\ &= \frac{K_\pi}{4} E'^2_p \; n_p(E'_p) \, . \end{aligned} \tag{4.43}$$

With $K_\pi = 0.5$ and the sum over the all flavours Eq. 4.43 simplifies to

$$E'^2_\nu n'_\nu = \frac{3}{8} E'^2_p n_p(E'_p) \, . \tag{4.44}$$

4.2.5 *Neutrino Oscillations*

In section 2, we introduced neutrino oscillations. We mentioned that neutrinos are produced in flavour ratios of roughly 1:2:0 for $\nu_e : \nu_\mu : \nu_\mu$ at the GRB site. As a result of the long travel distances and limited detector resolution, only the oscillations-averaged flavours with a ratio of 1:1:1 for $\nu_e : \nu_\mu : \nu_\mu$ can be detected. In Fig. 19 we show the neutrino spectrum and its neutrino flavour components without (Fig. 19a) and with the effect of oscillation (Fig. 19b), which corresponds to the spectrum at the source and at Earth.

Comparing the two spectra, we deduce that there is a significant tau neutrino (anti-neutrino) component with oscillation, as expected. The black envelope curve in Fig. 19, which is the sum of all neutrino flavours, stays constant as the number of particles should stay constant as well as its energy distribution. The individual contributions are expected to change their contribution, as can be seen clearly when looking at the curves for electron and muon neutrinos and anti-neutrinos. The flux of muon neutrinos at the source is higher than at the Earth, which is to explain by the strong $\nu_\mu \leftrightarrow \nu_\tau$ mixing. Because of this mixing, approximately half of the muon neutrinos will be detected as tau neutrinos. Therefore, the number of muon neutrinos appears to be decreased when comparing Fig. 19a and Fig. 19b and the tau neutrino curve follows closely the muon neutrino curve. The fact that also the shape of the electron neutrino curve is changing can be explained by the probabilities for electron neutrinos oscillating into muons and tau neutrinos along the way. The mixing is not exactly a change of ratio from 1:2:0 to 1:1:1, as we already discussed in section 2.1.3.

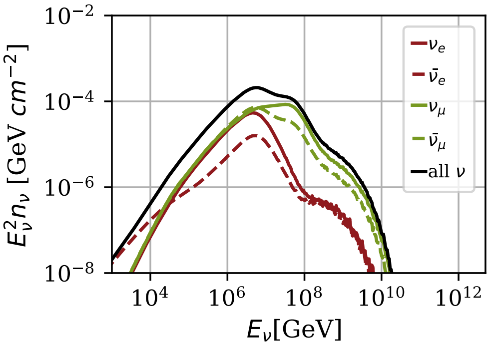

(a) Arbitrary GRB spectrum without oscillations.

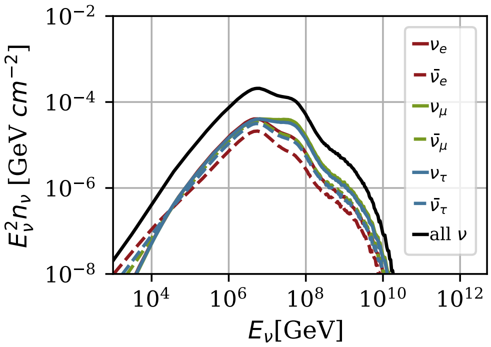

(b) Arbitrary GRB spectrum with oscillations.

FIG. 19. GRB spectrum with (right) and without (left) consideration of neutrino oscillations. The sum of neutrinos (black curve) stays constant, while the individual neutrino contributions vary.

4.3 NEUTRINO PREDICTIONS WITH FIREBALLET

In this thesis, we use the IceCube software FIREBALLET to calculate the actual neutrino flux in Eq. 4.40 for given sets of GRB parameters based on the internal shock fireball model. In its original form, FIREBALLET can be used to predict neutrino fluxes based on on-axis γ-ray observations. In this section, we introduce the framework itself. We show all results based on realistic GRB parameters, which we introduce in section 4.3.2. They are taken from [41] and cover a good variety of typical GRB parameters.

4.3.1 FIREBALLET: *A Fireball Emission Tool*

All assumptions and calculations which are done in section 4 are combined in the software framework FIREBALLET. The initial version from 2012 was implemented by M. Ahlers to predict the neutrino emission from GRBs based on input parameters from non-neutrino observations. The underlying model assumption is the relativistic fireball internal shock scenario.

The neutrino predictions in FIREBALLET take the full $p\gamma$ interaction chain into account, thus general resonance excitations and decays, direct single pion production and diffractive and non–diffractive multi-particle production are included, as discussed in section 2.2. For this intention, the Monte-Carlo Code SOPHIA [47] is deployed within FIREBALLET. SOPHIA calculates the cross section of hadronic interactions between relativistic nucleons and target photons over the whole energy range, taking into account the full $p\gamma$ chain. Additionally, to this, synchrotron losses of intermediate particles are included as an extra Monte-Carlo step within FIREBALLET. This is done separately and is not part of the SOPHIA code.

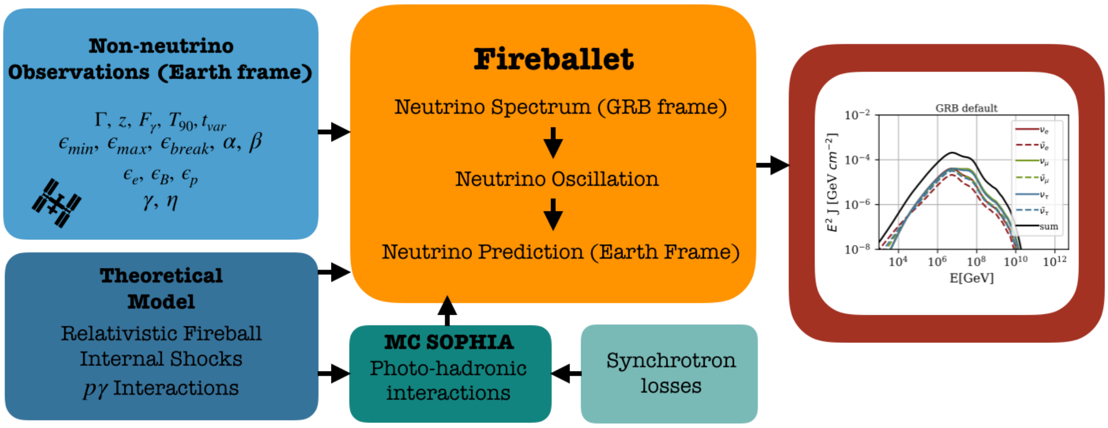

FIG. 20. Schematic Illustration of FIREBALLET.

Figure 20 illustrates the framework as a flow chart, starting from simple input parameters and leading to the visualized neutrino spectra. As input parameters are the quantities required, which we discussed in the last chapters: the Lorentz boost Γ, redshift z, duration of the burst T_{90}, the γ-ray fluence $\mathcal{F}_\gamma$, the variability timescale $t_{\rm var}$, parameters describing the photon spectrum ($\epsilon_{\rm min/max}, \epsilon^{\rm instr.}_{\rm min/max}, \epsilon_{\rm break}, \alpha, \beta$), the bolometric energy fractions of the magnetic field ϵ_B, electrons ϵ_e and protons ϵ_p, spectral index of the proton spectrum γ and the acceleration efficiency of the protons η. Because FIREBALLET predicts the neutrino flux based on observations in the Earth frame, it is internally defined such that all parameters have to be forwarded in the Earth frame. With these parameters, and the theoretical assumptions of the fireball model, FIREBALLET calculates the internal GRB quantities as the optical depth and the proton energy. It includes the $p\gamma$ cross section from the SOPHIA code and additional synchrotron losses. In the last step neutrino oscillations are applied and a boost into the Earth frame is accomplished before one obtains neutrino spectra from the output files of FIREBALLET.

The software is equipped with various options that can be set by the user if desired. For example, one can choose whether neutrino oscillation should be included or not. With this approach, the neutrino spectrum in terms of individual flavours induced at the source and detected at Earth can be calculated, as illustrated in Fig. 19, section 4.2.5. Furthermore, the photon spectrum can be approximated either with the broken power-law or Band spectrum and it is possible to reduce pion production only to $p\gamma$-resonances. For further details about the software and the SOPHIA Code please refer to [12, 47]. The GRB default parameters are listed in [12].

4.3.2 *Standard GRB Parameters*

Here, we give a brief introduction into the standard GRB model parameter we chose to illustrate our results. For all following discussions, we compare 3 different sets of GRB parameters, covering a variety of possible parameter configurations and illustrating different temporal stages within the GRB emission. We consider one configuration being an example of prompt GRB emission with high Lorentz factor $\Gamma = 1000$, and two models for extended emission (moderate and optimistic in terms of detection, denoted as EE

	EE Moderate	EE Optimistic	Prompt
Γ	30	10	10^3
L_{iso} [erg/s]	3×10^{48}	3×10^{48}	10^{51}
E_{iso} [erg]	10^{51}	10^{51}	10^{51}
r_{dis} [cm]	10^{14}	3×10^{13}	3×10^{13}
ϵ_{min} [eV]	300.	300.	10^4
ϵ_{max} [eV]	10^4	10^4	10^6
ϵ_{break} [eV]	10^3	10^4	5×10^5
$\mathcal{F}_\gamma$ [erg/cm^2]	9.29×10^{-5}	9.29×10^{-5}	9.29×10^{-5}
T_{90} [s]	333	333	1.0
t_{var} [s]	1.97	5.32	5.32×10^{-4}

TAB. 1. FIREBALLET input parameters for three different "textbook" GRB models [41, 49].

Moderate and EE Optimistic) with lower Lorentz factors of $\Gamma = 10$ and 30. The two EE late-time emission models are caused by extended late-time activities of the central engine but are still assigned to internal shock mechanisms. These three "textbook" models and their corresponding parameters are taken from [41], based on [49]. The parameters are summarized in Tab. 1.

Additional parameters, which are the same for all three cases, are a luminosity distance of d_L=300 Mpc (which corresponds to a redshift of z=0.064), energy fractions for baryons $\epsilon_b = 0.1$ and electrons $\epsilon_e = 1.0$, baryonic loading $1/f_e = 10.0$, α=0.5, β=2.0, a proton spectral index of γ= 2.0 and an acceleration efficiency of $\eta = 1.0$. The limits for the internal photon spectrum in the Earth frame, $\epsilon'^{\text{true}}_{\text{min}}$ and $\epsilon'^{\text{true}}_{\text{max}}$ are given as 0.1 and 1.0×10^6 eV respectively [41]. To pass them onto FIREBALLET correctly, they have to be transformed into the GRB frame via $\epsilon = \epsilon'\mathcal{D}/(1 + z)$ for all three sets of parameters individually as $\mathcal{D} \to \Gamma$ is different for all three cases. The break energy ϵ_{break} in Tab. 1 is given in the Earth frame and thus no transformation is required. Note, that the initial FIREBALLET configuration uses the $\mathcal{D} \to \Gamma$ approximation for the Doppler factor.

The values for T_{90}, $\mathcal{F}_\gamma$, and t_{var} in the lower part of Tab. 1 are obtained from by Eq. 4.20, Eq. 4.17 and Eq. 4.24 with the given parameters in the upper part of Tab. 1. The limits ϵ_{min} and ϵ_{max} are chosen to agree with the energy range covered by the Swift XRT for the two late-time emission models, and by the Fermi GBM detectors for the prompt emission.

Validation

For the input parameters as given in Tab. 1, we obtain the neutrino spectra shown in Fig. 21a. To compare the result achieved with FIREBALLET with the one in [41], we set the option to only include $p\gamma$-interaction via resonances. Furthermore, we show the result under the assumption, that the only considered resonance is the in section 2.2 discussed Δ^+ resonance. These are the same assumptions made in [41] and thus, the comparison is justified. We show all three curves, corresponding to the three models, as the neutrino spectrum per flavour.

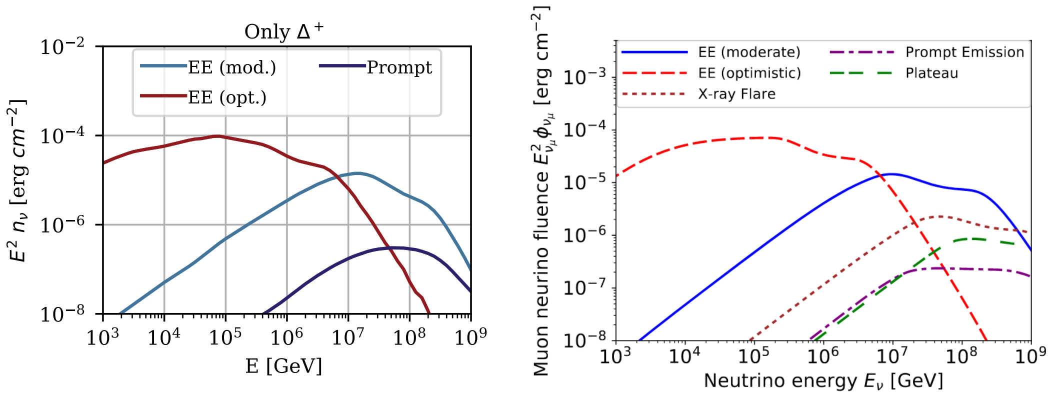

(a) (b)

FIG. 21. Comparison of our results (a) with the ones given in [41] (b). Note, that we only give the result in units of [erg cm^{-2}] here to compare with the plot on the right. Following plots will be given in [GeV cm^{-2}].

In [41], two additional models are shown, the X-ray and Plateau emission. Both are also models for internal shock induced neutrinos, but due to their similarity in Γ and other parameters, we are only focusing on the three models we introduced in section 4.3.2. Therefore, the comparison between Fig. 21a and Fig. 21b is restricted to the prompt and extended emission models. The comparison shows great agreement and we conclude, that we are capable to reproduce established results with FIREBALLET and the given parameters. This marks a great justification and starting point for further spectrum studies.

It should be mentioned that in the following, we only consider neutrino spectra that are based on cross section calculations where the full $p\gamma$ interaction chain is considered. This is a more physically realistic treatment of the calculation and one of the big achievements of the combined usage of FIREBALLET and SOPHIA.

5 OFF-AXIS NEUTRINO PREDICTIONS

So far, we considered all GRB quantities and their transformations regardless of the jet geometry as its expansion in polar and azimuthal dimensions. In the following, we will derive an effective expression for the Doppler factor, which takes into account a finite jet opening angle. As we will see, this modification has effects on the values for the Doppler factor and its scaling as a function of the viewing and opening angle.

We will start the derivation by following an alternative approach for the scaling of the fluence and the isotropic equivalent luminosity with the Doppler factor in a more general formalism, by defining a norm factor and an effective Doppler factor. These two factors are used to describe the off-axis emission and the opening angle of the emission jet. We investigate how the norm factors behave as functions of the off-axis and opening angle, and how the photon and neutrino spectra are affected. In the second part of this chapter, we will show how these modifications affect the neutrino spectra obtained from FIREBALLET, which has to be modified in order to account for our generalization. Eventually, we briefly introduce how our derived analytical formalism can easily be extended to describe structured GRB jets in section 5.6.

5.1 NORMALIZATION FACTOR N_{jet}

We introduce the *emissivity*, j_ν [erg cm^{-3} sr^{-1} s^{-1} Hz^{-1}], the energy emitted per unit volume, solid angle, time and frequency as

$$j_\nu = \frac{\mathrm{d}E}{\mathrm{d}V \; \mathrm{d}\Omega \; \mathrm{d}t \; \mathrm{d}\nu} \,. \tag{5.1}$$

We use that $j_\nu = \mathcal{D}^2/(1+z)^2 j'_\nu$ [67] and take the transformation properties of $\mathrm{d}V$, $\mathrm{d}\Omega$, $\mathrm{d}t$ and $\mathrm{d}\nu$ we found in section 4.1. Additionally, we include the cosmological redshift effect, which was previously neglected for simplicity. We write for $\mathrm{d}E/\mathrm{d}\Omega$ in the GRB frame, where primed quantities are again in the GRB frame, while quantities without a prime or star are in the Earth frame:

$$\begin{aligned}\frac{\mathrm{d}E}{\mathrm{d}\Omega} &= \left(\frac{\mathcal{D}^2}{(1+z)^2} j'_\nu\right)\left(\frac{\mathcal{D}}{(1+z)}\mathrm{d}V'\right)\left(\frac{(1+z)}{\mathcal{D}}\mathrm{d}t'\right)\left(\frac{\mathcal{D}}{(1+z)}\mathrm{d}\nu'\right) \\ &= \frac{\mathcal{D}^3}{(1+z)^3} j'_\nu \; \mathrm{d}V' \; \mathrm{d}t' \; \mathrm{d}\nu' \,. \end{aligned} \tag{5.2}$$

The emission in the GRB frame is assumed to be isotropic in the co-moving frame. Therefore, the time-integrated emissivity can be expressed by the local photon density n'_γ as

$$\int j'_\nu \mathrm{d}t' = \frac{1}{4\pi} n'_\gamma \epsilon'_\gamma \,. \tag{5.3}$$

Integrating Eq. 5.3 over $\mathrm{d}\nu_\gamma \sim \mathrm{d}\epsilon_\gamma$ leads to $U'_\gamma/(4\pi)$, following Eq. 4.27 in section 4.2. Additionally, we use the definition for the angular diameter distance $d_A^2 = \mathrm{d}A/\mathrm{d}\Omega$ and its relation to the luminosity distance $d_A = d_L/(1+z)^2$ and rewrite Eq. 5.2

$$\frac{\mathrm{d}E}{\mathrm{d}A} = \frac{1+z}{4\pi d_L^2} \int \mathcal{D}^3\ U'_\gamma\ \mathrm{d}V'\,. \tag{5.4}$$

The quantity $\mathrm{d}E/\mathrm{d}A$ is the known energy fluence $\mathcal{F}_\gamma$. Transforming the volume element into the stellar frame $\mathrm{d}V' = \Gamma \mathrm{d}V^*$ and using the expression for $\Delta V^* = r_{\text{dis}}^2 \Delta r \mathrm{d}\Omega^*$ from Eq. 4.25 we find for the energy fluence per shell

$$\mathcal{F}_\gamma = \frac{1+z}{4\pi d_L^2} r_{\text{dis}}^2 \Delta r \int \Gamma\ \mathcal{D}^3\ U'_\gamma\ \mathrm{d}\Omega^*\,. \tag{5.5}$$

As we want to derive a generalization of the Doppler factor which includes information on the jet geometry, we rewrite the Doppler factor from Eq. 4.7 in section 4.1 as a function of the Lorentz factor Γ and solid angle Ω^*

$$\mathcal{D}(\Omega^*) = \frac{1}{\Gamma(1-\beta\cdot\hat{n}(\Omega^*)\cdot\hat{n}_{obs})}\,. \tag{5.6}$$

We choose a coordinate system in which the jet axis is aligned with the z-axis and the line-of-sight axis of the observer has an angle θ_v to the z-axis. The observer and jet axis are both defined as unit vectors. The expression $\beta\cdot\hat{n}(\Omega^*)$ is defined as a radial unit vector multiplied with the velocity of a volume element in the GRB frame. The unit vector $\hat{n}_{obs}$ points towards the observer. Figure 22a shows the two vectors $\hat{n}(\Omega^*)$ and $\hat{n}_{\text{obs}}$ in the chosen coordinate system, in which the z-axis is in line with the jet axis, which corresponds to $\hat{n}(\Omega^*)$ for $\theta^* = 0$. This arbitrary choice allows simple calculations, but we could have also chosen a different coordinate system to work with. In our convention, we write

$$\hat{n}(\Omega^*)\cdot\hat{n}_{obs} = \begin{pmatrix}\cos(\alpha^*)\ \sin(\theta^*)\\ \sin(\alpha^*)\ \sin(\theta^*)\\ \cos(\theta^*)\end{pmatrix}\cdot\begin{pmatrix}\sin(\theta_v)\\ 0\\ \cos(\theta_v)\end{pmatrix}\,, \tag{5.7}$$

where α^* and θ^* denote the azimuthal and polar angle of the jet, and θ_v is the viewing angle with respect to the jet axis. For Eq. 5.6 follows therefore

$$\mathcal{D}(\Omega^*) = \frac{1}{\Gamma\left(1-\beta\left(\cos(\alpha^*)\sin(\theta^*)\sin(\theta_v)+\cos(\theta^*)\cos(\theta_v)\right)\right)}\,. \tag{5.8}$$

The special expression for the Doppler factor in Eq. 4.7 in section 4.1 is can be reproduced from Eq. 5.8 for $\theta^* = 0$. This special case takes only one viewing angle θ_v into account. But instead, one rather has to integrate over all angles, defined by the observer and jet vectors, that are positioned inside the jet (defined by θ^* and α^*) as they all contribute to the observation. This is illustrated in Fig. 22b. It becomes clear, that all infinitesimal emission regions (*blobs*, small grey circles) along the top of the jet are observed from a different observation (viewing) angle (blue lines). This intuition of the jet pictures the so-called *top-hat jet*. It assumes, that the Γ-factor is evenly distributed at the *top* of the jet. The jet is characterized by sharp edges, which means there are no emitting *blobs* outside the region defined by the opening angle.

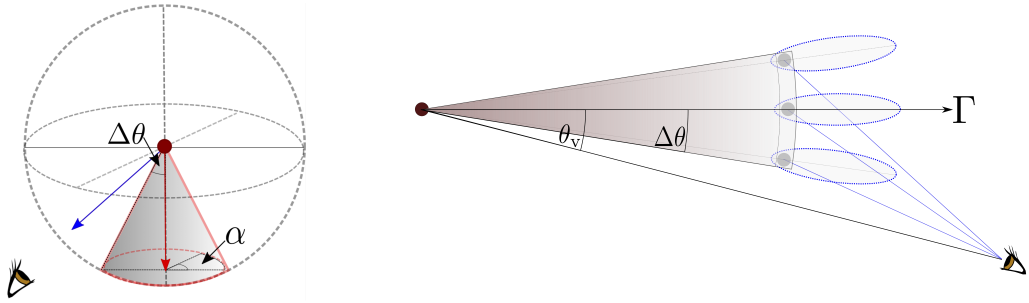

(a) Spherical coordinate system in the stellar frame to illustrate the jet vector $\hat{n}(\Omega^*)$ (red), which has to be integrated in polar (θ^*) and azimuthal (α^*) direction. The blue arrow shows the observation axis, $\hat{n}_{\text{obs}}$. The central engine is located in the center of the sphere with radius r_{dis}.

(b) Illustration of the jet with half opening angle $\Delta\theta$ and viewing angle θ_v in the $\theta - z$ plane. From every infinitesimal blob (grey circles) the emission is maximally boosted along a different direction. Therefore, the observer receives emission as a superposition from many different observation angles (drawn as blue lines).

FIG. 22. Illustrations for extended GRB jet geometry with opening angle $\Delta\theta$ and azimuthal angle α^*.

Another rarely discussed picture for neutrino predictions from GRBs is the *structured* jet, where Γ is a function of the polar angle θ^*. This function is defined such that no "sharp" edges occur [57]. Even though this seems to be a more realistic scenario describing nature, we restrict our following studies primarily on the top hat jet. After introducing the general formalism, the description can easily be extended to a structured description, as we will discuss briefly in section 5.6.

From Fig. 22b we understand, that the different *blobs* for a top-hat jet move along different directions (grey lines). This results in different viewing angles for the observer for every single emitting element. As studied in section 4.1, the Doppler factor differs depending on the viewing angle. Thus, also the emission that is boosted towards the observer changes with the viewing angle and therefore, all elements are boosted with a different $\mathcal{D}$. While the previous $\mathcal{D}$ definition considers only one single *blob* with one defined angle to the observer's line of sight, Eq. 5.5 integrates over all viewing angles with the generalization of $\mathcal{D}(\Omega^*)$ in Eq. 5.6. As we will see, the "simplified" Doppler factor defined in Eq. 4.7 can be used as an approximation for specific configurations of Γ, θ_v and $\Delta\theta$, but is not a general valid description.

We replace $\mathcal{D}^3$ from Eq. 4.7 in section 4.1 by $\mathcal{D}(\Omega^*)^3$ in Eq. 5.6 and write out the integral in Eq. 5.5. The integration interval is for θ between 0 and the half jet opening angle $\Delta\theta$, α^* is integrated from 0 to 2π assuming a symmetric jet in azimuthal direction. We find for the energy fluence per shell

$$\mathcal{F}_\gamma = \frac{1+z}{4\pi d_L^2} r_{dis}^2 \Delta r \int_0^{2\pi} \mathrm{d}\alpha^* \int_0^{\Delta\theta} \mathrm{d}\theta^* \sin(\theta^*) \Gamma \left(\frac{1}{\Gamma(1-\beta\cos(\Omega^*))} \right)^3 U'_\gamma \,. \tag{5.9}$$

It should be mentioned that Eq. 5.9 can be extended to the fluence for the entire burst by replacing the single sub-shell time scale, $\Delta r = t_{\text{var}}$ with $T_{90}/(1+z)$, describing the total burst duration in the stellar frame.
For simplicity we introduce a notation for the third power angular integrated Doppler factor multiplied with Γ in Eq. 5.9:

$$\mathcal{N}_{\text{jet}} := \int\limits_{\Delta\Omega_{jet}} \mathrm{d}\Omega^* \; \Gamma \; \mathcal{D}(\Omega^*)^3 \,. \tag{5.10}$$

Note at this point that in our case, Γ is not angular-dependent and is treated only as a constant in the integration. For the above mentioned structured jet, Γ would depend on Ω^*. Therefore, we use the notation where Γ is already explicit in the integral to make a transition to the structured jet more transparent.
Furthermore, we assume that the photon density U'_γ is constant along the jet expansion and thus is also treated outside the integration.

We rewrite Eq. 5.9 including $\mathcal{N}_{\text{jet}}$:

$$\mathcal{F}_\gamma = \frac{1+z}{4\pi d_L^2} r_{dis}^2 \Delta r \mathcal{N}_{\text{jet}} U'_\gamma \,. \tag{5.11}$$

Comparing Eq. 5.11 with the expression for the fluence in Eq. 4.27, we identify

$$\mathcal{F}_\gamma = \frac{1+z}{4\pi d_L^2} E'^{\text{shock}} \,, \tag{5.12}$$

where we use once again the relations $\Delta r = t_{\text{var}}$ and $E'^{\text{shock}} = \frac{t_{\text{var}}}{T_{90}} E'^{\text{iso}}$ from section 4.2. From this follows naturally the formulation of the internal photon energy as

$$\begin{aligned} U'_\gamma &= \frac{E'^{\text{shock}}_\gamma}{t_{\text{var}} r_{\text{dis}}^2 \mathcal{N}_{\text{jet}}} \\ &= \frac{L_\gamma^{\text{iso}}}{r_{\text{dis}}^2 \mathcal{N}_{\text{jet}}} \,. \end{aligned} \tag{5.13}$$

This formulation allows to directly set this result in contrast to the same formulation based on the special ("naive") approach in Eq. 4.26 in section 4.2, which takes no angular dependencies into account. To do so, we compare Eq. 5.13 with Eq. 4.26. We recognize, that in our new formalism the factor $\mathcal{N}_{\text{jet}}$ is a general replacement for the factor $4\pi\Gamma^2$. As we will see, for specific cases, $\mathcal{N}_{\text{jet}}$ becomes $4\pi\Gamma^2$ and thus is capable of reproducing previous results.

In the following, the behaviour of $\mathcal{N}_{\text{jet}}$ depending on it's variables Γ, θ_v and $\Delta\theta$ is investigated. Figure 24 shows the scaling of the factor $\mathcal{N}_{\text{jet}}$ as a function of the viewing angle θ_v. The three plots correspond to three different Γ factors respectively, and for all Γ factors a selection of opening angles $\Delta\theta$ is represented. The values of the opening angles are chosen to be smaller, comparable, and larger than the angle corresponding to the critical angle of $1/\Gamma$. These three cases are illustrated in Fig. 23. The curves are normalized to their on-axis value, which is found to be approximately $4\pi\Gamma^2$. Additionally, the red, dashed curves in the plots indicate how the approach $\mathcal{D}^3(\theta_v)$ (defined in Eq. 4.7) behaves as a function of the viewing angle θ_v. These curves are normalized by the $\mathcal{D}(0) \to 2\Gamma$ approximation. When studying the $\mathcal{N}_{\text{jet}}$ curves, we identify three categories of behaviour depending on the opening angle:

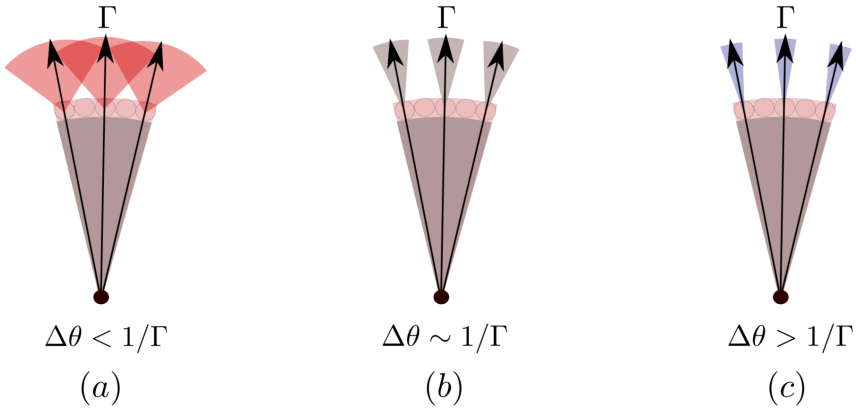

FIG. 23. Illustration for GRB emission jets with different $\Delta\theta$ and Γ values. The illustration assumes the same opening angle in all cases and shows the spread from the emission *blobs* for low Γ values (left), medium Γ values with $\Delta\theta \sim 1/\Gamma$ and high Γ values (right). For viewing angles with $\theta_v \sim \Delta\theta$ we expect different amounts of emissions from the three cases.

- $\Delta\theta \sim 1/\Gamma$ (Fig. 23b): The curve follows approximately the red dashed curve, showing $\mathcal{D}(\theta_v)^3$ behaviour. The largest discrepancy between $\mathcal{D}(\theta_v)^3$ and $\mathcal{N}_{\text{jet}}$ can be identified for viewing angles corresponding roughly to the opening angle and thus to the critical angle $1/\Gamma$. This is the region where an observer is positioned at the "edge" of the GRB emission jet.

- $\Delta\theta < 1/\Gamma$ (Fig. 23a): The curve follows the same trajectory as $\mathcal{D}(\theta_v)^3$, but reaches a smaller on-axis value, which can be approximated as $2(\Gamma\Delta\theta)^2$. For small opening angles we approximate $\mathrm{d}\Omega^*$ as $\pi\Delta\theta^2$ in Eq. 5.10. By doing this, we obtained $\mathcal{N}_{\text{jet}} \to (\pi\Delta\theta^2)\Gamma(2\Gamma)^3$ for the on-axis case with $\mathcal{D} \to 2\Gamma$. Dividing this by the normalization constant $4\pi\Gamma^2$ gives $2(\Gamma\Delta\theta)^2$. Thus, for an on-axis observer, the amount of received emission lowers with decreasing opening angle. From $\Delta\theta \sim 1/\Gamma$ downwards, the on-axis observer will feel a stronger decrease in emission because less infinitesimal emission regions (*blobs*) are included by the integral over $\mathrm{d}\theta$. Looking at the illustration (a) in Fig. 23, is becomes clear, that for small opening angles, less emission from the widely boosted *blobs* is included. The constant region for small viewing angles becomes shorter and the drop occurs at roughly $\theta_v \sim \Delta\theta$. For large viewing angles, the edge becomes dominant and $\mathcal{N}_{\text{jet}}$ behaves like a point-source, $\mathcal{D}(\theta_v)^3$

- $\Delta\theta > 1/\Gamma$ (Fig. 23c): We identify a trajectory that does not coincide with the $\mathcal{D}(\theta_v)^3$ curve at a first glance. The normalized value for $\mathcal{N}_{\text{jet}}$ is independent of θ_v for $\theta_v < \Delta\theta$, which is interpreted such, that emission coming from the jet edge is sub-dominant. The curve falls rapidly at $\theta_v \sim \Delta\theta$. Until $\sim 2\Delta\theta$ the rapid fall continues and behaves asymptotically like a $\mathcal{D}(\theta_v)^3$ behaviour for larger viewing angles outside the jet cone.

The curves of $\mathcal{N}_{\text{jet}}$ shown in Fig. 24 can be summarized as follows: For all Γ values, the factor $\mathcal{N}_{\text{jet}}$ is constant as long as θ_v is smaller than $\Delta\theta$, meaning that the line of sight of the observer coincidences with being "inside" the jet opening angle. Thin jets ($\Delta\theta < 1/\Gamma$)

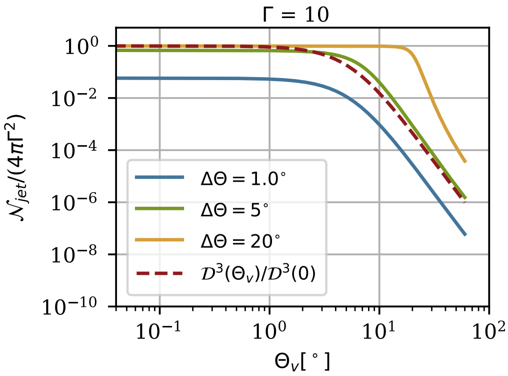

(a) $\Gamma = 10$, $1/\Gamma \sim 5.73°$

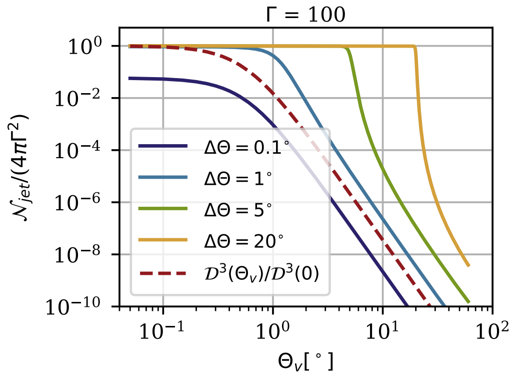

(b) $\Gamma = 100$, $1/\Gamma \sim 0.57°$

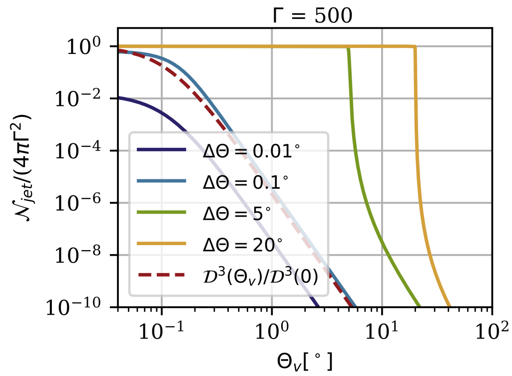

(c) $\Gamma = 500$, $1/\Gamma \sim 0.12°$

FIG. 24. Behaviour of the $\mathcal{N}_{\text{jet}}$ as a function of the viewing angle, θ_v, for different opening angels, $\Delta\theta$, and Γ Lorentz factors. The curves are normalized to $4\pi\Gamma^2$, as this is the expected on-axis value for $\mathcal{N}_{\text{jet}}$. The red dashed curves show how $\mathcal{D}(\theta)^3$ behaves compared to the new factor. Strong deviations above and below the critical opening angle of $1/\Gamma$ are visible.

follow the $\mathcal{D}^3$ curve under consideration of small off-axis values. In all cases, $\mathcal{N}_{\text{jet}}$ behaves like $\mathcal{D}^3$ at large viewing angles ($\Delta\theta \ll \theta_v$). This is interpreted such, that for viewing angles far outside the jet region, the emission from the jet appears point-source like. The edge of the jet becomes dominant for the emission. The transition area, where the viewing angle coincidences roughly with the opening angle has a different, more rapid behaviour in the wide jet case. The higher the Lorentz boost, the sharper becomes the edge at $\theta_v \sim \Delta\theta$. For lower Γ values, a larger opening angle $\Delta\theta$ has to be chosen to observe a sharp edge. Similar results have already been shown in [39]. In this reference, the curves are parametrized piecewise for the three different regimes, which we also identified. Our exact calculation of $\mathcal{N}_{\text{jet}}$ is consistent with [39], which approves our approach.

Figure 25 illustrates, how $\mathcal{N}_{\text{jet}}$ behaves as a function of $\Delta\theta$ for various viewing angles. Similar to the previous plots, the factor is plotted for different viewing angles, which cover the regions above, below and comparable to the critical angle $1/\Gamma$. Again, the plot is represented for three different Γ factors and normalized by $4\pi\Gamma^2$. Following the procedure from above we identify different behaviours in the curves:

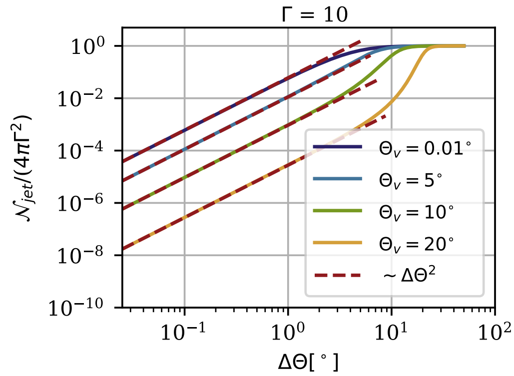

(a) $\Gamma = 10$, $1/\Gamma \sim 5.73°$

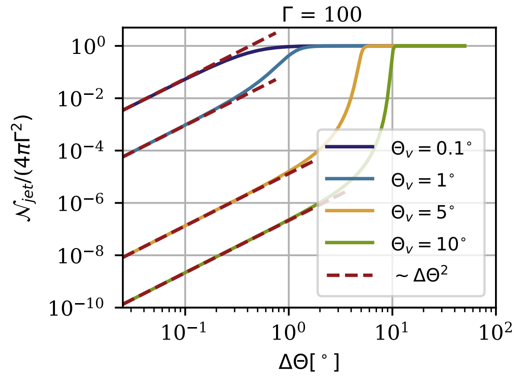

(b) $\Gamma = 100$, $1/\Gamma \sim 0.57°$

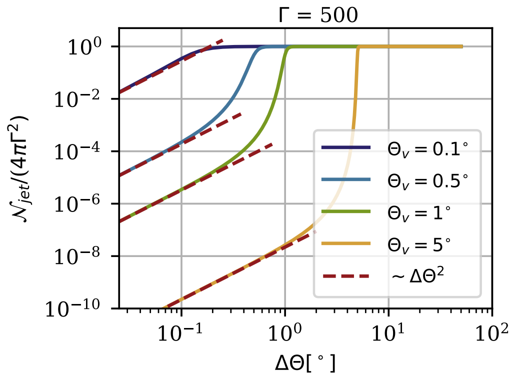

(c) $\Gamma = 500$, $1/\Gamma \sim 0.12°$

FIG. 25. $\mathcal{N}_{\rm jet}$ as a function of $\Delta\theta$. For wide jets compared to the viewing angle, $\Delta\theta \gtrsim \theta_v$, $\mathcal{N}_{\rm jet}$ converges the on-axis value of $4\pi\Gamma^2$. For viewing angles around $1/\Gamma$, the curvature of $\mathcal{N}_{\rm jet}$ changes from being positive to negative.

- $\Delta\theta < 1/\Gamma$: The factor $\mathcal{N}_{\rm jet}$ approaches very low values for small opening angles. The factor becomes smaller for large viewing angles and follows a $\sim \Delta\theta^2$ behaviour to higher opening angles. To understand this, consider the same approximation for Eq. 5.10 for small opening angles we already discussed in the last paragraph, $\mathcal{N}_{\rm jet} \to \Gamma\mathcal{D}^3(\theta_v)\pi(\Delta\theta)^2$. Here, $\mathcal{D}^3(\Omega^*) \to \mathcal{D}^3(\theta_v)$ follows by definition from fixing θ to a constant value of 0 in Eq. 5.8. Naturally, for a vanishing opening angle it follows that $\mathcal{N}_{\rm jet} \to 0$.

- $\Delta\theta \sim 1/\Gamma$: The transition area is characterized by a steep increase of the $\mathcal{N}_{\rm jet}$ factor, which appears to be steeper for larger viewing angles. For $\theta_v > 1/\Gamma$, there is a strong "jump" in the behaviour of the curve. This jump coincides with the jet edge coming into the view. This jump is a smooth transition for smaller viewing angles with $\theta_v < 1/\Gamma$.

- $\Delta\theta > \max[(1/\Gamma), \theta_v]$: $\mathcal{N}_{\rm jet}$ approaches the constant value, which is $4\pi\Gamma^2$ for all viewing angles and Lorentz factors. This confirms nicely, that the commonly known scaling for the internal photon density (Eq. 4.27) can be correctly reproduced for wide opening angles in our convention.

Figures 24 and 25 represent clearly, that the new added consideration of the jet opening angle modifies the behaviour of the Doppler factor $\mathcal{D}$. Assumptions that were made in earlier works are hereby proven to be only correct for the special case of a wide jet.

5.2 PHOTON AND NEUTRINO SPECTRA

In the following, we study the effect of the introduced generalization of the Doppler factor on the photon and thus also the neutrino spectrum. We will see, that the generalization allows an approximation, which makes the description somewhat more intuitive and resists validation tests.

The particle fluence $F(E)$ is generally connected with the energy fluence via $\mathcal{F} = \int EF(E)\mathrm{d}E$. In Eq. 5.4 we integrate the photon spectrum $n'_\gamma(\epsilon')$ over the photon energy $\mathrm{d}\epsilon'$ to obtain the internal energy density U'_γ. Let us go one step back to find the differential photon fluence, which can be written in the form

$$\epsilon^2 F(\epsilon) = \frac{1+z}{4\pi d_L^2} r_{\mathrm{dis}}^2 \Delta r \int\limits_{\Delta\Omega} \mathrm{d}\Omega^* \; \Gamma \; \mathcal{D}^3(\Omega^*) \left[\epsilon'^2 n'_\gamma(\epsilon')\right]_{\epsilon'=\epsilon\frac{1+z}{\mathcal{D}(\Omega^*)}} . \tag{5.14}$$

Again, we identify the norm factor $\mathcal{N}_{\mathrm{jet}}$, which we introduced in the previous chapter. But additionally, the photon energy transforms with the Doppler factor, and thus, also has to be integrated over the polar and azimuthal angle of the jet. More intuitive, this means, that the photon spectrum n'_γ is found to be a superposition of many spectra observed under different observation angles. This corresponds to the same description as already discussed with the help of Fig. 22b. Every *blob* emits a photon spectrum, which is observed under different shifting conditions. The resulting total spectrum observed at Earth is the sum of all these individual spectra. This has a natural consequence: For individual photon spectra approximated as broken power-laws, the break energies are all slightly shifted. Integrating over all spectra leads to a “smoothed” break instead of a sharp break.

In Eq. 5.14, the norm factor $\mathcal{N}_{\mathrm{jet}}$ is not a stand-alone argument anymore, as the integral has to be performed including the photon energy and spectrum. To simplify this expression we define an *effective* Doppler factor $\langle\delta\rangle_{\mathrm{eff}}$ for the energy shift and spectrum as

$$\langle\delta\rangle_{\mathrm{eff}} := \int\limits_{\Delta\Omega_{\mathrm{jet}}} \mathrm{d}\Omega^* \; \Gamma \; \mathcal{D}^3(\Omega^*) \Bigg/ \int\limits_{\Delta\Omega_{\mathrm{jet}}} \mathrm{d}\Omega^* \; \Gamma \; \mathcal{D}^2(\Omega^*) \, . \tag{5.15}$$

Note that this essentially defines an averaged Doppler factor. This definition allows to simplify not only Eq. 5.14, it also is constructed such that the energy and particle fluence at the source are conserved. The nominator in Eq. 5.15 scales with $\mathcal{D}^3(\Omega^*)$

corresponding to Eq. 5.14, which describes the energy. Dividing both sides of the Eq. 5.14 by ϵ corresponds to the number of particles

$$\begin{aligned}\epsilon F(\epsilon) &= \frac{1+z}{4\pi d_L^2} r_{\rm dis}^2 \Delta r \int\limits_{\Delta\Omega} \mathrm{d}\Omega^* \ \Gamma \ \mathcal{D}^3(\Omega^*) \frac{1}{\epsilon} \left[\epsilon'^2 n'_\gamma(\epsilon')\right]_{\epsilon'=\epsilon\frac{1+z}{\mathcal{D}(\Omega^*)}} \\ &= \frac{(1+z)^2}{4\pi d_L^2} r_{\rm dis}^2 \Delta r \int\limits_{\Delta\Omega} \mathrm{d}\Omega^* \ \Gamma \ \mathcal{D}^2(\Omega^*) \left[\epsilon' n'_\gamma(\epsilon')\right]_{\epsilon'=\epsilon\frac{1+z}{\mathcal{D}(\Omega^*)}} \ , \end{aligned} \tag{5.16}$$

where in the last step, $1/\epsilon$ is replaced by $(1+z)/(\mathcal{D}(\Omega^*)\epsilon')$ and therefore,the number of particles, Eq. 5.16, scales with $\mathcal{D}^2(\Omega^*)$. This is per construction used as denominator in the definition of $\langle\delta\rangle_{\rm eff}$ in Eq. 5.15 and the averaged Doppler-factor is weighted by this expression. We will see in the following, that the definition of $\langle\delta\rangle_{\rm eff}$ has another handy advantage. This is given by the fact that $\langle\delta\rangle_{\rm eff}$ approaches Γ for specific on-axis cases, which was found to be a widely used scaling factor for considerations without opening angles. Thus, our chosen definition of $\langle\delta\rangle_{\rm eff}$ is capable to reproduce well established results.

Using the averaged Doppler factor in Eq. 5.15 and assuming that variations in $n'(\epsilon')$ across the jet are negligible, allows to approximate Eq. 5.14 as

$$\epsilon^2 F(\epsilon) \simeq \frac{1+z}{4\pi d_L^2} r_{\rm dis}^2 \Delta r \mathcal{N}_{\rm jet} \left[\epsilon'^2 n'(\epsilon')\right]_{\epsilon'=\epsilon\frac{1+z}{\langle\delta\rangle_{\rm eff}}} \ . \tag{5.17}$$

The result given in Eq. 5.17 is worth studying in detail. Consider the flux for an on- and off-axis emission respectively, where we divide both sides of Eq. 5.17 by ϵ^2 and use $\epsilon'/\epsilon = (1+z)/\langle\delta\rangle_{\rm eff}$

$$F^{\rm on}(\epsilon) \simeq \frac{1+z}{4\pi d_L^2} r_{\rm dis}^2 \Delta r \mathcal{N}_{\rm jet}^{\rm on} \left(\frac{(1+z)}{\langle\delta\rangle_{\rm eff}^{\rm on}}\right)^2 \left[n'(\epsilon')\right]_{\epsilon'=\epsilon\frac{1+z}{\langle\delta\rangle_{\rm eff}^{\rm on}}} \ , \tag{5.18}$$

$$F^{\rm off}(\epsilon) \simeq \frac{1+z}{4\pi d_L^2} r_{\rm dis}^2 \Delta r \mathcal{N}_{\rm jet}^{\rm off} \left(\frac{(1+z)}{\langle\delta\rangle_{\rm eff}^{\rm off}}\right)^2 \left[n'(\epsilon')\right]_{\epsilon'=\epsilon\frac{1+z}{\langle\delta\rangle_{\rm eff}^{\rm off}}} \ . \tag{5.19}$$

As already mentioned, we assume that the internal spectrum behaves almost constant across the neutrino emission region. Therefore, we can solve Eq. 5.18 for the pre-factor times $n'(\epsilon')$ and write it into Eq. 5.19. By this we find

$$F_{\rm off}(\epsilon) \simeq \frac{\mathcal{N}_{\rm jet}^{\rm off}}{\mathcal{N}_{\rm jet}^{\rm on}} \frac{1}{\eta^2} F_{\rm on}(\epsilon/\eta) \,, \tag{5.20}$$

where $\eta = \langle\delta\rangle_{\rm eff}^{\rm off}/\langle\delta\rangle_{\rm eff}^{\rm on}$. This results enables us to predict off-axis emission based on on-axis calculations. This is of great importance, because most neutrino predictions are based on on-axis emission. Equation 5.20 gives an easy access to scale down these predictions. Furthermore, it can be simplified to what is in the following called the *naive* off-axis scaling ("naive" in the sense of simplified, meaning it is valid for one special case compared to our derived generalization), defined as [16]

$$F_{\rm off}(\epsilon) = \eta' F_{\rm on}(\epsilon/\eta') \,, \tag{5.21}$$

with $\eta' = \mathcal{D}(\theta_v)/\mathcal{D}(0) \simeq 2\Gamma/\Gamma(1-\beta\cos(\theta_v))$. This can be derived from the more general scaling in Eq. 5.20: for $\langle\delta\rangle \to \mathcal{D}$ we find that $\eta = \eta'$. Furthermore, in Fig. 24 it was

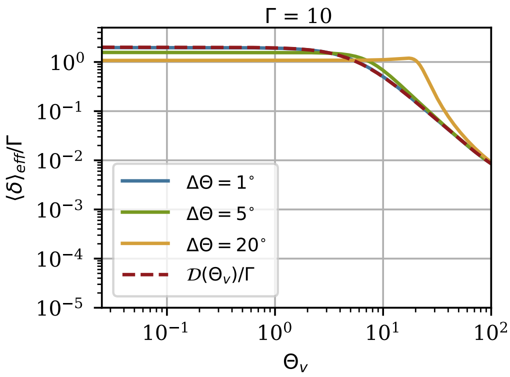

(a) $\Gamma = 10$

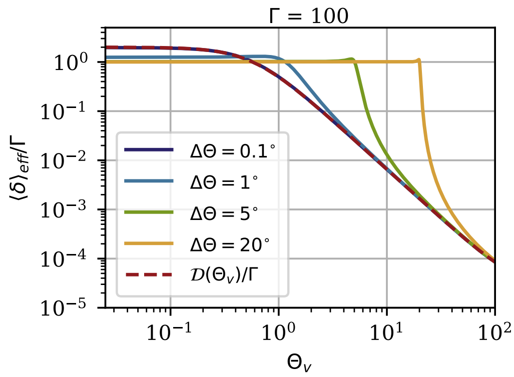

(b) $\Gamma = 100$

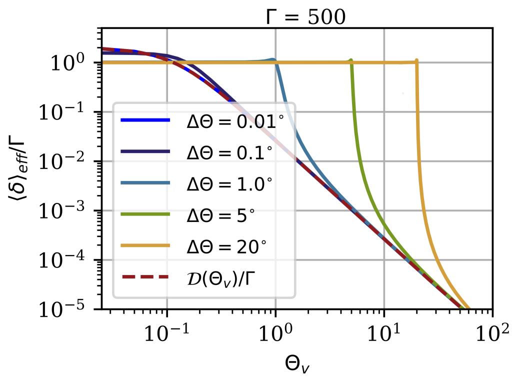

(c) $\Gamma = 500$

FIG. 26. Effective Doppler factor $\langle\delta\rangle_{\text{eff}}$ as a function of θ_v. All curves are normalized to Γ. Shown are not only $\langle\delta\rangle_{\text{eff}}$ for different opening angles and Γ factors, but also $\mathcal{D}(\theta)$, normalized to Γ, as a comparison (red dashed curve).

found that $\mathcal{N}_{\text{jet}}^{\text{off}}$ behaves like $\mathcal{D}^3(\theta_v)/\mathcal{D}^3(0) = \eta'^3$ for narrow jets. With $\mathcal{N}_{\text{jet}}^{\text{on}} = 1$ in this approximation, one arrives at Eq. 5.21, which is an approximation for narrow jets. The more general scaling is nevertheless given in Eq. 5.20.

Following the investigations we made for the jet norm factor $\mathcal{N}_{\text{jet}}$ in section 5.1, we study $\langle\delta\rangle_{\text{eff}}$ as a function of the viewing angle θ_v (Fig. 26) and opening angle $\Delta\theta$ (Fig. 27). Figure 26 shows for three Γ factors the behaviour of $\langle\delta\rangle_{\text{eff}}$ as a function of θ_v, dependent on different jet opening angles. The curves are normalized to Γ and similar to the plots for $\mathcal{N}_{\text{jet}}$, we show as a reference the behaviour of $\mathcal{D}(\theta_v)$, which in this case is normalized by Γ. We conclude from investigating Fig. 26:

- $\Delta\theta < 1/\Gamma$: The averaged Doppler factor $\langle\delta\rangle_{\text{eff}}$ follows closely the $\mathcal{D}(\theta_v)$ curve. For on-axis observations with $\theta_v = 0^\circ$ we find $\langle\delta\rangle_{\text{eff}}$ to be 2Γ, which agrees with the $\mathcal{D}(0) \to 2\Gamma$ approximation for the Doppler factor (Eq. 4.8)

- $\Delta\theta > 1/\Gamma$: For *fat* jets with $\Delta\theta_v > 1/\Gamma$, the curves approach an on-axis case which corresponds roughly to Γ. The larger the opening angle, the closer the on-axis value goes to Γ, which corresponds to the widely used factor. Thus, we are capable to reproduce well established results as a limiting case of our approximation for a

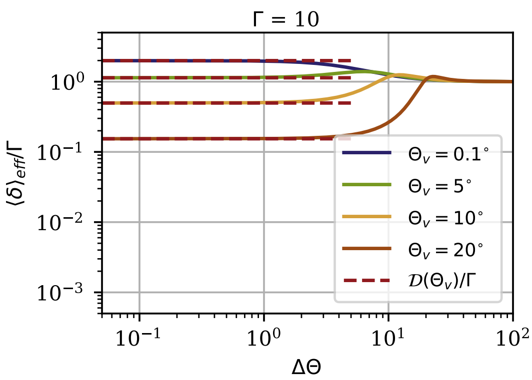

(a) $\Gamma = 10$

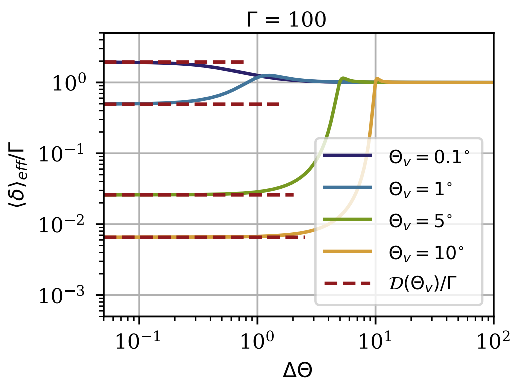

(b) $\Gamma = 100$

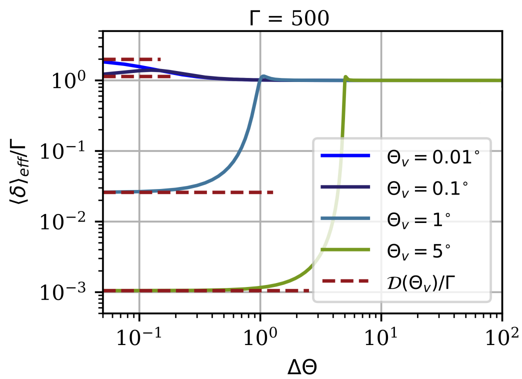

(c) $\Gamma = 500$

FIG. 27. Effective Doppler factor $\langle\delta\rangle_{\text{eff}}$ as a function of $\Delta\theta$. The curves are all normalized to Γ. The red, dashed curves indicate that for small opening angles the effective Doppler factor behaves like to "naive" Doppler factor $\mathcal{D}(\theta_v)$, which is here normalized to Γ.

fat jet with wide opening angle. For increasing viewing angles, $\langle\delta\rangle_{\text{eff}}$ is constant at its on-axis value until $\theta_v \sim \Delta\theta$. At this point, the curve for $\langle\delta\rangle_{\text{eff}}$ rises slightly before rapidly falling and converging the $\mathcal{D}(\theta_v)$ behaviour. The rise for $\langle\delta\rangle_{\text{eff}}$ is at a viewing angle that coincides exactly with an observer positioned at the edge of the jet as a consequence of the interfering Doppler factors.

Figure27 shows $\langle\delta\rangle_{\text{eff}}$ as a function of $\Delta\theta$, normalized by Γ. Once again, three plots represent 3 different Γ factors. On each plot $\langle\delta\rangle_{\text{eff}}$ is depicted for different viewing angles, which are selected to illustrate different behaviours whether the viewing angle coincidences with being smaller, comparable or larger than the critical angle $1/\Gamma$. For all curves individually, the corresponding value of the naive $\mathcal{D}(\theta_v)$ is drawn as a red, dashed line. We distinguish:

- $\theta_v < 1/\Gamma$: For small opening angles, $\langle\delta\rangle_{\text{eff}}$ approaches 2Γ. After a constant range the curve falls down and converges to Γ. For viewing angles very close to $1/\Gamma$, the curve is constant for almost the entire $\Delta\theta$ range, except a minimal increase for $\Delta\theta = \theta_v$. This marks again the case where the line of sight of the observer is equivalent with the edge of the jet. The $\langle\delta\rangle_{\text{eff}}$ values for small opening angles can be understood with the same argument as stated for the $\mathcal{N}_{\mathrm{jet}}$ consideration. For small angles, we find $\mathrm{d}\Omega^* \to \pi\Delta\theta^2$ and $\mathcal{D}(\Omega^*) \to \mathcal{D}(\theta_v)$. Due to the definition of $\langle\delta\rangle_{\mathrm{eff}}$ the $\pi\Delta\theta^2$ dependencies get cancelled, while $\mathcal{D}^3(\Omega^*)/\mathcal{D}^2(\Omega^*) = \mathcal{D}(\theta_v)$, which explains the red dashed curves.

- $\theta_v > 1/\Gamma$: The effective Doppler factor $\langle\delta\rangle_{\mathrm{eff}}$ is constant for small opening angles at a low value, which is lower the higher the off-axis angle is for the same reason we just explained ($\mathcal{D}(\theta_v)$). The curve increases rapidly and overshoots Γ with a peak at $\Delta\theta \sim \theta_v$. From this point, it converges towards Γ. These small peaks above Γ for large viewing angles occur for the same reasons as already discussed in Fig. 27: It is the critical region where the viewing angle and the opening angle become equal, by means the observer is aligned with the edge of the jet. This has an increased *effective* Doppler factor as a consequence.

The main insights we obtained from investigating the behaviour of $\mathcal{N}_{\mathrm{jet}}$ and $\langle\delta\rangle_{\mathrm{eff}}$ can be summarized as

1. Including a finite opening angle of the emission jet in the theoretical description changes established results that were used in studies, such as [16, 21, 38, 46, 64].

2. This well known and theoretically established scaling of the internal energy density and thus the neutrino spectrum, is valid for considerations of jets with wide opening angles.

3. The on-axis approximation $\mathcal{D} \to 2\Gamma$ is only valid for thin jets with $\Delta\theta < 1/\Gamma$.

5.2.1 *Validation of the Effective Doppler Factor* $\langle\delta\rangle_{\mathrm{eff}}$

Before we continue to apply the new formalism on actually neutrino spectra, we take a moment to discuss the validity of the introduced approximation with $\langle\delta\rangle_{\mathrm{eff}}$ in Eq. 5.17. In the following, we compare two different approaches to express the shift in the photon spectrum. We investigate the difference between the exact method with $\mathcal{D}(\Omega^*)$, as stated in Eq. 5.14 and the approximation via $\langle\delta\rangle_{\mathrm{eff}}$, given in Eq. 5.17. The exact strategy will be denoted *exact*, while *effective* refers to the approximation. We already discussed, that the integration over multiple photon spectra will lead to a smoothed final spectrum observed at Earth. To see this effect we use a broken power-law with two breaks as a simplified test spectrum:

$$n'(\epsilon') = \begin{cases} (\epsilon'/\epsilon_{\mathrm{br},1})^{-\alpha} & \epsilon' < \epsilon_{\mathrm{br},1} \\ (\epsilon'/\epsilon_{\mathrm{br},1})^{-\beta} & \epsilon' \in [\epsilon_{\mathrm{br},1}, \epsilon_{\mathrm{br},2}] \\ (\epsilon'/\epsilon_{\mathrm{br},2})^{-\gamma} & \epsilon' > \epsilon_{\mathrm{br},2}\,. \end{cases} \tag{5.22}$$

We use this definition for the spectrum in Eqs. 5.14 and 5.17. The results for one exemplary case with Γ=100 and arbitrary choices of $\epsilon_{\mathrm{br},1} = 1$ eV, $\epsilon_{\mathrm{br},2} = 10$ eV, $\alpha = 1.0, \beta = 2.0, \gamma = 4.0$ for two different viewing angles $\theta_v = 1°, 5°$ and two opening angles $\Delta\theta = 3°, 5°$ are represented in Fig. 28

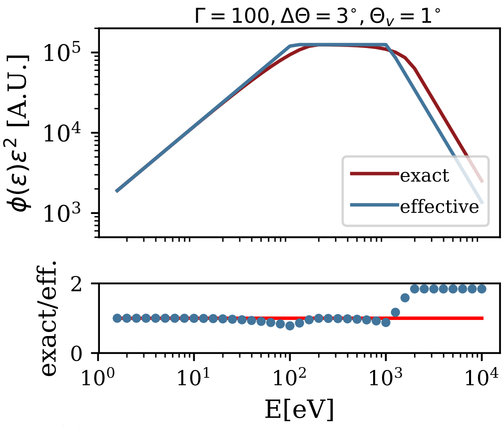

(a) $\Gamma = 100$, $\theta_v = 1.0°$, $\Delta\theta = 3.0°$

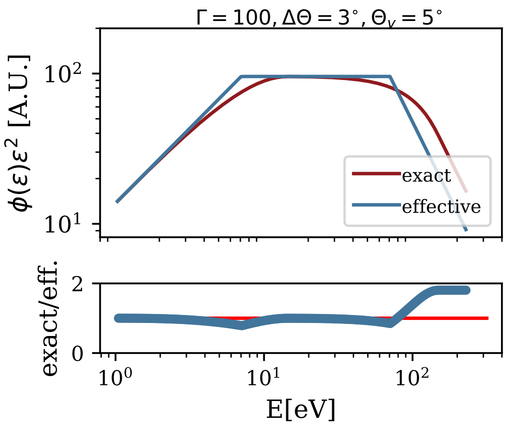

(b) $\Gamma = 100$, $\theta_v = 5.0°$, $\Delta\theta = 3.0°$

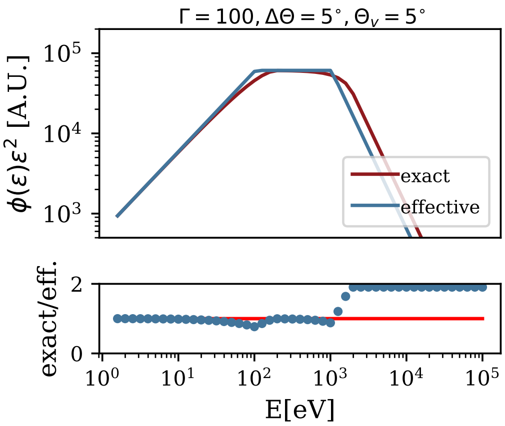

(c) $\Gamma = 100$, $\theta_v = 5.0°$, $\Delta\theta = 5.0°$

FIG. 28. Comparison between the exact (red) and effective (blue) approximation of the energy shift in the spectrum. The lower plots in (a), (b) and (c) show the deviation between the two methods: around the break energies and the falling side of the spectra, we find the largest discrepancy. Note the remarkable difference in the orders of magnitude on the y-axis, due to the variation of opening and viewing angles.

The three plots show for two different jet opening angles and viewing angles how the observed photon spectra look like according to the two approaches of Doppler shift, the exact and the effective. The two approaches are drawn in different colors and their deviation from each other is shown in the lower plots, respectively. Before going into the details of the comparison we would like to record, that the broken power-law spectrum of the spectrum shows indeed a softened break, as we mentioned already. Figure 12 in section 3.4 shows one individual spectrum with a sharp cutoff at the peak energy. For the exact treatment (red curves) in Fig. 28, we now observe a superposition of many broken power laws, which, summed up by the integral, show a smooth transition around the regions, where the spectral indices change. As the approximation follows closely the exact determination, we use the effective Doppler factor in the following.

The spectra we showed in Fig. 21 are for an on-axis observation. In this section, we show, that based on such on-axis predictions, it is possible to infer a "naive" off-axis scaling. Such a procedure was done in [16] to estimate the expected neutrino flux from a potential off-axis emission. We call these predictions "naive" because no assumptions about an opening angle are made. In fact, the emission is assumed to come from one emission blob, and thus no integration/averaging is applied. This can be interpreted as a very narrow jet. Only the final on-axis neutrino spectrum will be multiplied by a scaling factor η to account for a decreasing spectrum with increasing viewing angle, which was already derived in section 5.2. We do not change the values of the internal GRB parameters, even though they should change with the viewing-angle dependent Doppler factors. For the same observed fluence from different viewing angles, one should obtain larger internal GRB parameters, as the fluence would experience a larger boost for greater viewing angles.

Using Eq. 5.21 from section 5.2, we scale down the predicted on-axis neutrino spectrum and account for a shift in energy with η' with $E^{\text{off}} = \eta'/E^{\text{on}}$. The plots on the LHS of Fig. 29 show the effect of this scaling on the three different GRB models.

The horizontal shift of the spectrum towards smaller energies for higher viewing angles is due to the scaling of the internal spectrum itself. Additionally the spectrum is shifted vertically by η'^3, due to the shift in the fluence and energy. Larger off-axis emission means a smaller value for $\mathcal{D}$ and thus the boost into the GRB frame is lower. This affects the internal GRB quantities such as e.g. the photon energy density, which eventually determine the neutrino production. Furthermore, we observe that for large Γ factors, the effect of an off-axis observation leads to a stronger suppression of the neutrino spectrum. We will come back to this phenomena later on again and explain this in detail. We have seen previously, that the Doppler boost is very different when we properly include an off-axis and additionally an opening angle in the description. The curves in Fig. 29 in the left column serve as a first idea of how off-axis emission affects the observed spectra. We will come back to these plots once we obtained the scaling with the generalized description and compare the two different approaches.

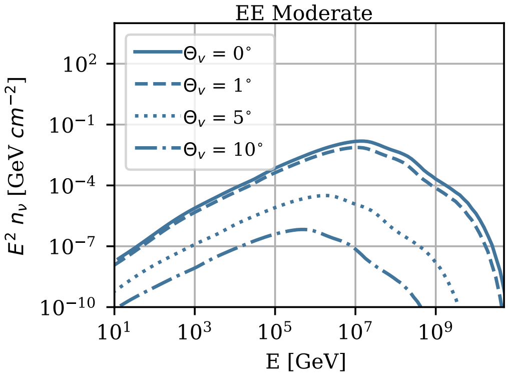

(a) $\Gamma = 30$, simplified scaling

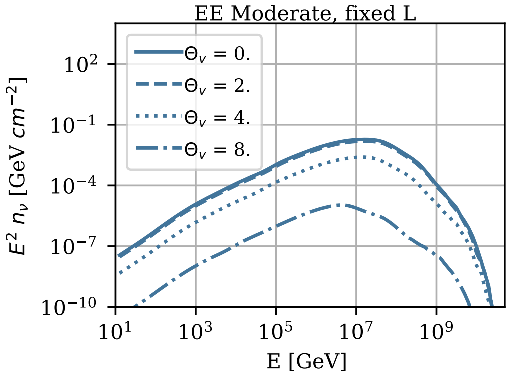

(b) $\Gamma = 30$, sophisticated scaling

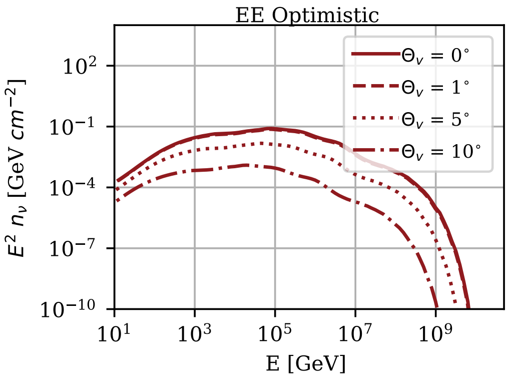

(c) $\Gamma = 10$, simplified scaling

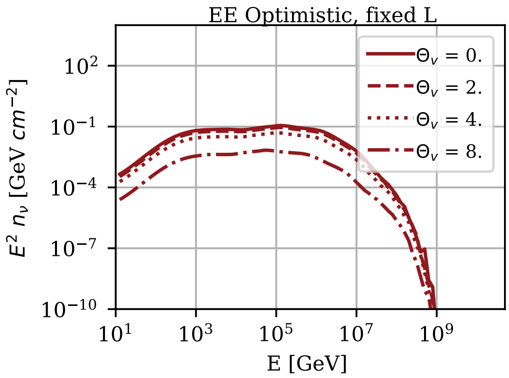

(d) $\Gamma = 10$, sophisticated scaling

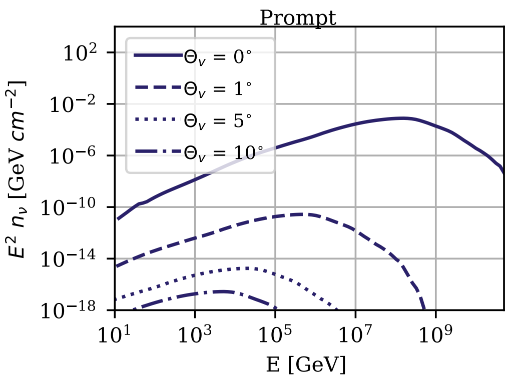

(e) $\Gamma = 1000$, simplified scaling

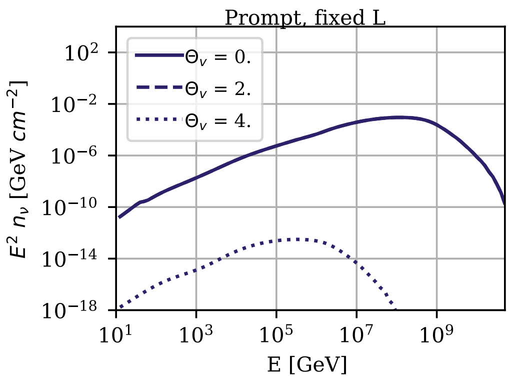

(f) $\Gamma = 1000$, sophisticated scaling

FIG. 29. On-axis (solid lines) neutrino spectra and off-axis scaling achieved with the scaling factor η' (plots in the left column) and generalized scaling with $\mathcal{N}_{\rm jet}$ and $\langle\delta\rangle_{\rm eff}$ (plots in the right column). Note the adjusted y-axis range for the prompt emission case.

	$\mathcal{N}_{\text{jet}}(\theta_v)$				$\langle\delta\rangle_{\text{eff}}(\theta_v)$			
Model	0°	2°	4°	8°	0°	2°	4°	8°
EE Mod.	10367.6	8406.1	1481.67	15.68	38.65	39.92	24.60	4.47
EE Opt.	480.02	393.54	218.20	33.70	17.82	16.94	14.30	7.75
Prompt	1.26e07	1.26e07	20.70	0.02	1000.36	1001.18	2.74	0.15

TAB. 2. Values for $\langle\delta\rangle_{\text{eff}}$ and $\mathcal{N}_{\text{jet}}$ with varying viewing angle θ_v. The opening angle is kept fix at $\Delta\theta = 3°$ and the Lorentz factors are 30 for EE Moderate, 10 for the EE Optimistic, and 1000 for the Prompt emission models. These values are used in the modified FIREBALLET program.

5.4 SOPHISTICATED OFF-AXIS SCALING

The IceCube software FIREBALLET, which we introduced in section 4.3, is extremely useful when it comes to the predictions of neutrino fluxes generated in GRB environments. So far, there is no option to give reasonable estimations for off-axis emission. This means, that the Doppler factor $\mathcal{D}$ is approximated by the Lorentz factor Γ. But as we showed in the last section, this can only be used for a wide jet, on-axis approximation. In this section, we modify FIREBALLET to become a tool for realistic descriptions for off-axis emission GRBs with $\mathcal{N}_{\text{jet}}$ and δ_{eff} as we defined them in Eq. 5.10 and Eq. 5.15 and study the results from this modification.

5.4.1 *Implementation*

Following Eqs. 5.15 and 5.10, we introduce two new factors as input parameters in FIREBALLET. While $\langle\delta\rangle_{\text{eff}}$ replaces Γ for all shifts in energy, $\mathcal{N}_{\text{jet}}$ substitutes $4\pi\Gamma^2$ in the calculation of U'_γ and the B-field calculation based on U'_γ, as shown in Eq. 5.13. The Lorentz factor Γ is kept for the calculation of the dissipations radius r_{dis} and the variability time scale t_{dyn} as defined in Eq.4.24 in section 4.2. The values for $\langle\delta\rangle_{\text{eff}}$ and $\mathcal{N}_{\text{jet}}$ have to be calculated externally for given sets of Lorentz boost Γ, opening angle $\Delta\theta$ and viewing angle θ_v. The software is (yet) not capable to calculate $\langle\delta\rangle_{\text{eff}}$ and $\mathcal{N}_{\text{jet}}$ from given input values Γ, $\Delta\theta$ and θ_v.

In the following, we discuss the resulting off-axis spectra for the three GRB models we introduced in section 4.3.2. We only adopt one fixed opening angle, $\Delta\theta = 3°$ and vary the viewing angle within a range of four angles, $0°, 2°, 4°, 8°$. By this, we make sure to cover ranges for viewing angles within and outside the jet opening angle. The calculated values for $\langle\delta\rangle_{\text{eff}}$ and $\mathcal{N}_{\text{jet}}$ are listed in Tab. 2.

5.4.2 *Validation*

As a sanity check, we use values for $\mathcal{N}_{\text{jet}}$ and $\langle\delta\rangle_{\text{eff}}$ corresponding to values of $4\pi\Gamma^2$ and Γ for the three GRB models. In section 5.1, we found that these values are describing the

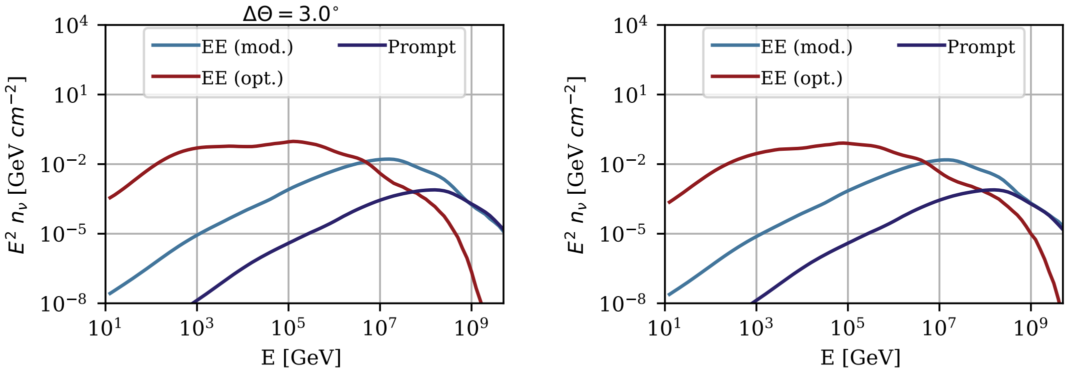

(a) $\mathcal{N}_{\rm jet}$ and $\langle\delta\rangle_{\rm eff}$ for $\Delta\theta = 3^\circ$ and $\theta_v = 0^\circ$. (b) $\mathcal{N}_{\rm jet} = 4\pi\Gamma^2$ and $\langle\delta\rangle_{\rm eff} = \Gamma$, for on-axis emission.

FIG. 30. Neutrino spectra for moderate, optimistic and prompt emission with defined opening angle of $\Delta\theta = 3.0^\circ$ (left) and spectra without defined opening angle (right).

case without a finite opening angle (corresponding to the wide-jet approximation) and on-axis emission. For these input parameters we obtained the on-axis curves shown in Fig. 30b. We do not show the plot here, but the initial FIREBALLET configuration (without $\mathcal{N}_{\rm jet}$ and $\langle\delta\rangle_{\rm eff}$) gives the exact same curves and therefore, we refrain from showing the corresponding plot. However, mentioning this is of great importance, as it allows us to conclude, that we implemented $\mathcal{N}_{\rm jet}$ and $\langle\delta\rangle_{\rm eff}$ correctly. In the following, we use the modified FIREBALLET to calculate neutrino spectra for arbitrary opening and viewing angles.

To see the effect of an opening angle, that is small enough to not fulfil $\mathcal{N}_{\rm jet} \to 4\pi\Gamma^2$ and $\langle\delta\rangle_{\rm eff} \to \Gamma$, we compare the wide angle approximation with results where $\mathcal{N}_{\rm jet}$ and $\langle\delta\rangle_{\rm eff}$ are calculated for $\Delta\theta = 3.0^\circ$ and $\theta_v = 0^\circ$. The values for the two factors are given in Tab. 2. The result is presented in Fig. 30a.

At a first glance, we do not see big differences between the two cases, corresponding to $\Delta\theta = 3^\circ$(left) and the wide-jet approach (right). Especially for the curves corresponding to large Γ factors, which are the prompt ($\Gamma = 1000$) and the EE moderate (Γ=30) emission models, no strong deviation is visible. But for the optimistic model (Γ=10), some deviations are to report, especially in the tail at higher energies. For a Lorentz boost of $\Gamma = 10$, the critical angle corresponds to $1/\Gamma$=5.72°, which is greater than the opening angle of 3°. Therefore, an opening angle of 3° can not be used to approximate the wide-jet approximation for Γ=10, as done in Fig. 30b. Consequently, we expect changes for an included opening angle only for low Lorentz factors with $1/\Gamma > \Delta\theta$. The curves in Fig. 30a match these expectations well.

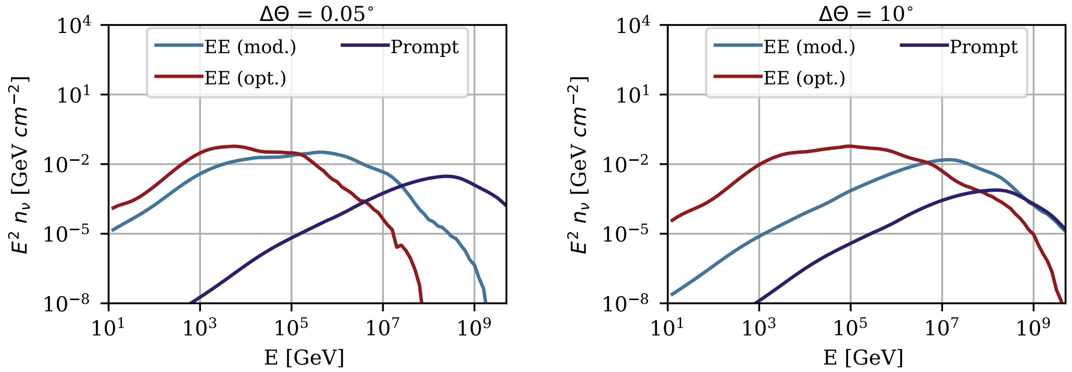

(a) $\Delta\theta > 1/\Gamma$ for all three GRB models.

(b) $\Delta\theta < 1/\Gamma$ for all three GRB models.

FIG. 31. GRB neutrino spectra for on-axis observation, under consideration of different opening angles.

5.4.3 *Variation of Opening Angles*

To understand the arguments we just discussed from a physics point of view, we remind ourselves, that for $\Gamma > 1$ factors, each emitting *blob* along the top-hat of the jet emits predominantly in the forward/boost direction. The emission spread is described by the kinematic angle of $1/\Gamma$. For cases, where $1/\Gamma$ is larger than the geometric opening angle of the jet itself, we "suppress" the emission from individual blobs, as illustrated in Fig. 23 (a). As we integrate only over the range of the jet opening angle, some contributions at wider angles from the blobs will be taken away and thus, the spectrum is affected as seen in Fig. 30a.

The largest Lorentz boost we are considering here is $\Gamma = 1000$, corresponding to a critical angle of 0.06°. We expect, that for an opening angle smaller than 0.06° we observe significant deviations in the spectra for all three models. For this reason, an opening angle of 0.05° is chosen, and the result is presented in Fig. 31a. As predicted, we see changes in all three spectra compared to Fig 30b. From our arguments follows, that the Γ=10 model (EE optimistic) should experience the strongest change, which agrees nicely with Fig. 31a.

Furthermore, we can also investigate how the spectra look for a wide jet with an explicit given opening angle. Following the approach for the narrow jet, we find the largest critical angle for $\Gamma = 10$ to be 5.72°. Choosing an opening angle of $\Delta\theta = 10°$ ensures, that the critical angles for all three models falls within this range. The result is shown in Fig. 31b. Comparing this result with the curves shown in Fig. 30b shows perfect agreement. Thus, even an opening angle of $\Delta\theta = 10°$ is a good wide-jet approximation for the three models we choose. We go back to the behaviour of $\mathcal{N}_{\text{jet}}$ and $\langle\delta\rangle_{\text{eff}}$ as functions of $\Delta\theta$ in Fig. 25 and Fig. 27. In these illustrations we notice, that for opening angles slightly larger than $\Delta\theta$ and small viewing angles, the factors approach their wide-jet approximation values quickly. Thus, an opening angle of 10° is considered to be large for the Lorentz factors we study.

	$2°(0°)$	$4°(1°)$	$8°(5°)$
$\eta'(\theta_{\mathrm{eff}})$	1	0.97	0.57
$(\mathcal{N}_{\mathrm{jet}}^{\mathrm{off}}/\mathcal{N}_{\mathrm{jet}}^{\mathrm{on}})/\eta^2(\theta_v)$	0.91	0.71	0.37

TAB. 3. Scaling values for the Γ=10 optimistic GRB emission model. The viewing angle in brackets is the effective viewing angle $\theta_{\mathrm{eff}} = \max(0, \Delta\theta - \theta_v)$, used for the naive scaling to compare the two cases accordingly.

The GRB 170817A/GW170817 event, which was recently observed in terms of γ -rays and gravitational waves, was found to be a GRB with a narrow jet opening angle of $\Delta\theta \lesssim 5°$. Therefore, we use one fixed, exemplary opening angle of $\Delta\theta = 3.0°$ in the following considerations. The importance of this specific GRB will be further discussed in section 5.5. So far, we only studied the effect of a finite opening angle on on-axis predictions. In the next chapter, we will investigate how the spectra are affected when additionally off-axis viewing angles are considered.

5.4.4 *Off-Axis Scaling including Opening Angles*

For the three GRB models, we would like to study off-axis emission by changing the input parameters of $\mathcal{N}_{\mathrm{jet}}$ and $\langle\delta\rangle_{\mathrm{eff}}$ in Eqs. 5.10 and 5.15 according to arbitrary values of Γ, θ_v and $\Delta\theta$.

For all three GRB models, we calculate the on-axis spectrum and its off-axis equivalents using the values for the factors $\mathcal{N}_{\mathrm{jet}}$ and $\langle\delta\rangle_{\mathrm{eff}}$ given in Tab. 2. To obtain results that are comparable with the ones presented in Fig. 29, we use the "fixed Luminosity" option in Fireballet. This option allows to calculate the neutrino spectra for arbitrary viewing angles, while the isotropic luminosity is kept at a constant value. This corresponds to the case that we observe the same source from different viewing angles, for which we expect a decreasing flux for larger off-axis angles. The results are presented in the right column in Fig. 29. These results can directly be used to compare with the off-axis scaling we obtained for the simplified ("naive") approach, shown in the plots on the left in Fig. 29. For completeness, the results for the off-axis scaling where the fluence instead of the luminosity kept fix are presented in appendix b).

Note, that a viewing angle of e.g. 5° does not describe the same viewing angle for the "naive" and "sophisticated" scaling. In fact, a viewing angle of 5° in the naive scaling corresponds to 5°+$\Delta\theta$ in the "exact" off-axis predictions, because strictly spoken the viewing angle has to be measured from the edge of the jet. This means, that viewing angles of $\theta_v = 2°, 4°, 8°$ in right-hand sided plot in Fig. 29 correspond effectively to viewing angles of $\theta = 0°, 1°, 5°$ in the left-hand sided plots in Fig. 29.

Looking at the results of the two approaches, we conclude, that the naive scaling shows a less strong suppression compared to the sophisticated scaling. This tells us, that off-axis predictions based on the commonly used simplified scaling are generally overestimating the neutrino spectra. The difference in suppression for the different viewing angles can be reproduced and understood by comparing the scaling factors we derived for the relations

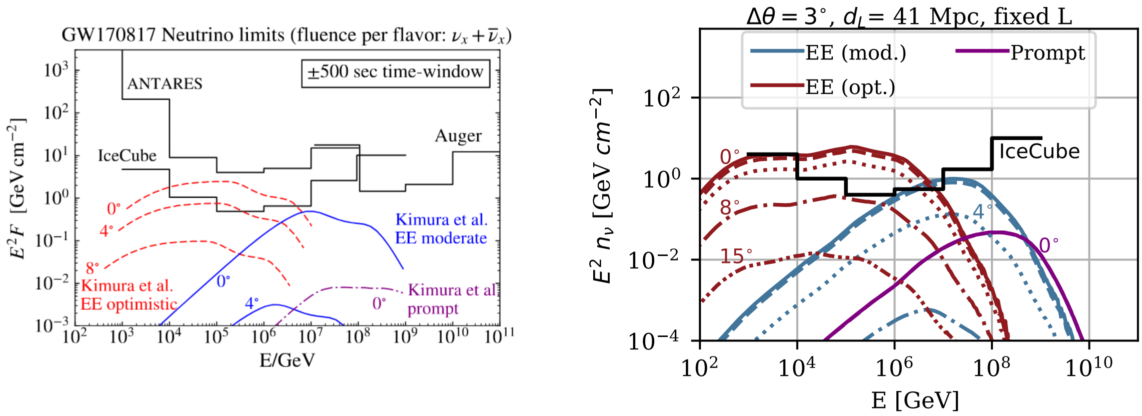

FIG. 32. GW170817 from paper (left) and me (right). Neutrino prediction based on naive off-axis scaling for GW170817/GRB 170817A [16].Neutrino prediction for GW170817/GRB 170817A with consideration of a jet opening angle of $\Delta\theta = 3.0$.

between F_{on} and F_{off} for the two different approaches, done in Eq. 5.21 and Eq. 5.20. The values for the scaling factors are summarized exemplary for the Γ=10 case in Tab. 3. It becomes clear, that the sophisticated scaling experiences a stronger suppression when comparing the scaling factor values for $\theta_v + \Delta\theta$ in the generalized approach with the factors for θ_v in the simplified scaling approach.

5.5 NEUTRINO PREDICTIONS FOR GW170817/GRB 170817 A

In 2017, the gravitational wave signal GW170817 caused great sensation due to the first successful coincident GW and γ-ray observation (GRB 170817A). The event was found to be caused by a NS-NS merger, and therefore expected to produce neutrinos, as we discussed in section 3. Alerts were sent to IceCube and off-line analyses were looking for neutrinos coming from the GRB event.

No neutrinos coincidental with the GW170817/GRB 170817A event were found. Many analyses tried to explain why the GRB was not detected in terms of neutrinos. The argument that was eventually found is that the flux of neutrinos was too low to be detected due to off-axis emission. From the spin-axis of the BH, that was created in the cataclysmic event, an emission angle of $\theta_v = 15°$ was identified [56]. In [16], the naive off-axis scaling was applied to compare the predicted flux with IceCube's sensitivity levels for a ν_μ detection. By this, it became clear that IceCube was not sensitive even for slight off-axis angles. Now, we want to show how these predictions would look like under consideration of the modification regarding the Doppler factor we derived and motivated throughout this thesis.

We follow the approach in [16] to scale down the distance for the Kimura GRB models from 300 Mpc to 41 Mpc, as this was the distance found to correspond to GW170817/GRB 170817A. Again, we keep the observed luminosity fixed and vary the parameters for $\mathcal{N}_{\text{jet}}$

and $\langle\delta\rangle_{\text{eff}}$ according to the studied viewing angles. All parameters from Tab. 1 are used again, except the distance, redshift and luminosity (thus fluence), which are scaled according to the distance difference.

Figure 32 shows the result that was published in [16] (left). We compare this result with the one we obtain for our model, which is presented in Fig. 32 (right). Here, we can once again summarize the features of the generalized off-axis scaling: The overall neutrino flux appears to be a bit higher, when including a finite opening angle of $\Delta\theta = 3.0°$. Note, that in this case we show exactly the same viewing angles in our approach as shown in Fig. 32 (left). Thus, for a consideration of the viewing angle measure from the edge of the jet, one has to subtract the opening angle from the given angles to obtain a 'èffective" viewing angle $\theta_v^{\text{eff}} = \theta_v - \Delta\theta_v$. The curves in Fig. 32 (right) are shown for absolute viewing angle, rather than effective viewing angle, to highlight the effect of an finite opening angle of $\Delta\theta = 3°$. However, the $\theta_v = 4°$ case in Fig. 32 (left) corresponds roughly to $\theta_v = 8°$ in Fig. 32 (right). From this we deduce, that the naive scaling overestimates the neutrino flux and leads to a lighter suppression for large viewing angles, for viewing angles measure from the edge of the jet.

With Fig. 32 (right) we realize, that if GW170817/GRB170817A would have correspond to a GRB with optimistic parameters and at a 15° viewing angle, IceCube's sensitivity would have been only two orders of magnitude away from a detection. On the other hand, the suppression for small viewing angles for the GRB parameters describing the prompt emission is already so strong, that they are not in the range of Fig. 32 (right) anymore. In contrast to Fig. 32 (left), our approach shows, that IceCube is sensitive to the moderate extended emission GRB if observed on-axis. This results illustrates that with future upgrades of the IceCube detector and good luck in terms of GRB parameters, we will certainly detected neutrinos from GRBs in the near future.

5.6 STRUCTURED JET MODEL

As a last, additional step, we would like to expand our formalism to a general description of the structured jet. For all derivations so far, we assumed, that the Lorentz factor Γ is constant across the top of the jet, describing a *top-hat* jet. But, there are good arguments that a jet might rather have a structured Γ distribution for different regions. The central engine black hole has an accretion disk and accumulated matter in the torus around it in the plane perpendicular to the jet axis. Due to this, the outer regions of jet, which are closer to the accretion disk, have a higher baryonic loading. Since the baryonic loading influences the velocity at which the jet outflow is escaping, these regions experience a smaller Lorentz boost compared to central regions of the jet. This is illustrated in Fig. 33 (b) and visually compared to the top-hat jet (a).

We rewrite the energy fluence per shell in Eq. 5.5, assuming now that the radius, the photon density and Γ depend on the angle θ^*

$$\mathcal{F} = \frac{t_{\text{var}}}{4\pi d_L^2} \int \mathrm{d}\Omega^* \; \Gamma(\theta^*)\mathcal{D}^3(\theta^*) r_{\text{dis}}^2(\theta^*) U'_\gamma(\theta^*)\,. \tag{5.23}$$

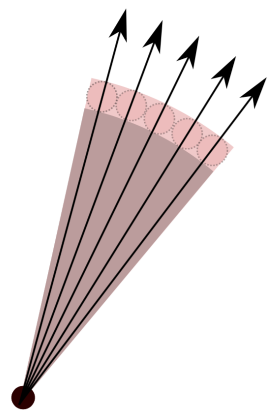

(a) Top Hat Jet

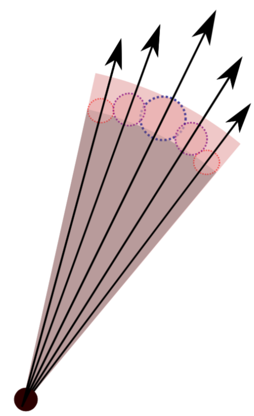

(b) Structured Jet

FIG. 33. Top hat jet (a) versus structured jet (b) with emission regions (grey/coloured circular shaped regions). In the top hat jet, all emission *blobs* move with the same Lorentz factor radial away from the central engine, while for the structured jet the central regions experience a higher Lorentz factor due to the smaller baryonic loading. The black arrows indicate the size of Γ depending on the angle to the jet core axis.

Because the energy and the Lorentz factor depend on the solid angle Ω^*, we express Eq. 5.23 in terms of the bolometric energy per solid angle $\mathrm{d}E^*/\mathrm{d}\Omega^*$ and find

$$\mathcal{F} = \frac{1+z}{4\pi d_L^2} \int \mathrm{d}\Omega^* \; \mathcal{D}^3(\Omega^*) \frac{1}{\Gamma(\theta^*)} \left(\frac{\mathrm{d}E^*}{\mathrm{d}\Omega^*} \right) , \tag{5.24}$$

in the GRB frame with $\widehat{\Gamma}$ and $\widehat{E}$ being the Lorentz factor and the isotropic energy at the jet core. Comparing Eq. 5.24 with Eq. 5.5, we identify the bolometric energy per solid angle to be

$$\frac{\mathrm{d}E^*}{\mathrm{d}\Omega^*} = \frac{1}{4\pi} \Delta r \; 4\pi r_{\mathrm{dis}}^2(\theta^*) U_\gamma'(\theta^*) \Gamma^2(\theta^*) \, , \tag{5.25}$$

with $\Delta r = t_{\mathrm{var}}/(1+z)$. We define for the top-hat jet

$$\frac{\mathrm{d}E^*}{\mathrm{d}\Omega^*} = \frac{\widehat{E}}{4\pi} \Theta(\Delta\theta - \theta^*) \, , \tag{5.26}$$

and

$$\Gamma(\theta^*) = 1 + (\widehat{\Gamma} - 1)\Theta(\Delta\theta - \theta^*) \, . \tag{5.27}$$

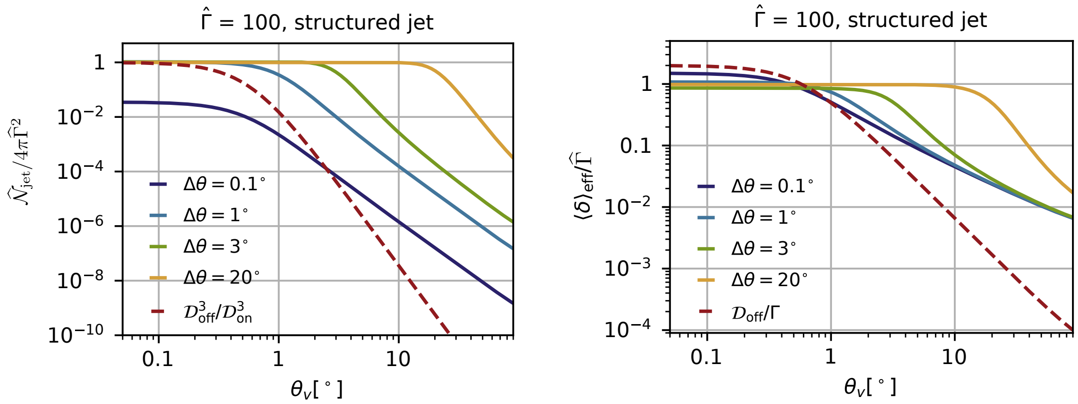

(a) $\widehat{\mathcal{N}}_{\rm jet}$, normalized to $4\pi\widehat{\Gamma}^2$

(b) $\widehat{\langle\delta\rangle}_{\rm eff}$, normalized to $\widehat{\Gamma}$

FIG. 34. $\widehat{\mathcal{N}}_{\rm jet}$ and $\widehat{\langle\delta\rangle}_{\rm eff}$ for the structured jet with $\widehat{\Gamma} = 100$.

With these definitions at hand, Eq. 5.24 reduces to the expression for $\mathcal{F}_\gamma$ we found earlier in Eq. 5.5. But contradictory, Eq. 5.24 allows also a general, structured jet case for which we define [56]

$$\frac{\mathrm{d}E^*}{\mathrm{d}\Omega^*} = \frac{\widehat{E}}{4\pi}\frac{1}{1+(\theta^*/\Delta\theta)^{s_1}}\,, \tag{5.28}$$

and

$$\Gamma(\theta^*) = 1 + \frac{\widehat{\Gamma}-1}{1+(\theta^*/\Delta\theta)^{s_2}}\,, \tag{5.29}$$

where we use s_1=5.5 and s_2=3.5 in the following, as these values are found as best-fit parameter for the specific afterglow emission of GRB 170817A [56]. Expressing the fluence similar to the approach in Eq. 5.11 we formulate

$$\mathcal{F} = \frac{1+z}{4\pi d_L^2}\frac{1}{4\pi\widehat{\Gamma}^2}\mathcal{N}_{\rm jet}\widehat{E}\,, \tag{5.30}$$

with the normalization factor $\widehat{\mathcal{N}}_{\rm jet}$ in this approach being defined as:

$$\widehat{\mathcal{N}}_{\rm jet}(\theta_v) = \int \mathrm{d}\Omega^*\ \mathcal{D}^3(\Omega^*)\frac{\widehat{\Gamma}^2}{\Gamma(\theta^*)}\left(\frac{\mathrm{d}E^*}{\mathrm{d}\Omega^*}\right)/\left(\frac{\widehat{E}}{4\pi}\right)\,. \tag{5.31}$$

The corresponding effective Doppler factor in this this general formulation can be found to be

$$\widehat{\langle\delta\rangle}_{\rm eff} = \int \mathrm{d}\Omega^*\ \mathcal{D}^3(\Omega^*)\frac{1}{\Gamma(\theta^*)}\left(\frac{\mathrm{d}E^*}{\mathrm{d}\Omega^*}\right)\Big/\int \mathrm{d}\Omega^*\ \mathcal{D}^2(\Omega^*)\frac{1}{\Gamma(\theta^*)}\left(\frac{\mathrm{d}E^*}{\mathrm{d}\Omega^*}\right)\,. \tag{5.32}$$

The resulting plots for $\widehat{\mathcal{N}}_{\rm jet}(\theta_v)$ and $\widehat{\langle\delta\rangle}_{\rm eff}$ for the structured jet as function of θ_v are exemplary shown for the $\Gamma = 100$ case in Fig. 34.

Figure 34 shows clearly, that the behaviour of $\widehat{\mathcal{N}}_{\rm jet}(\theta_v)$ and $\widehat{\langle\delta\rangle}_{\rm eff}$ looks very different for the structured jet, compared to the top-hat cases we investigated in Fig. 24 and Fig. 26.

Considering Fig. 34a, we identify that the normalization factor $\widehat{\mathcal{N}}_{\rm jet}$ behaves similar to the top-hat jet for small viewing angles. It is independent of θ_v and reaches the $4\pi\widehat{\Gamma}^2$ approximation asymptotically for $\theta_v \to 0$ and wide jets. In contrast, the structured jet $\widehat{\mathcal{N}}_{\rm jet}$ deviates strongly from an $\mathcal{D}^3$ behaviour for large viewing angles. We observe a similar phenomenon for the $\widehat{\langle\delta\rangle}_{\rm eff}$ structured jet behaviour in Fig. 34b. For small viewing angles, the curves approach $\widehat{\Gamma}$, but not even narrow jets reach the $2\widehat{\Gamma}$ on-axis approximation. For large viewing angles, the curves show significantly higher Doppler factors than for the top-hat jet, presented in Fig. 26.

It should be mentioned, that further investigations of the structured jet are not included in the scope of the Thesis. A publication is in preparation, which summarizes the top-hat jet studies presented here and describes the structured jet in more detail. Please refer to [14].

6 CONCLUSION AND OUTLOOK

With the successful coincident observations of gravitational waves and γ-rays in GW170817/ GRB 170817A and of neutrinos and γ-rays (IceCube-170922A/TXS 0506+056) multi-messenger astronomy gained momentum. Astronomy entered a new area in terms of high-energy observations. In this thesis, we discussed one of the most promising sources to be detected in three messengers, γ-ray bursts. Neutrinos are the missing messenger in observations so far and thus we focused on the predicted neutrino fluence. The neutrino emission is connected to CR emission of GRBs. Therefore, not only would a neutrino detection confirm our models, but it would also approve GRBs as sources of CR acceleration, as these sources are still unknown until these days.

In the course of the thesis presented here, we introduced important aspects of neutrinos and GRBs, which are necessary to predict the flux of neutrinos. We derived an analytical model, that allows calculating the expected neutrino fluence for typical GRB parameters, based on non-neutrino observations. The achievement of this formalism is that off-axis emission under consideration of jet opening angles and jet structures can be modelled. We showed, how on-axis predictions can be scaled by an easy accessible factor to off-axis emission. Additionally, we modified existing IceCube software to predict neutrino fluences from GRB off-axis emission using our derived formalism. We showed that our generalized analytical model is capable to reproduce established results for special cases. One important result is that we find the neutrino prediction for the GW170817/ GRB 170817A event only two orders of magnitude below the IceCube sensitivity level in our description, where it was predicted to be several orders of magnitude lower by an widely used approximate scaling.

This result is of great importance concerning planned upgrades for the neutrino observatory IceCube and the improved sensitivity of the GW detectors LIGO and Virgo. The amount of detected GWs and astrophysical neutrinos will increase significantly and thus the chances become higher, to observe neutrinos from GRBs in coincidence with GWs and γ-rays. The presented work shows that we are able to detect neutrinos from GRB off-axis emission for a lucky interplay of internal GRB parameters. Off-axis emission was so far mostly used to explain the non-observation of neutrinos. But our formalism shows that the effect of off-axis angles is less significant as assumed so far. This assumes that GRB emission jets are generally rather narrow, which was also found experimentally for the GW170817/GRB 170817A observation.

Based on this work, further studies could include the different structure functions of the GRB jets. Detailed studies on the structured jet case can be found in [14], which is based on some of the author's contributions and attached at the end of this document. Also, including neutrino production in external shocks, which is the case for afterglow emission would be interesting to study. For afterglow emission, the Γ factor is expected to decrease, which has an effect on the critical angle $1/\Gamma$ and thus makes observations likely even as off-axis observations. Also, how the spectrum in our model for all observed parameters for the GW170817/GRB170817 A observation looks like would be attractive to investigate. Finally, coincident observations of neutrinos, GWs and γ-rays from a GRB would evoke the ultimate test for our model predictions and will show us, how the missing neutrino piece in the GRB puzzle looks like.

FIG. 35. The missing neutrino piece of the GRB puzzle introduced in section 1. This thesis has the aim to push forward the successful observation and interpretation of neutrinos form GRBs.

REFERENCES

[1] GraceDB. Gravitational-Wave Candidate Event Database. Last revisited: 08/2019: https://gracedb.ligo.org/superevents/public/O3/.

[2] M. G. Aartsen et al. Evidence for High-Energy Extraterrestrial Neutrinos at the IceCube Detector. *Science*, 342:1242856, 2013.

[3] M. G. Aartsen et al. First Observation of PeV-Energy Neutrinos with IceCube. *Phys. Rev. Lett.*, 111:021103, Jul 2013.

[4] M. G. Aartsen et al. Astrophysical neutrinos and cosmic rays observed by IceCube. *Adv. Space Res.*, 62:2902–2930, 2018.

[5] M. G. Aartsen et al. Multimessenger observations of a flaring blazar coincident with high-energy neutrino IceCube-170922A. *Science*, 361(6398):eaat1378, 2018.

[6] J. Aasi et al. Advanced LIGO. *Class. Quant. Grav.*, 32:074001, 2015.

[7] B. P. Abbott et al. Observation of Gravitational Waves from a Binary Black Hole Merger. *Phys. Rev. Lett.*, 116(6):061102, 2016.

[8] B. P. Abbott et al. Gravitational Waves and Gamma-rays from a Binary Neutron Star Merger: GW170817 and GRB 170817A. *Astrophys. J.*, 848(2):L13, 2017.

[9] B. P. Abbott et al. GW170817: Observation of Gravitational Waves from a Binary Neutron Star Inspiral. *Phys. Rev. Lett.*, 119(16):161101, 2017.

[10] B. P. Abbott et al. Multi-messenger Observations of a Binary Neutron Star Merger. *Astrophys. J.*, 848(2):L12, 2017.

[11] B. P. Abbott et al. GWTC-1: A Gravitational-Wave Transient Catalog of Compact Binary Mergers Observed by LIGO and Virgo during the First and Second Observing Runs. 2018.

[12] M. Ahlers. *Fireballet* - A fireball emission tool, Internal IceCube Software Manual, 2012.

[13] M. Ahlers. High-Energy Neutrinos. Talk at the ISAPP Texel, 2017.

[14] M. Ahlers and L. Halser. Neutrino Fluence from Gamma-Ray Bursts: Off-Axis View of Structured Jets. 2019. Attached to this document.

[15] M. Ahlers, K. Helbing, and C. Pérez de los Heros. Probing Particle Physics with IceCube. *Eur. Phys. J.*, C78(11):924, 2018.

[16] A. Albert et al. Search for High-energy Neutrinos from Binary Neutron Star Merger GW170817 with ANTARES, IceCube, and the Pierre Auger Observatory. *Astrophys. J.*, 850(2):L35, 2017.

[17] D. Band et al. BATSE observations of gamma-ray burst spectra. I - Spectral diversity. *apj*, 413:281–292, Aug. 1993.

[18] V. Barger, D. Marfatia, and K. Whisnant. *The Physics of Neutrinos.* Princeton University Press, Princeton, N.J, course book edition, 2012.

[19] P. Bhattacharjee and G. Sigl. Origin and propagation of extremely high-energy cosmic rays. *Phys. Rept.*, 327:109–247, 2000.

[20] A. Bhattacharya, R. Gandhi, W. Rodejohann, and A. Watanabe. The Glashow resonance at IceCube: signatures, event rates and pp vs. $p\gamma$ interactions. *JCAP*, 1110:017, 2011.

[21] D. Biehl, J. Heinze, and W. Winter. Expected neutrino fluence from short Gamma-Ray Burst 170817A and off-axis angle. *Mon. Not. Roy. Astron. Soc.*, 476(1):1191–1197, 2018.

[22] R. M. Bionta et al. Observation of a Neutrino Burst in Coincidence with Supernova SN 1987a in the Large Magellanic Cloud. *Phys. Rev. Lett.*, 58:1494, 1987.

[23] F. Capozzi, E. Di Valentino, E. Lisi, A. Marrone, A. Melchiorri, and A. Palazzo. Global constraints on absolute neutrino masses and their ordering. *Phys. Rev.*, D95(9):096014, 2017.

[24] S. Carroll. *Spacetime and geometry, an introduction to general relativity.* Pearson, New York, pearson new international edition edition, 2014.

[25] C. Chen and C. Cardot. A Catalog of Astrophysical Neutrino Candidates for IceCube. 2019.

[26] I. Collaboration. IceCube Media Gallery. The Detector. Last revisited: 08/2019, https://icecube.wisc.edu/gallery/press/view/1336.

[27] L. Collaboration. LIGO Technology, Last revisted: 08/2019. Last revisited 07/2019: https://www.ligo.caltech.edu/page/ligo-technology.

[28] W. Commons. File:Standard Model of Elementary Particles.svg, 2018. https://en.wikipedia.org/wiki/Standard_Model#/media/File:Standard_Model_of_ Elementary_Particles.svg.

[29] O. Cremonesi. Neutrino-less double beta decay experiments. *Hyperfine Interact.*, 239(1):54, 2018.

[30] I. Esteban et al. Global analysis of three-flavour neutrino oscillations: synergies and tensions in the determination of $\theta_2 3, \delta_C P$, and the mass ordering. *JHEP*, 01:106, 2019.

[31] B. Falkenburg and W. Rhode, editors. *From Ultra Rays to Astroparticles*. Springer, Dordrecht, Netherlands, 2012.

[32] J. A. Formaggio and G. P. Zeller. From eV to EeV: Neutrino Cross Sections Across Energy Scales. *Rev. Mod. Phys.*, 84:1307–1341, 2012.

[33] A. Franckowiak. Multimessenger Astronomy with Neutrinos. *Journal of Physics: Conference Series*, 888:012009, Sep 2017.

[34] T. K. Gaisser, R. Engel, and E. Resconi. *Cosmic Rays and Particle Physics*. Cambridge Universti Press, Cambridge, 2nd [fully updated] ed. edition, 2016.

[35] S. L. Glashow. Resonant Scattering of Antineutrinos. *Phys. Rev.*, 118:316–317, Apr 1960.

[36] F. Halzen and S. R. Klein. IceCube: An Instrument for Neutrino Astronomy. *Rev. Sci. Instrum.*, 81:081101, 2010.

[37] P. F. Harrison, D. H. Perkins, and W. G. Scott. Tri-bimaximal mixing and the neutrino oscillation data. *Phys. Lett.*, B530:167, 2002.

[38] S. Hummer, P. Baerwald, and W. Winter. Neutrino Emission from Gamma-Ray Burst Fireballs, Revised. *Phys. Rev. Lett.*, 108:231101, 2012.

[39] K. Ioka and T. Nakamura. Can an Off-axis Gamma-Ray Burst Jet in GW170817 Explain All the Electromagnetic Counterparts? *PTEP*, 2018(4):043E02, 2018.

[40] J. Jones, I. Mocioiu, M. H. Reno, and I. Sarcevic. Tracing very high-energy neutrinos from cosmological distances in ice. *Phys. Rev.*, D69:033004, 2004.

[41] S. S. Kimura, K. Murase, P. Mészáros, and K. Kiuchi. High-Energy Neutrino Emission from Short Gamma-Ray Bursts: Prospects for Coincident Detection with Gravitational Waves. *Astrophys. J.*, 848(1):L4, 2017.

[42] R. W. Klebesand, I. B. Strong, and R. A. Olson. Observations of Gamma-Ray Bursts of Cosmic Origin. *Astrophysical Journal, vol. 182, p.L85*, 1976.

[43] G. R. . A. Lightman. *Radiative Processes in Astrophysics*. WILEY-VCH Verlag GmbH & Co. KGaA, Weinheim, 2004.

[44] P. Lipari, M. Lusignoli, and D. Meloni. Flavor Composition and Energy Spectrum of Astrophysical Neutrinos. *Phys. Rev.*, D75:123005, 2007.

[45] R. S. Mallozi. BATSE GRB Durations, 2018. https://gammaray.msfc.nasa.gov/batse/grb/duration/.

[46] P. Meszaros. Gamma-Ray Bursts. *Rept. Prog. Phys.*, 69:2259–2322, 2006.

[47] A. Mucke, R. Engel, J. P. Rachen, R. J. Protheroe, and T. Stanev. SOPHIA: Monte Carlo simulations of photohadronic processes in astrophysics. *Comput. Phys. Commun.*, 124:290–314, 2000.

[48] K. Murase and I. Bartos. High-Energy Multi-Messenger Transient Astrophysics. 2019.

[49] K. Murase and S. Nagataki. High Energy Neutrino Flash from Far-UV/X-ray Flares of Gamma-Ray Bursts. *Phys. Rev. Lett.*, 97:051101, 2006.

[50] W. S. Paciesas et al. The Fourth batse gamma-ray burst catalog (revised). *Astrophys. J. Suppl.*, 122:465–495, 1999.

[51] W. Pauli. Offener Brief an die Gruppe der Radioaktiven bei der Gauvereins- zu Tuebingen, 1930.

[52] J. P. Rachen and P. Meszaros. Photohadronic neutrinos from transients in astrophysical sources. *Phys. Rev.*, D58:123005, 1998.

[53] W. Rodejohann. Neutrino-less Double Beta Decay and Particle Physics. *Int. J. Mod. Phys.*, E20:1833–1930, 2011.

[54] S. Roy Choudhury and S. Hannestad. Updated results on neutrino mass and mass hierarchy from cosmology with Planck 2018 likelihoods. 2019.

[55] B. Ryden and B. M. Peterson. *Foundations of astrophysics.* Addison-Wesley, San Francisco, 2010.

[56] O. S. Salafia, G. Ghirlanda, S. Ascenzi, and G. Ghisellini. The on-axis view of GRB 170817A. *Astron. Astrophys.*, 628:A18, 2019.

[57] O. S. Salafia, G. Ghisellini, A. Pescalli, G. Ghirlanda, and F. Nappo. Structure of Gamma-Ray Burst jets: intrinsic versus apparent properties. *Mon. Not. Roy. Astron. Soc.*, 450(4):3549–3558, 2015.

[58] A. Y. Smirnov. The Mikheyev-Smirnov-Wolfenstein (MSW) Effect. In *International Conference on History of the Neutrino: 1930-2018 Paris, France, September 5-7, 2018*, 2019.

[59] M. Tanabashi et al. Review of Particle Physics. *Phys. Rev. D*, 98:030001, Aug 2018.

[60] M. Thomson. *Modern particle physics.* Cambridge University Press, Cambridge, 2013.

[61] T. Thummler. Introduction to direct neutrino mass measurements and KATRIN. *Nucl. Phys. Proc. Suppl.*, 229-232:146–151, 2012.

[62] D. Tosi. The search for neutrino-less double-beta decay: summary of current experiments. In *Proceedings, 14th ICATPP Conference on Astroparticle, Particle, Space Physics and Detectors for Physics Applications (ICATPP 2013): Como, Italy, September 23-27, 2013*, pages 304–314, 2014.

[63] G. Vedrenne and J.-L. Atteia. *Gamma-ray bursts, the brightest explosions in the universe.* Springer Praxis books in astronomy and planetary sciences. Springer In association with Praxis, Berlin New York Chichester, UK, 2009.

[64] E. Waxman and J. N. Bahcall. High-energy neutrinos from cosmological gamma-ray burst fireballs. *Phys. Rev. Lett.*, 78:2292–2295, 1997.

[65] Y. Wu and A. MacFadyen. Constraining the Outflow Structure of the Binary Neutron Star Merger Event GW170817/GRB170817A with a Markov Chain Monte Carlo Analysis. *Astrophys. J.*, 869(1):55, 2018.

[66] Y.-R. Yen. Status of the KATRIN neutrino mass experiment. In *8th Meeting on CPT and Lorentz Symmetry (CPT'19) Bloomington, Indiana, USA, May 12-16, 2019*, 2019.

[67] B. Zhang. *The Physics of Gamma-Ray Bursts.* Cambridge University Press, Cambridge, UK, 2019.

APPENDIX A

This derivation follows very closely the one in [43].
Neutrinos move along null-geodesics within all frames, which means that $c^2 \mathrm{d}t^2 - \mathrm{d}r^2 = 0$, but also $c^2 \mathrm{d}t'^2 - \mathrm{d}r'^2 = 0$. Therefore we can write for the GRB and observer frame:

$$\mathrm{d}t' = \mathrm{d}t' \tag{A.1}$$

$$\mathrm{d}t = \mathrm{d}r \tag{A.2}$$

This can be set into relation by a Lorentz transformation. For the time and all three spatial coordinates, we obtain separately

$$\begin{aligned} \mathrm{d}t &= \Gamma(\mathrm{d}t' + \beta/c\ \mathrm{d}x') \\ \mathrm{d}x &= \Gamma(\mathrm{d}x' + \beta\ c\ \mathrm{d}t') \\ \mathrm{d}y &= \mathrm{d}y' \\ \mathrm{d}z &= \mathrm{d}z' \end{aligned}$$

Writing out the velocity u in x-direction in the GRB-frame

$$\begin{aligned} u_x &= \frac{\mathrm{d}x}{\mathrm{d}t} \\ &= \frac{\Gamma(\mathrm{d}x' + \beta\ c\ \mathrm{d}t')}{\Gamma(\mathrm{d}t' + \beta/c\ \mathrm{d}x')} \\ &= \frac{u'_x + \beta\ c}{1 + u_x \beta/c} \qquad \text{(A.3)} \\ u_y &= \frac{u'_y}{\Gamma(1 + \beta/c u'_x)} \qquad \text{(A.4)} \end{aligned}$$

Assuming a more general velocity v, which has components in x- and y-direction, leads to the "new interpretation" of Eq. A.3 and Eq. A.4: $u_x = u_\perp$ and $u_y = u_\parallel$. We derive:

$$\tan(\theta) = \frac{u_\parallel}{u_\perp} \tag{A.5}$$

$$\cos(\theta) = \frac{u_\perp}{v} \tag{A.6}$$

Using eq. (A.6) gives the laboured result:

$$
\begin{aligned}
\cos(\theta) &= \frac{u_\perp}{v} \\
&= \frac{1}{v}\left(\frac{u'_\parallel + \beta\ c}{1+\beta/cu'_\parallel}\right) \\
&= \frac{\frac{c}{v}cos(\theta')+1}{\frac{1}{v}+\frac{\beta}{v}\cos\theta'} \\
&= \frac{\cos(\theta')+\beta}{1+\beta\cos(\theta')}
\end{aligned}
\tag{A.7}
$$

$\beta = v/c$ and $u'_\parallel = c\cos(\theta')$ is applied when going from the second to the third line. In the last step, $v = c \sim 1$ is assumed.

APPENDIX B

We calculate the neutrino spectra for fixed luminosity in Section 5.4.4. However, the first checks were made for a fixed fluence instead. This is the default configuration in FIREBALLET. For this case, we keep the fluence the same for all off-axis angles and only change $\mathcal{N}_{\rm jet}$ and $\langle\delta\rangle_{\rm eff}$. This means physically that we observe multiple sources from different observation angles. For all sources the same fluence is measured, which means internally they are different in luminosity due to the different viewing angles under which we observe them.

The result for all three cases can be seen in Fig. 36. Here we report that the change in the spectrum is large for large Γ boosts. While in the extended emission optimistic case we only experience little changes in the vertical direction, we see a huge difference, not only in vertical but also horizontal direction. For the prompt case, the shape of the spectrum changes drastically.

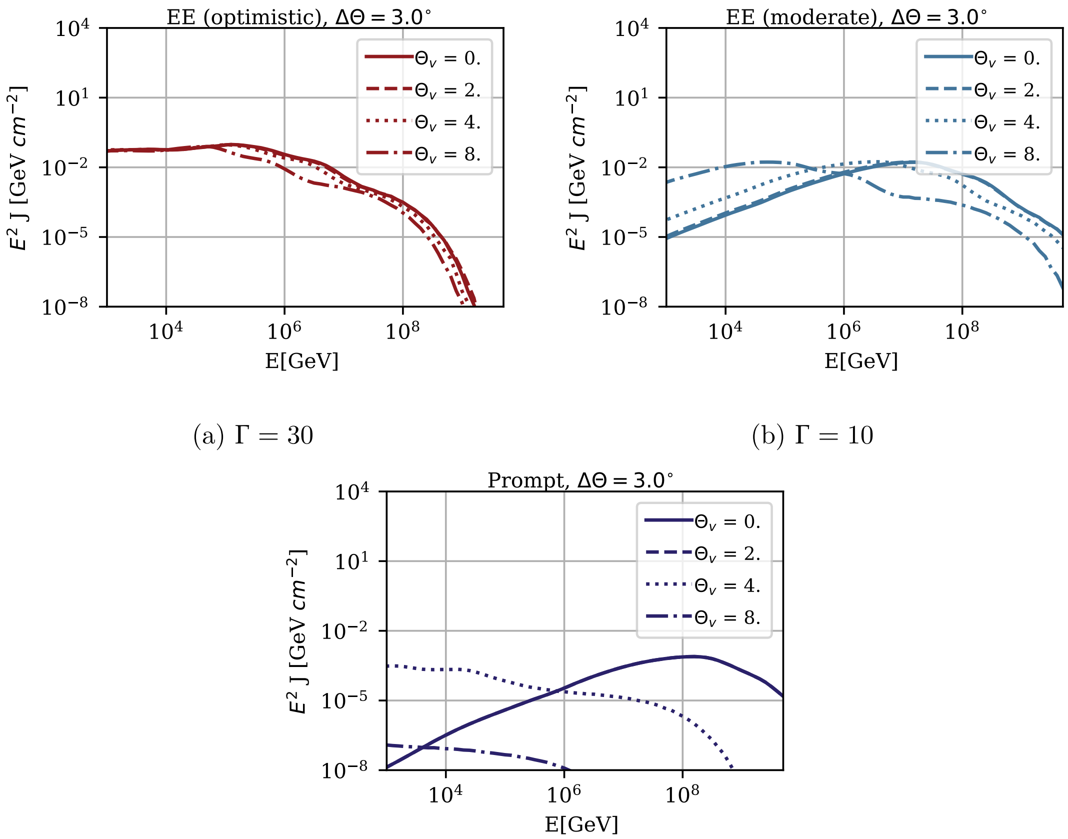

(a) $\Gamma = 30$

(b) $\Gamma = 10$

(c) $\Gamma = 1000$

FIG. 36. Off-axis scaling for the three GRB models with fixed energy fluence $\mathcal{F}$.

Neutrino Fluence from Gamma-Ray Bursts: Off-Axis View of Structured Jets

Markus Ahlers & Lea Halser
Niels Bohr International Academy & Discovery Center, Niels Bohr Institute, University of Copenhagen, DK-2100 Copenhagen, DK

arXiv:1908.06953v1 [astro-ph.HE] 19 Aug 2019

ABSTRACT
We investigate the expected high-energy neutrino fluence from internal shocks produced in the relativistic outflow of gamma-ray bursts. Previous model predictions have primarily focussed on on-axis observations of uniform jets. Here we present a generalization to account for arbitrary viewing angles and jet structures. Based on this formalism, we provide an improved scaling relation that expresses off-axis neutrino fluences in terms of on-axis model predictions. We also find that the neutrino fluence from structured jets can exhibit a strong angular dependence relative to that of γ-rays and can be far more extended. We examine this behavior in detail for the recent short gamma-ray burst GRB 170817A observed in coincidence with the gravitational wave event GW170817.

Key words: gamma-ray burst – neutrinos

1 INTRODUCTION

Gamma-Ray Bursts (GRBs) are some of the most energetic transient phenomena in our Universe that dominate the γ-ray sky over their brief existence. The burst duration, ranging from milliseconds to a few minutes, requires central engines that release their energy explosively into a compact volume of space. The GRB data show a bimodal distribution of long ($\gtrsim 2$s) and short bursts, indicating different progenitor systems. The origin of long-duration GRBs has now been established as the core-collapse of massive stars (Woosley 1993) by the association with type Ibc supernovae in a few cases (Hjorth & Bloom 2012). The recent observation of GRB 170817A in association with the gravitational wave GW170817 (Abbott et al. 2017a,b) has confirmed the idea that (at least some) short-duration GRB originate from binary neutron star mergers (Paczynski 1986; Eichler et al. 1989; Narayan et al. 1992). The subsequent multi-wavelength observations of this system also provided evidence for an associated kilonova/macronova from merger ejecta (Villar et al. 2017) and allowed for a detailed study of the jet structure by the late-time GRB afterglow (Lazzati et al. 2018; Troja et al. 2018; Margutti et al. 2018; Lamb et al. 2019; Ghirlanda et al. 2019; Lyman et al. 2018).

After core-collapse or merger, the nascent compact remnant – a black hole or rapidly spinning neutron star – is initially girded by a thick gas torus from which it starts to accrete matter at a rate of up to a few solar masses per second. The system is expected to launch axisymmetric outflows via the deposition of energy and/or momentum above the poles of the compact remnant. The underlying mechanism is uncertain and could be related to neutrino pair annihilation powered by neutrino emission of a hyper-accreting disk (Popham et al. 1999) or magnetohydrodynamical processes that extract the rotational energy of a remnant black hole (Blandford & Znajek 1977). The interaction of the expanding and accelerating outflow with the accretion torus collimates the outflow into a jet. Subsequent interactions with dynamical merger ejecta or the stellar envelope further collimate and shape the jet until it emerges (or not) from the progenitor environment. We refer to Zhang (2018) for a recent detailed review of the status of GRB observations and models.

For the remainder of this paper, we will assume that the prompt γ-ray display is related to energy dissipation in the jet via internal shocks (Rees & Mészáros 1994; Paczynski & Xu 1994). The variability of the central engine can result in variations of the Lorentz factor in individual sub-shells of the outflow that eventually collide (Shemi & Piran 1990; Rees & Mészáros 1992; Mészáros & Rees 1993). Electrons accelerated by first order Fermi acceleration in the internal shock environment radiate via synchrotron emission, which can contribute to or event dominate the observed prompt γ-ray display (Rees & Mészáros 1994; Paczynski & Xu 1994). In order to be visible, these internal shocks have to occur above the photosphere, where the jet becomes optically thin to Thomson scattering. However, it has been argued that the dissipation of bulk jet motion via (combinations of) internal shocks, magnetic reconnection or neutron-proton collisions close to the photosphere can also produce the typical GRB phenomenology (Rees & Mészáros 2005; Ioka et al. 2007; Beloborodov 2010; Lazzati & Begelman 2010). Eventually, the collision of the fireball with interstellar gas forms external shocks that can explain the GRB afterglow ranging from radio to X-ray frequencies (Mészáros et al. 1994; Mészáros & Rees 1994).

Baryons entrained in the jet are inevitably accelerated along with the electrons in internal shocks. Waxman (1995) argued that a typical GRB environment can satisfy the requirements to accelerate cosmic rays to the extreme energies of beyond 10^{20} eV observed on Earth. A smoking-gun test of this scenario is the production of high-energy neutrinos from the decay of charged pions and kaons produced by

© 2019 The Authors

CR interactions with the internal photon background (Waxman & Bahcall 1997; Guetta et al. 2004; Murase & Nagataki 2006; Zhang & Kumar 2013). Searches of neutrino emission of GRBs with the IceCube neutrino observatory at the South Pole has put meaningful constraints on the neutrino emission of GRBs (Ahlers et al. 2011; Abbasi et al. 2012; Aartsen et al. 2017) and has triggered various model revisions (Murase et al. 2006; Li 2012; Hummer et al. 2012; He et al. 2012; Murase & Ioka 2013; Senno et al. 2016; Denton & Tamborra 2018).

Most GRB neutrino predictions are based on on-axis observations of a uniform jet with constant bulk Lorentz factor Γ within a half-opening angle $\Delta\theta$ that is significantly larger than the kinematic angle $1/\Gamma$. The apparent brightness of the source is then significantly enhanced due to the strong Doppler boost of the emission. However, the recent observations of GRB 170817A & GW170817 (Abbott et al. 2017a,b) and the multi-wavelength emission of its late-time afterglow (Lazzati et al. 2018) has confirmed earlier speculations that the GRB jet is structured. This explains the brightness of the GRB despite our large viewing angle of $\gtrsim 15°$.

In this paper, we study the neutrino fluence in the internal shock model of GRBs for arbitrary viewing angles and jet structures. In section 2 we will provide a detailed derivation of the relation between the internal emissivity of the GRB and the fluence for an observer at arbitrary relative viewing angles. Our formalism will clarify some misconceptions that have appeared in the literature and provide an improved scaling relation of the particle fluence. In section 3 we will study off-axis emission for various jet structures and determine a revised scaling relation that allows to express off-axis fluence predictions based on on-axis models. We then study neutrino emission from internal shocks in structured jets in section 4 and show that the emissivity of neutrinos is expected to have a strong angular dependence relative to the γ-ray display. We illustrate this behavior in section 5 for a structured jet model inferred from the afterglow of GRB 170817A before we conclude in section 6.

Throughout this paper we work with natural Heaviside-Lorentz units with $\hbar = c = \varepsilon_0 = \mu_0 = 1$, $\alpha = e^2/(4\pi) \simeq 1/137$ and $1\ \mathrm{G} \simeq 1.95\times10^{-2}\ \mathrm{eV}^2$. Boldface quantities indicate vectors.

2 PROMPT EMISSION FROM RELATIVISTIC SHELLS

The general relation of the energy fluence $\mathcal{F}$ (units of GeV cm^{-2}) from structured jets observed under arbitrary viewing angles can be determined via the specific emissivity j (units of cm^{-3} s^{-1} sr^{-1}). This ansatz has been used by Granot et al. (1999), Woods & Loeb (1999), Nakamura & Ioka (2001) and Salafia et al. (2016) to derive the time-dependent electromagnetic emission of GRBs. The dependence of the isotropic-equivalent energy on jet structure and viewing angle has been studied by Yamazaki et al. (2003), Eichler & Levinson (2004) and Salafia et al. (2015). We present here a simple and concise derivation of this relation for thin relativistic shells, also accounting for cosmological redshift. The resulting expressions will allow us to relate the photon density in the structured jet to the observed prompt γ-ray fluence and to determine the efficiency of neutrino emission from cosmic ray interactions in colliding sub-shells.

A sketch of the variable GRB outflow and the resulting collision of sub-shells is shown in Fig. 1. In the observer's rest frame, the fluence per area dA from individual elements of a merged shell is related to the emission into a solid angle

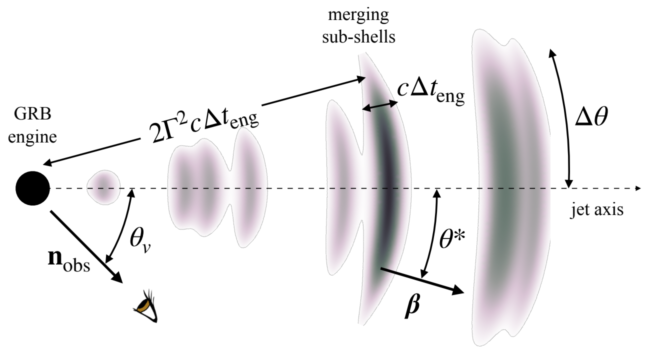

Figure 1. Sketch of colliding sub-shells of a variable GRB outflow. Sub-shells with different bulk Lorentz factors $\Delta\Gamma \sim \Gamma$ that are emitted from the GRB engine with time difference $\Delta t_{\rm eng}$ merge at a distance $r_{\rm dis} \sim 2\Gamma^2 c\Delta t_{\rm eng}$ and dissipate bulk kinetic energy. Internal shocks accelerate electrons and protons and contribute to the non-thermal emission of the merged shell. Emission along the shell is boosted into the observer frame along a radial velocity vector $\boldsymbol{\beta}(\Omega^*)$. The observer sees the emission under a viewing angle θ_v in the direction $\mathbf{n}_{\rm obs}$.

$\mathrm{d}\Omega = \mathrm{d}A/d_A^2$ for a source at angular diameter distance d_A. The combined emission of one shell is therefore

$$\mathcal{F} = \frac{1}{d_A^2}\int \mathrm{d}V \int \mathrm{d}\epsilon \int \mathrm{d}t\, j\,. \tag{1}$$

The specific emissivity j in the observer's reference frame is related to the specific emissivity j' in the rest frame of the sub-shell (denoted by primed quantities in the following) as (Rybicki & Lightman 1979)

$$j = \frac{\mathcal{D}^2}{(1+z)^2} j'\,, \tag{2}$$

where z denotes the redshift of the source and $\mathcal{D}$ the Doppler factor of the specific volume element. In the following, we will assume that the jet structure in the GRB's rest frame (denoted by starred quantities in the following) is axisymmetric. The spherical coordinate system is parametrized by zenith angle θ^* and azimuth angle ϕ^* such that the jet axis aligns with the $\theta^* = 0$ direction. Note that we do not account for the counter-jet in our calculation, but this addition is trivial. At a sufficiently large distance from the central engine, the jet flow is assumed to be radial. The relative viewing angle between the observer and jet axis is denoted as θ_v. The Doppler factor can then be expressed as

$$\mathcal{D}(\Omega^*) = \left[\Gamma(\theta^*)(1 - \boldsymbol{\beta}(\Omega^*)\cdot\mathbf{n}_{\rm obs})\right]^{-1}\,, \tag{3}$$

where $\boldsymbol{\beta}(\Omega^*)$ corresponds to the radial velocity vector of the specific volume element in the GRB's rest frame and $\mathbf{n}_{\rm obs}$ is a unit vector pointing towards the location of the observer. Due to the symmetry of the jet we can express the scalar product in (3) as

$$\boldsymbol{\beta}(\Omega^*)\cdot\mathbf{n}_{\rm obs} = \beta(\theta^*)\left(\sin\theta^*\cos\phi^*\sin\theta_v + \cos\theta^*\cos\theta_v\right)\,. \tag{4}$$

Using the transformation of energy $\epsilon' = (1+z)\epsilon/\mathcal{D}$, volume $V' = (1+z)V/\mathcal{D}$ and time $t' = t\mathcal{D}/(1+z)$, we can express Eq. (1) as

$$\mathcal{F} = \frac{1+z}{d_L^2}\int \mathrm{d}V' \int \mathrm{d}\epsilon' \int \mathrm{d}t' \mathcal{D}^3(\Omega^*) j'\,. \tag{5}$$

In this expression we have used the relation $d_L(z) = (1+z)^2 d_A(z)$ between the luminosity and angular diameter distance for a source at redshift z.

The infinitesimal volume element $\mathrm{d}V'$ in the rest frame of the sub-shell is related to the volume element $\mathrm{d}V^*$ in the frame of the central engine as $\mathrm{d}V' = \Gamma(\theta^*)\mathrm{d}V^*$. In the internal shock model, the shell radius and width (in the central engine frame) can be related to the variability time scale $\Delta t_{\rm eng}$ of the central engine as $r_{\rm dis} \simeq 2\Gamma^2 c\Delta t_{\rm eng}$ and $\Delta r \simeq c\Delta t_{\rm eng}$. The time-integrated emissivity can then be expressed as a sum over $N_{\rm sh}$ merging sub-shells with width Δr that appear at a characteristic distance $r_{\rm dis}$,

$$j^*(\theta^*) \simeq N_{\rm sh}\Delta r(\theta^*)\delta(r^* - r_{\rm dis}(\theta^*))j^*_{\rm IC}(\theta^*)\,. \tag{6}$$

The total number of colliding sub-shells can be estimated by the total engine activity $T_{\rm GRB}$ as $N_{\rm sh} \simeq \xi T_{\rm GRB}/\Delta t_{\rm eng}$ where we have introduced an intermittency factor $\xi \leq 1$. For simplicity, we will assume in the following that the total engine activity is related to the observation time as $T_{\rm GRB} \simeq T_{90}/(1+z)$ and $\xi = 1$. Note that the observed variability time-scale $t_{\rm var}$ of a thin jet with viewing angle $\theta_{\rm obs}$ can be related to the engine time scale as $t_{\rm var}/\Delta t_{\rm eng} \simeq \mathcal{D}(0)/\mathcal{D}(\theta_{\rm obs})$, whereas the total observed emission T_{90} is only marginally effected by the off-axis emission (Salafia et al. 2016).

The specific emissivity $j'_{\rm IC}$ in the rest frame of the sub-shell is assumed to be isotropic. The time-integrated emission can therefore be expressed in terms of a spectral density:

$$n'(\theta^*) = 4\pi \int \mathrm{d}t' j'_{\rm IC}(\theta^*)\,. \tag{7}$$

The background of relativistic particles in the shell rest frame contributes to the total internal energy density of the shell as

$$u'(\theta^*) = \int \mathrm{d}\epsilon' \epsilon' n'(\theta^*)\,. \tag{8}$$

This allows us to express the observed fluence by the internal energy density as:

$$\mathcal{F} \simeq \frac{cT_{90}}{4\pi d_L^2} \int \mathrm{d}\Omega^* \Gamma(\theta^*)\mathcal{D}^3(\Omega^*) r^2_{\rm dis}(\theta^*) u'(\theta^*)\,. \tag{9}$$

This is the most general expression for the prompt fluence emitted from a thin shell of an axisymmetric radial jet.

3 JET STRUCTURE AND OFF-AXIS SCALING

The previous discussion simplifies if we can consider an emission region that moves at a constant velocity $\boldsymbol{\beta}$. The energy fluence $\mathcal{F}$ in the observer's rest frame is then related to the bolometric energy E' in the source rest frame as (Granot et al. 2002)

$$\mathcal{F} = \frac{1+z}{4\pi d_L^2}\mathcal{D}^3 E'\,, \tag{10}$$

with $\mathcal{D} = [\Gamma(1 - \boldsymbol{\beta}\cdot\mathbf{n}_{\rm obs})]^{-1}$. This approximates the case of a thin GRB jet observed at large viewing angle, $\theta_v \gg \Delta\theta$ and $\theta_v \gg 1/\Gamma$. In this case expression (10) allows to estimate the off-axis emission from on-axis predictions by re-scaling the particle fluence F (units of GeV^{-1} cm^{-2}) by a factor $\eta = \mathcal{D}_{\rm off}/\mathcal{D}_{\rm on}$ as

$$F_{\rm off}(\epsilon) = \eta F_{\rm on}(\epsilon/\eta)\,, \tag{11}$$

where $\mathcal{D}_{\rm off}$ accounts for the viewing angle with respect to the jet boundary. This simple approximation was chosen by Albert et al. (2017) to account for the off-axis scaling of on-axis neutrino fluence predictions by Kimura et al. (2017) for the case of GRB 170817A. However, this scaling approach can only be considered to be a first order approximation and does not capture all relativistic effects, including intermediate situations where the kinematic angle $1/\Gamma$ becomes comparable to the viewing angle or jet opening angle or more complex situations of structured jets (see also the discussion by Biehl et al. (2018)).

In the following we will derive a generalization of the naive scaling relation (11) that applies to a larger class of jet structures and relative viewing angles. Expression (9) derived in the previous section relates the observed fluence in photons or neutrinos to their internal energy density in the rest frame of the shell. The distribution of total energy and Lorentz factor with respect to the solid angle Ω^* is determined by the physics of the central engine and its interaction with the remnant progenitor environment before the jet emerges. It is therefore convenient to rewrite Eq. (9) in terms of a bolometric energy per solid angle in the GRB's rest frame (Salafia et al. 2015),

$$\mathcal{F} = \frac{1+z}{4\pi d_L^2}\int \mathrm{d}\Omega^* \frac{\mathcal{D}^3(\Omega^*)}{\Gamma(\theta^*)}\frac{\mathrm{d}E^*}{\mathrm{d}\Omega^*}\,. \tag{12}$$

Using the relation $\mathrm{d}E^*/\mathrm{d}\Omega^* = \Gamma\mathrm{d}E'/\mathrm{d}\Omega^*$, one can recognize Eq. (12) as the natural extension of Eq. (10) for a spherical distribution of emitters. We can identify the angular distribution of internal energy from Eq. (9) as

$$\frac{\mathrm{d}E^*}{\mathrm{d}\Omega^*} = \frac{1}{4\pi}cT_{\rm GRB}4\pi r^2_{\rm dis}(\theta^*)\Gamma^2(\theta^*)u'(\theta^*)\,. \tag{13}$$

The jet structures that we are going to investigate in the following are parametrized in terms of the angular dependence of the Lorentz factor $\Gamma(\theta^*)$ and the kinetic energy $\mathrm{d}E^*/\mathrm{d}\Omega^*$ in the engine's rest frame. We will consider two cases:
(i) a *top-hat* (uniform) jet with

$$\frac{\mathrm{d}E^*}{\mathrm{d}\Omega^*} = \frac{\widehat{E}}{4\pi}\Theta(\Delta\theta - \theta^*)\,, \tag{14}$$

and

$$\Gamma(\theta^*) = 1 + (\widehat{\Gamma} - 1)\Theta(\Delta\theta - \theta^*)\,, \tag{15}$$

corresponding to a constant Lorentz factor $\widehat{\Gamma}$ within a half-opening angle $\Delta\theta$ and

(ii) a *structured* jet with

$$\frac{\mathrm{d}E^*}{\mathrm{d}\Omega^*} = \frac{\widehat{E}}{4\pi}\frac{1}{1 + (\theta^*/\Delta\theta)^{s_1}}\,, \tag{16}$$

and

$$\Gamma(\theta^*) = 1 + \frac{\widehat{\Gamma} - 1}{1 + (\theta^*/\Delta\theta)^{s_2}}\,. \tag{17}$$

Both jet models are normalized to the core energy $\widehat{E}$ and Lorentz factor $\widehat{\Gamma}$ at the jet core. We use $s_1 = 5.5$ and $s_2 = 3.5$ in the following, corresponding to the best-fit parameters for the afterglow emission of GRB 170817A (Ghirlanda et al. 2019). Note that in the limit $s_1 \to \infty$ and $s_2 \to \infty$, the structured jet is identical to the top-hat jet.

With these two jet models, we can now study the generalized off-axis scaling of the fluence (12). It is convenient to express the energy fluence (12) in a form similar to the special case (10) as

$$\mathcal{F} = \frac{1+z}{4\pi d_L^2}\mathcal{N}_{\rm jet}\widehat{E}\,, \tag{18}$$

where we introduce the jet scaling factor

$$\mathcal{N}_{\rm jet}(\theta_v) \equiv \int \mathrm{d}\Omega^* \frac{\mathcal{D}^3(\Omega^*)}{\Gamma(\theta^*)}\frac{1}{\widehat{E}}\frac{\mathrm{d}E^*}{\mathrm{d}\Omega^*}\,. \tag{19}$$

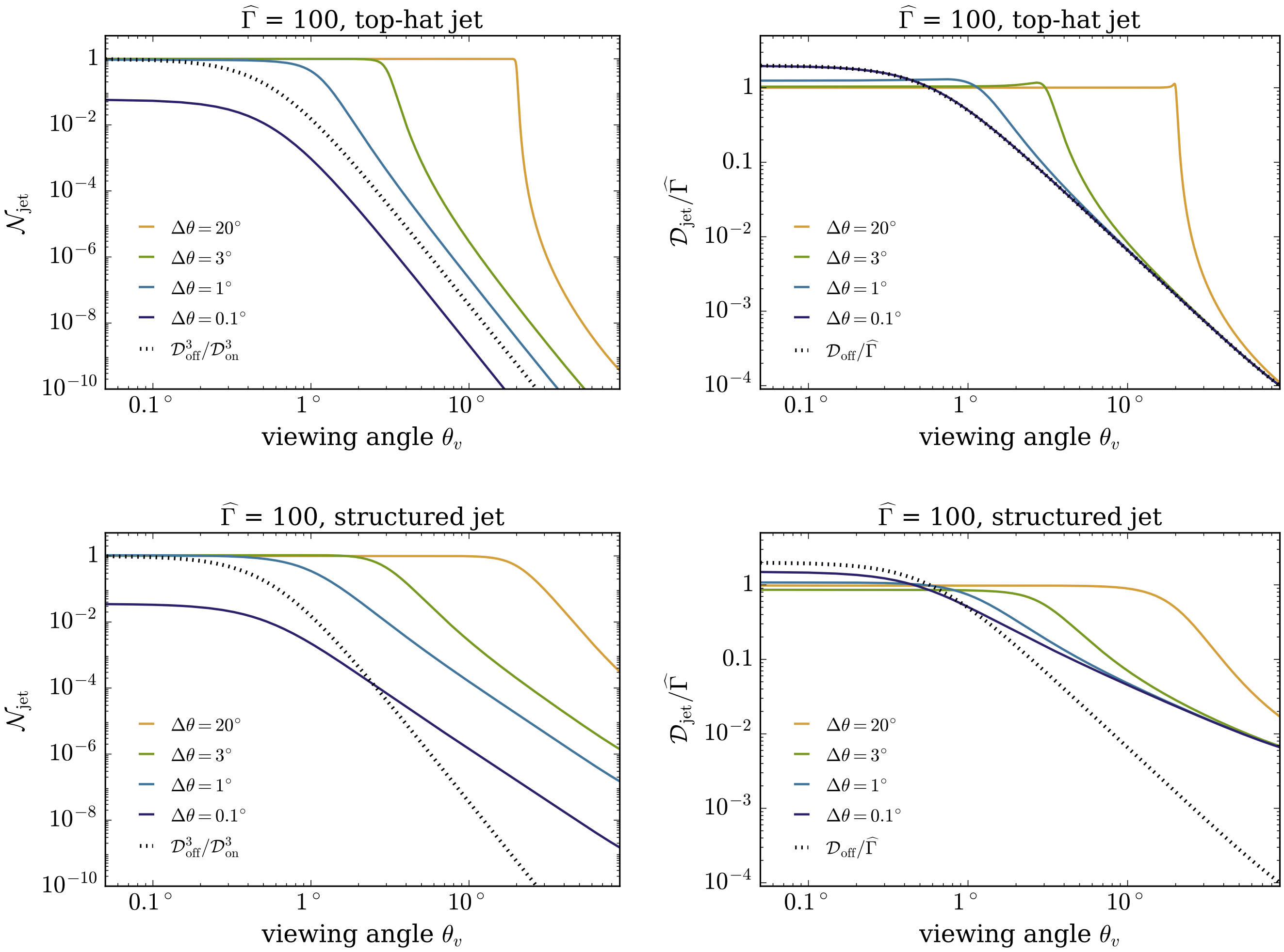

Figure 2. The scaling factor $\mathcal{N}_{\rm jet}$ (*left*) defined in Eq. (19) and effective Doppler factor $\mathcal{D}_{\rm jet}$ (*right*) defined in Eq. (22) for a top-hat jet (*top*) and a structured jet (*bottom*). The dotted lines in the plots indicate the expected scaling of $\mathcal{N}_{\rm jet}$ and $\mathcal{D}_{\rm jet}/\widehat{\Gamma}$ for a top-hat jet observed at a large viewing angle θ_v.

The top left panel of Fig. 2 show this normalization factor for a top-hat jet for a variable viewing angle. The asymptotic behavior of the top-hat jet can be easily understood: For an on-axis observer with $\theta_v \ll \Delta\theta$ and jet factor approaches a constant. For high Lorentz factors, $\Gamma\Delta\theta \gg 1$, the emission from the edge of the jet is subdominant and the jet factor reaches $\mathcal{N}_{\rm jet} \simeq 1$. The core energy $\widehat{E}$ is in this case equivalent to the isotropic-equivalent energy in the observer's frame. For low Lorentz factors, $\Gamma\Delta\theta \ll 1$, the edge of the jet becomes visible and the jet factor becomes $\mathcal{N}_{\rm jet} \simeq 2(\Gamma\Delta\theta)^2$. On the other hand, for off-axis emission with $\theta_v \gg \Delta\theta$ the jet factor reproduces the expected $\mathcal{D}^3_{\rm off}$-scaling of Eq. (10). The bolometric energy in the GRB and jet frame are related as $E^* = \Gamma E' \simeq (\Delta\Omega_{\rm jet}/4\pi)\widehat{E}$. For comparison, we show in the upper plot in Fig. 1 the naive scaling $(\mathcal{D}_{\rm off}/\mathcal{D}_{\rm on})^3$ expected from Eq. (10), not correcting for the jet opening angle.

The case of a structured jet is shown in the bottom left panel of Fig. 2. Similar to the case of the top-hat jet, at small viewing angles, $\theta_v \ll \Delta\theta$, the jet factor is independent of the viewing angle and reaches $\mathcal{N}_{\rm jet} \simeq 1$ if $\Gamma\Delta\theta \gg 1$. However, the behavior at a large viewing angle, $\theta_v \gg \Delta\theta$, becomes more complex. The scaling with θ_v is much shallower than $(\mathcal{D}_{\rm off}/\mathcal{D}_{\rm on})^3$ expected from Eq. (10) and a top-hat jet.

We can extend the scaling of the energy fluence (18) to that of the particle fluence F. The particle fluence observed at an energy ϵ is related to contributions across the shell at energy $\epsilon' = \epsilon(1+z)/\mathcal{D}$. The particle fluence F (in units of $\mathrm{GeV}^{-1}\mathrm{cm}^{-2}$) can then be derived following the same line of arguments used for the energy fluence and can be expressed as:

$$\epsilon^2 F(\epsilon) = \frac{1+z}{4\pi d_L^2}\int \mathrm{d}\Omega^* \frac{\mathcal{D}^3(\Omega^*)}{\Gamma(\theta^*)}\frac{\mathrm{d}E^*}{\mathrm{d}\Omega^*}\left[\frac{\epsilon'^2 n'(\theta^*,\epsilon')}{u'(\theta^*)}\right]_{\epsilon'=\epsilon\frac{1+z}{\mathcal{D}(\Omega^*)}}. \tag{20}$$

In the following we will assume that the internal spectrum only mildly varies across the sub-shell, $n'(\theta^*,\epsilon')/u'(\theta^*) \simeq n'(\epsilon')/u'$. We can then find an approximate solution to Eq. (20) of the form

$$\epsilon^2 F(\epsilon) \simeq \frac{1+z}{4\pi d_L^2}\mathcal{N}_{\rm jet}\widehat{E}\left[\frac{\epsilon'^2 n'(\epsilon')}{u'}\right]_{\epsilon'=\epsilon\frac{1+z}{\mathcal{D}_{\rm jet}}}, \tag{21}$$

where we define the average Doppler boost as

$$\mathcal{D}_{\rm jet}(\theta_v) \equiv \int \mathrm{d}\Omega^* \frac{\mathcal{D}^3(\Omega^*)}{\Gamma(\theta^*)}\frac{\mathrm{d}E^*}{\mathrm{d}\Omega^*}\Bigg/\int \mathrm{d}\Omega^* \frac{\mathcal{D}^2(\Omega^*)}{\Gamma(\theta^*)}\frac{\mathrm{d}E^*}{\mathrm{d}\Omega^*}. \tag{22}$$

Note that, by design, approximation (21) conserves the total energy *and* particle fluence from the source.

The right panels of Figure 2 show the normalized average Doppler factor $\mathcal{D}_{\rm jet}/\widehat{\Gamma}$ for the top-hat jet (*top*) and the

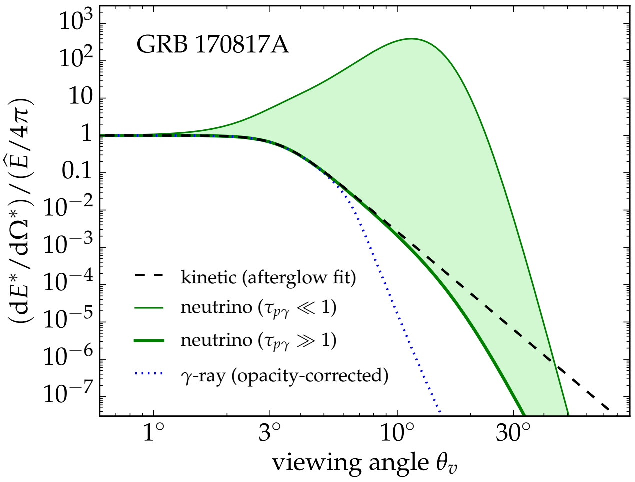

Figure 3. Relative angular distribution of the energy associated with the bulk flow (solid black line), neutrinos at low and high opacity (thin & thick green line), and γ-rays corrected for Thomson scattering in the shell (dotted blue line).

structured jet (*bottom*). For on-axis observation, $\theta_v \ll \Delta\theta$, the average Doppler factor becomes independent of viewing angle. For high Lorentz factors, $\Gamma\Delta\theta \gg 1$, it approaches the Lorentz factor in the jet center, $\mathcal{D}_{\rm jet} \simeq \widehat{\Gamma}$. Only for narrow jets, $\Gamma\Delta\theta \ll 1$, and on-axis views we approach the on-axis Doppler limit $\mathcal{D}_{\rm jet} \simeq 2\widehat{\Gamma}$.

Again, the off-axis emission, $\theta_v \gg \Delta\theta$, shows quite different asymptotic behaviors for the two jet structures. In the case of the top-hat jet (*top*) the average Doppler factor approaches the naive scaling with off-axis Doppler factor $\mathcal{D}_{\rm off}$. Narrow top-hat jets, $\Delta\theta\Gamma \ll 1$, can be well approximated by $\mathcal{D}_{\rm jet} \simeq \mathcal{D}_{\rm off}$ over the full range of viewing angles. For the structured jet (*bottom*) the scaling of $\mathcal{D}_{\rm jet}$ with large viewing angle does not follow the naive $\mathcal{D}_{\rm off}$ scaling and lead to significantly higher Doppler factor.

With the quantities $\mathcal{N}_{\rm jet}$ and $\mathcal{D}_{\rm jet}$ we can now provide a revised scaling relation for the off-axis particle fluence F (units of $\mathrm{GeV}^{-1}\mathrm{cm}^{-2}$):

$$F_{\rm off}(\epsilon) \simeq \frac{\mathcal{N}_{\rm jet}(\theta_v)}{\mathcal{N}_{\rm jet}(0)}\frac{1}{\eta^2}F_{\rm on}(\epsilon/\eta)\,. \tag{23}$$

Here, we define in analogy to Eq. (11) $\eta = \mathcal{D}_{\rm jet}(\theta_v)/\mathcal{D}_{\rm jet}(0)$, but in terms of the average Doppler factor in Eq. (22) for different observer locations. Many GRB calculations are based on the assumption of an on-axis observer of a uniform jet with wide opening angle. In this case the on-axis calculation is based on $\mathcal{N}_{\rm jet}(0) \simeq 1$ and $\mathcal{D}_{\rm jet}(0) \simeq \Gamma$, as can be seen in the top plots of Fig. 2. Note that for top-hat jets observed at a large viewing angle, $\theta_v \gg \Delta\theta$, the ratio of the jet factors approaches $\mathcal{N}_{\rm jet}(\theta_v)/\mathcal{N}_{\rm jet}(0) \simeq \eta^3$ (*cf.* top left panel of Fig. 2) and in this case Eq. (23) reproduces the naive scaling relation (11).

In principle, the scaling relation (23) applies to photon and neutrino predictions based on arbitrary jet structures and viewing angles. However, a crucial underlying assumption of the approximation (23) is that the relative emission spectrum only mildly varies across the sub-shell, $n'(\theta^*,\epsilon')/u'(\theta^*) \simeq n'(\epsilon')/u'$. We will see in the following that the emissivity of structured jets in the internal shock model can have strong local variations of magnetic fields and photon densities across the shock, which can jeopardize this condition. In this case, the calculation needs to be carried out using the exact expression (20).

4 NEUTRINO FLUENCE FROM STRUCTURED JETS

Internal shocks from colliding sub-shells of the GRB engine are expected to accelerate protons (and heavier nuclei) entrained in the GRB outflow. The spectrum of cosmic ray protons is assumed to follow a power-law close to ϵ_p^{-2} up to an effective cutoff that is determined by the relative efficiency of cosmic ray acceleration and competing energy loss processes. Based on the γ-ray fluence of the burst, one can estimate the internal energy densities of cosmic rays, photons and magnetic fields. The internal photon density allows to predict the opacity of individual sub-shells to proton-photon ($p\gamma$) interactions. Neutrino production follows predominantly from the production of pions, that decay via $\pi^+ \to \mu^+\nu_\mu$ followed by $\mu^+ \to e^+\nu_e\bar{\nu}_\mu$ or the charge-conjugate processes. The presence of strong internal magnetic fields leads to synchrotron loss of the initial protons and secondary charged particles before their decay. The mechanism was initially introduced by Waxman & Bahcall (1997) for the case of an on-axis jet with wide opening angle and has been studied in variations by several authors since (Guetta et al. 2004; Murase & Nagataki 2006; Anchordoqui et al. 2008; Ahlers et al. 2011; He et al. 2012; Zhang & Kumar 2013; Tamborra & Ando 2015; Denton & Tamborra 2018).

The energy densities of photons, magnetic fields, and cosmic rays are limited by the efficiency of internal collisions (IC) of merging sub-shells to convert bulk kinetic energy of the flow into total internal energy of the merged shell. In the rest frame of the central engine, we parametrize the total internal energy from the kinetic energy of the outflow via an angular-dependent efficiency factor $\eta_{\rm IC}$ as

$$\frac{\mathrm{d}E^*_{\rm IC}}{\mathrm{d}\Omega^*} = \eta_{\rm IC}(\theta^*)\frac{\mathrm{d}E^*}{\mathrm{d}\Omega^*}\,. \tag{24}$$

To first order, the efficiency of converting bulk kinetic energy into internal energy can be estimated by energy and momentum conservation (Kobayashi et al. 1997). In Appendix A we introduce a simple model of the efficiency factor as a function of the Lorentz factor $\Gamma(\theta^*)$ and the asymptotic efficiency η_∞ for large Lorentz factors. The partition of the internal energy into γ-rays, cosmic rays and magnetic fields is then parametrized as

$$\frac{\mathrm{d}E^*_x}{\mathrm{d}\Omega^*} = \varepsilon_x\frac{\mathrm{d}E^*_{\rm IC}}{\mathrm{d}\Omega^*}\,, \tag{25}$$

with the corresponding energy fraction ε_γ, ε_p and ε_B, respectively.

Using relation (9), we can express the internal photon energy density as

$$u'_\gamma(\theta^*) \simeq \frac{L^{\rm iso}_\gamma/\mathcal{N}_{\rm jet}(\theta_v)}{cr^2_{\rm dis}(\theta^*)\Gamma^2(\theta^*)}\frac{1}{\widehat{E}_\gamma}\frac{\mathrm{d}E^*_\gamma}{\mathrm{d}\Omega^*}\,, \tag{26}$$

where the isotropic-equivalent luminosity is defined by the γ−ray fluence as $L^{\rm iso}_\gamma \equiv 4\pi d_L^2\mathcal{F}_\gamma/T_{90}$. Neutrino production from $p\gamma$ interactions is determined by the opacity $\tau_{p\gamma} \simeq ct'_{\rm dyn}\sigma_{p\gamma}n'_\gamma$ of individual merging sub-shells. If we relate the shell position and width to the variability of the central engine (see Fig. 1) and assume that the γ-ray spectrum is observed at a peak photon energy $\epsilon_{\rm peak}$, we can express the $p\gamma$ opacity as

$$\tau_{p\gamma}(\theta^*) \simeq \frac{\sigma_{p\gamma}L^{\rm iso}_\gamma}{c^2\Delta t_{\rm eng}\epsilon_{\rm peak}}\frac{\mathcal{D}_{\rm jet}(\theta_v)}{\mathcal{N}_{\rm jet}(\theta_v)}\frac{1}{\Gamma^5(\theta^*)}\frac{1}{\widehat{E}_\gamma}\frac{\mathrm{d}E^*_\gamma}{\mathrm{d}\Omega^*}\,. \tag{27}$$

For an on-axis observer of a wide ($\Gamma\Delta\theta \gg 1$) jet this reduces to the familiar $\widehat{\Gamma}^{-4}$-scaling (Waxman & Bahcall 1997) since $\mathcal{D}_{\rm jet}(0) \simeq \Gamma$ and $\mathcal{N}_{\rm jet}(0) \simeq 1$ (see Fig. 2). Note that the opacity is independent of viewing angle; the appearance of the quantities $\mathcal{N}_{\rm jet}$ and $\mathcal{D}_{\rm jet}$, that strongly depend on jet structure and viewing angle, compensate the corresponding scaling of the peak emission energy $\epsilon_{\rm peak}$ and isotropic-equivalent luminosity $L_\gamma^{\rm iso}$ in the observer's frame. We can finally approximate the neutrino scaling with the jet angle as

$$\frac{{\rm d}E^*_\nu}{{\rm d}\Omega^*} \simeq \frac{3}{4}K_\pi\frac{\varepsilon_p}{\varepsilon_\gamma}\left(1-e^{-\kappa\tau_{p\gamma}(\theta^*)}\right)\frac{{\rm d}E^*_\gamma}{{\rm d}\Omega^*}\,. \tag{28}$$

Here we account for the inelasticity $\kappa \simeq 0.2$ of photo-hadronic interactions. The pre-factors in Eq. (28) accounts for the fraction of charged-to-neutral pions, $K_\pi \simeq 1/2$, and for three neutrinos carrying about 1/4th of the pion energy. The combination $\varepsilon_p/\varepsilon_\gamma$ corresponds to the non-thermal baryonic loading factor ξ_p, which we fix at $\xi_p \simeq 1$ in the following.

The formalism outlined here so far follows the standard approach of neutrino production in the internal shock model. The new aspect that we want to highlight is the angular distribution of total neutrino energy (28) in structure jet models. Depending on the opacity of the shell the neutrino scaling with jet angle becomes

$$\frac{{\rm d}E^*_\nu}{{\rm d}\Omega^*} \propto \begin{cases} \frac{{\rm d}E^*_{\rm IC}}{{\rm d}\Omega^*} & \tau_{p\gamma} \gg 1\,, \\ \frac{1}{\Gamma^5(\theta^*)}\left(\frac{{\rm d}E^*_{\rm IC}}{{\rm d}\Omega^*}\right)^2 & \tau_{p\gamma} \ll 1\,. \end{cases} \tag{29}$$

The strong angular dependence of neutrino emission in low opacity regions can have a significant influence on the neutrino predictions, as we will illustrate by the case of GRB 170817A in the following.

5 PROMPT EMISSION OF GRB 170817A

As an illustration of neutrino production in structured jets we will discuss the prompt emission of the recent short GRB 170817A observed in coincidence with the gravitational wave GW170817 from a binary neutron star merger (Abbott et al. 2017a,b). The spectrum observed with Fermi-GBM is best described as a Comptonized spectrum, $n_\gamma(\epsilon) \propto \epsilon^\alpha \exp(-(2+\alpha)\epsilon/\epsilon_{\rm peak})$, with spectral index $\alpha \simeq 0.14 \pm 0.59$ and peak photon energy $\epsilon_{\rm peak} \simeq (215 \pm 54)$ keV (Goldstein et al. 2017). The energy fluence integrated in the 10–1000 keV range is $\mathcal{F}_\gamma \simeq (1.4 \pm 0.3) \times 10^{-7}\,{\rm erg\,cm^{-2}}$. The source is located at a luminosity distance of $d_L \simeq 41$ Mpc corresponding to a redshift $z \simeq 0.01$. The variability of the central engine is $t_{\rm var} \simeq 0.125$s with an emission time of $T_{90} \simeq 2$s. From this we can calculate the isotropic-equivalent energy as $E_\gamma^{\rm iso} \simeq (2.8 \pm 0.6) \times 10^{46}$ erg.

Based on afterglow emission, Ghirlanda et al. (2019) derived a model for the angular dependence of the kinetic energy of the outflow, based on the parametrizations of Eqs. (16) and (17) with best-fit parameters $s_1 = 5.5$ and $s_2 = 3.5$, opening angle $\Delta\theta \simeq 3.4°$, core Lorentz factor $\widehat{\Gamma} \simeq 250$, core energy $\widehat{E} \simeq 2.5 \times 10^{52}$ erg and viewing angle $\theta_v \simeq 15°$. Alternative models of the outflows have been presented by Lazzati et al. (2018), Troja et al. (2018), Margutti et al. (2018), Lamb et al. (2019) or Lyman et al. (2018).

5.1 Gamma-Ray Fluence

Before we turn to the neutrino fluence, it is illustrative to compare the structured jet model of Ghirlanda et al. (2019) based on afterglow observations to the expected prompt γ-ray emission from the internal shock model. For this comparison it is crucial to account for angular-dependent internal photon absorption. The opacity of individual sub-shells with respect to Thompson scattering on baryonic electrons is given as $\tau_T \simeq ct'_{\rm dyn}\sigma_T n'_e$ with Thomson cross section $\sigma_T \simeq 0.67$ barn and local baryonic electron density

$$n'_e \simeq \frac{Y_e}{cr^2_{\rm dis}m_p\Gamma(\theta^*)}\left[\frac{1}{T_{\rm GRB}(\Gamma(\theta^*)-1)}\frac{{\rm d}E^*}{{\rm d}\Omega^*}\right]\,. \tag{30}$$

The term in square brackets correspond to the angular-dependent mass flow ${\rm d}\dot{M}/{\rm d}\Omega^*$ of the structured jet. For the proton fraction of the flow we assume $Y_e \simeq 1/2$ in the following. We can then account for γ-ray absorption by Thomson scattering as

$$\frac{{\rm d}E^*_{\rm GRB}}{{\rm d}\Omega^*} \simeq \frac{1-e^{-\tau_T(\theta^*)}}{\tau_T(\theta^*)}\frac{{\rm d}E^*_\gamma}{{\rm d}\Omega^*}\,. \tag{31}$$

Figure 3 shows this angular distribution of emitted γ-rays as a dotted blue line.

From this γ-ray emission model, we calculate a jet scaling factor $\mathcal{N}_{\rm jet} \simeq 1.4\times10^{-5}$ for a viewing angle $\theta_v \simeq 15°$. Following Eq. (18), the internal γ-ray energy at the jet core is therefore required to reach $\widehat{E}_\gamma \simeq (2.1 \pm 0.4) \times 10^{51}$ erg to be consistent with the fluence level observed by Fermi-GBM. Assuming an asymptotic efficiency factor $\eta_\infty \simeq 0.2$ in Eq. (24) we can estimate the total internal energy of the sub-shell at the jet center as $\widehat{E}_{\rm IC} \simeq 5 \times 10^{51}$ erg. This is consistent with the γ-ray observation if we require that an energy fraction of $\varepsilon_\gamma \simeq 0.41 \pm 0.09$ contributes to the γ-ray emission of the burst.

For the prediction of the corresponding neutrino fluence we have to make an assumption about the relative photon target spectrum $n'_\gamma(\theta^*,\epsilon')/u'_\gamma(\theta^*)$ at angular distance θ^* in the sub-shell. In general, we don't expect that the spectral features remain constant across the shell, owing to the strong local variations from synchrotron loss in magnetic fields and photon absorption via Thomson scattering. Indeed, the γ-ray emissivity at an assumed viewing angle of $\theta_v \simeq 15°$ is strongly suppressed by the opacity of the photosphere; *cf.* Fig. 3. To study the dependence of our neutrino fluence predictions on this model uncertainty we consider two scenarios. In both cases we assume that the internal photon spectrum follows a Comptonized spectrum with low-energy index $\alpha = 0.14$. For the exponential cutoff we assume:
(a) a *constant* co-moving peak

$$\epsilon'_{\rm peak}(\theta^*) \simeq \frac{215{\rm keV}}{\mathcal{D}_{\rm jet}} \simeq 75{\rm keV}\,, \tag{32}$$

where $\mathcal{D}_{\rm jet} \simeq 2.9$ is the average Doppler factor (22) based on the angular-dependent γ-ray emission (31) and
(b) a *scaled* co-moving peak

$$\epsilon'_{\rm peak}(\theta^*) \simeq 75{\rm keV}\frac{\Gamma(\theta_v)}{\Gamma(\theta^*)}\,, \tag{33}$$

which corresponds to a fixed peak position $\epsilon^*_{\rm peak} = \Gamma\epsilon'_{\rm peak}$ in the rest frame of the central engine.

These two models are chosen such that the internal γ-ray emissivity is consistent with the γ-ray spectrum of GRB 170817A observed by Fermi-GBM at a viewing angle of 15°. However, note that model *(a)* implies that the peak photon energy for the *on-axis* observations would reach energies $\epsilon_{\rm peak} \simeq 20$ MeV, in tension with the peak distribution inferred from GRBs observed by Fermi-GBM (Gruber et al. 2014). The phenomenological model *(b)* is motivated by the discussion of Ioka & Nakamura (2019), who study the consistency of the on-axis emission of GRB 170817A with the

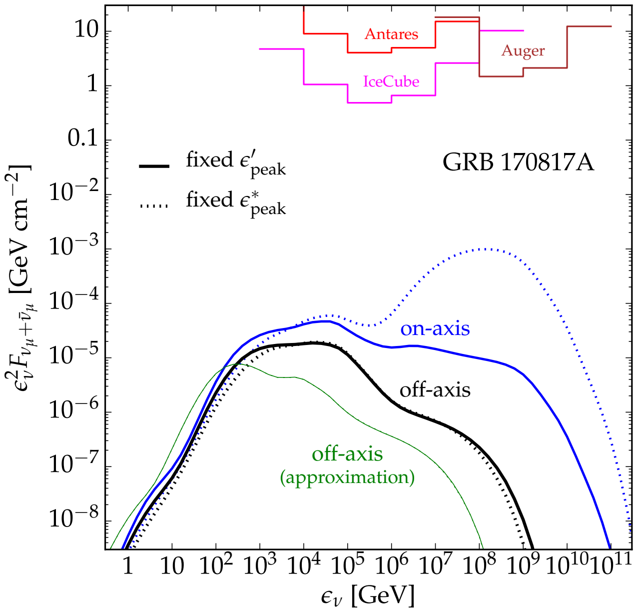

Figure 4. Predicted fluence of muon neutrinos ($\nu_\mu + \bar{\nu}_\mu$) associated with the prompt emission in the best-fit structured jet model of Ghirlanda et al. (2019). We show the predictions based on a fixed photon peak in the shell frame ("fixed ϵ'_{peak}", solid lines) using Eq. (32) and in the engine frame ("fixed ϵ^*_{peak}", dotted lines) using Eq. (33). The thick black lines show the off-axis emission at a viewing angle $\theta_v = 15°$. The blue lines show the corresponding prediction for the on-axis emission, which has a strong dependence on the internal photon spectrum. The thin green lines show the result of an approximation based on the standard on-axis calculation of uniform jets (Waxman & Bahcall 1997) with jet parameters from the structured jet model at $\theta^* = \theta_v$. The upper solid lines indicate the 90% C.L. upper limit on the fluence from Albert et al. (2017).

E_γ^{iso}-ϵ_{peak} correlation suggested by Amati (2006). Here, the on-axis fluence is expected to peak at $\epsilon_{\text{peak}} \simeq 178$ keV.

5.2 Neutrino Fluence

As we discussed in section 4, the neutrino emissivity of a structured jet is expected to deviate from the angular distribution of the observable γ-ray emission. For high opacity ($\tau_{p\gamma} \gg 1$) regions of the shell the angular distribution of the neutrino emission is expected to follow the distribution of internal energy (24) that takes into account the efficiency of dissipation in internal collisions. This is shown for our efficiency model (A6) as the thick green line in Fig. 4. For low-opacity ($\tau_{p\gamma} \gg 1$) regions, however, the energy distribution has an additional angular scaling from the opacity (27), as indicated by the thin green line. One can notice that a low opacity environment has an enhanced emission at jet angles 10°-20°, which is comparable to our relative viewing angle. Note that the angular distributions in Fig. 3 are normalized to the value at the jet core and do not indicate the absolute emissivity of neutrinos or γ-rays, which depend on jet angle θ^* and co-moving cosmic ray energy ϵ'_{p}.

At each jet angle θ^* we estimate the maximal cosmic ray energy based on a comparison of the acceleration rate to the combined rate of losses from synchrotron emission, $p\gamma$ interactions (Bethe-Heitler and photo-hadronic) and adiabatic losses. Our model predictions assume a magnetic energy ratio compared to γ-rays of $\xi_B = 0.1$ and a non-thermal baryonic loading of $\xi_p \simeq 1$ (see Appendix B). We calculate the neutrino emissivity $j'_{\nu_\alpha}(\theta^*, \epsilon'_\nu)$ from $p\gamma$ interactions with the photon background in sub-shells based on the Monte-Carlo generator `SOPHIA` (Mücke et al. 2000), that we modified to account for synchrotron losses of all secondary charged particles before their decay (Lipari et al. 2007). The uncertainties regarding the photon target spectrum are estimated in the following via the two models *(a)* and *(b)* of the peak photon energy.

The expected fluence of muon neutrinos ($\nu_\mu + \bar{\nu}_\mu$) under different model assumptions is shown in Fig. 4. The off-axis fluence at a viewing angle of $\theta_v \simeq 15°$ is indicated as thick black lines. The off-axis prediction has only a weak dependence on the angular scaling of the co-moving peak of the photon spectrum, Eqs. (32) or (33), as indicated as solid and dotted lines, respectively. This is expected from the normalization of the model to the observed γ-ray fluence under this viewing angle. For comparison, we also show in Fig. 4 an approximation (thin green lines) of the off-axis neutrino fluence based on the on-axis top-hat jet calculation with Lorentz factor and neutrino emissivity evaluated at $\theta^* \simeq \theta_v$. This approximation has been used by Biehl et al. (2018) to scale the off-axis emission of the structured jet. Note that this approximation significantly underestimates the expected neutrino fluence of GRB 170717A compared to an exact calculation.

Figure 4 also indicates the predicted neutrino fluence for an on-axis observer of the source located at the same luminosity distance. The extrapolated on-axis fluence shows a strong dependence on the model of the internal photon spectrum; model (33) predicts a strong neutrino peak at the EeV scale that exceeds the prediction of model (32) by two orders of magnitude. The relative difference of the neutrino fluence at the EeV scale follows from the ratio of $\epsilon'_{\text{peak}}(0)$ for the two models (32) and (32): For a fixed co-moving energy density of the shell, a lower peak photon energy corresponds to a higher photon density and also a higher threshold for neutrino production. One can also notice, that the on-axis neutrino fluence in the TeV range depends only marginally on the viewing angle. This energy scale is dominated by the emission of the jet at $\theta^* \simeq 10° - 20°$ and reflects the strong angular dependence of the neutrino emission in the rest frame of the central engine (*cf.* Fig. 3).

The upper thin solid lines in Fig. 4 show the 90% confidence level (C.L.) upper limits on the neutrino flux of GRB 170817A from Antares, Auger and IceCube (Albert et al. 2017). The predicted neutrino fluence is orders of magnitude below these combined limits. However, our neutrino fluence predictions are proportional to the non-thermal baryonic loading factor, and we assume a moderate value of $\xi_p = 1$ for our calculations. In any case, the predicted neutrino flux at an observation angle of 15° is many orders of magnitude larger than the expectation from an off-axis observation of a uniform jet.

6 CONCLUSIONS

In this paper, we have discussed the emission of neutrinos in the internal shock model of γ-ray bursts. The majority of previous predictions are based on the assumption of on-axis observations of uniform jets with wide opening angles. Here, we have extended the standard formalism of neutrino production in the internal shock model to account for arbitrary viewing angles and jet structures, parametrized by the angular distribution of kinetic energy and Lorentz factor of the outflow of the GRB engine.

One of the main results of this paper is a revised relation of the particle fluence between on- and off-axis observers given in Eq. (23) based on the exact scaling of the energy fluence given by Eq. (19) and an average Doppler factor defined by Eq. (23). This relation allows to rescale previous on-axis calculations for off-axis observers, assuming that the relative emission spectrum is independent on the jet angle, as expected for uniform jets. The particle fluence under general conditions can be derived from the exact expression (20).

We have shown that the neutrino emissivity of structured jets can exhibit a strong relative dependence on the jet angle compared to the emission of γ-rays. We have illustrated this dependence for the case of GRB 170817A assuming a structured jet model inferred from afterglow observations. We have shown that this model is consistent with the observed γ-ray fluence if we take into account photon absorption at large jet angles. We find that the predicted off-axis neutrino emission at about 15° is similar to the on-axis prediction in the TeV energy range and orders of magnitude larger than the expected fluence from an off-axis observation of a uniform jet.

ACKNOWLEDGEMENTS

The authors acknowledge support by Villum Fonden under project no. 18994.

REFERENCES

Aartsen M. G., et al., 2017, Astrophys. J., 843, 112
Abbasi R., et al., 2012, Nature, 484, 351
Abbott B. P., et al., 2017a, Astrophys. J., 848, L12
Abbott B. P., et al., 2017b, Astrophys. J., 848, L13
Ahlers M., Gonzalez-Garcia M. C., Halzen F., 2011, Astropart. Phys., 35, 87
Albert A., et al., 2017, Astrophys. J., 850, L35
Amati L., 2006, Mon. Not. Roy. Astron. Soc., 372, 233
Anchordoqui L. A., Hooper D., Sarkar S., Taylor A. M., 2008, Astropart. Phys., 29, 1
Beloborodov A. M., 2010, Mon. Not. Roy. Astron. Soc., 407, 1033
Biehl D., Heinze J., Winter W., 2018, Mon. Not. Roy. Astron. Soc., 476, 1191
Blandford R. D., Znajek R. L., 1977, Mon. Not. Roy. Astron. Soc., 179, 433
Blumenthal G. R., 1970, Phys. Rev., D1, 1596
Bustamante M., Ahlers M., 2019, Phys. Rev. Lett., 122, 241101
Denton P. B., Tamborra I., 2018, Astrophys. J., 855, 37
Eichler D., Levinson A., 2004, Astrophys. J., 614, L13
Eichler D., Livio M., Piran T., Schramm D. N., 1989, Nature, 340, 126
Ghirlanda G., et al., 2019, Science, 363, 968
Goldstein A., et al., 2017, Astrophys. J., 848, L14
Granot J., Piran T., Sari R., 1999, Astrophys. J., 513, 679
Granot J., Panaitescu A., Kumar P., Woosley S. E., 2002, Astrophys. J., 570, L61
Gruber D., et al., 2014, Astrophys. J. Suppl., 211, 12
Guetta D., Hooper D., Alvarez-Muniz J., Halzen F., Reuveni E., 2004, Astropart. Phys., 20, 429
He H.-N., Liu R.-Y., Wang X.-Y., Nagataki S., Murase K., Dai Z.-G., 2012, Astrophys. J., 752, 29
Hjorth J., Bloom J. S., 2012, CAPS, 51, 169
Hummer S., Baerwald P., Winter W., 2012, Phys. Rev. Lett., 108, 231101
Ioka K., Nakamura T., 2019, Mon. Not. Roy. Astron. Soc., 487, 4884
Ioka K., Murase K., Toma K., Nagataki S., Nakamura T., 2007, Astrophys. J., 670, L77
Kimura S. S., Murase K., Mészáros P., Kiuchi K., 2017, Astrophys. J., 848, L4
Kobayashi S., Piran T., Sari R., 1997, Astrophys. J., 490, 92
Lamb G. P., et al., 2019, Astrophys. J., 870, L15
Lazzati D., Begelman M. C., 2010, Astrophys. J., 725, 1137
Lazzati D., Perna R., Morsony B. J., López-Cámara D., Cantiello M., Ciolfi R., Giacomazzo B., Workman J. C., 2018, Phys. Rev. Lett., 120, 241103
Li Z., 2012, Phys. Rev., D85, 027301
Lipari P., Lusignoli M., Meloni D., 2007, Phys. Rev., D75, 123005
Lyman J. D., et al., 2018, Nat. Astron., 2, 751
Margutti R., et al., 2018, Astrophys. J., 856, L18
Mészáros P., Rees M. J., 1993, Astrophys. J., 405, 278
Mészáros P., Rees M. J., 1994, Mon. Not. Roy. Astron. Soc., 269, L41
Mészáros P., Rees M. J., Papathanassiou H., 1994, Astrophys. J., 432, 181
Mücke A., Engel R., Rachen J. P., Protheroe R. J., Stanev T., 2000, Comput. Phys. Commun., 124, 290
Murase K., Ioka K., 2013, Phys. Rev. Lett., 111, 121102
Murase K., Nagataki S., 2006, Phys. Rev., D73, 063002
Murase K., Ioka K., Nagataki S., Nakamura T., 2006, Astrophys. J., 651, L5
Nakamura T., Ioka K., 2001, Astrophys. J., 554, L163
Narayan R., Paczynski B., Piran T., 1992, Astrophys. J., 395, L83
Paczynski B., 1986, ApJ, 308, L43
Paczynski B., Xu G. H., 1994, Astrophys. J., 427, 708
Popham R., Woosley S. E., Fryer C., 1999, Astrophys. J., 518, 356
Rees M. J., Mészáros P., 1992, Mon. Not. Roy. Astron. Soc., 258, 41
Rees M. J., Mészáros P., 1994, Astrophys. J., 430, L93
Rees M. J., Mészáros P., 2005, Astrophys. J., 628, 847
Rybicki G. B., Lightman A. P., 1979, *Radiative processes in astrophysics*. Wiley, New York
Salafia O. S., Ghisellini G., Pescalli A., Ghirlanda G., Nappo F., 2015, Mon. Not. Roy. Astron. Soc., 450, 3549
Salafia O. S., Ghisellini G., Pescalli A., Ghirlanda G., Nappo F., 2016, Mon. Not. Roy. Astron. Soc., 461, 3607
Senno N., Murase K., Meszaros P., 2016, Phys. Rev., D93, 083003
Shemi A., Piran T., 1990, Astrophys. J., 365, L55
Tamborra I., Ando S., 2015, JCAP, 1509, 036
Troja E., et al., 2018, Mon. Not. Roy. Astron. Soc., 478, L18
Villar V. A., et al., 2017, Astrophys. J., 851, L21
Waxman E., 1995, Phys. Rev. Lett., 75, 386
Waxman E., Bahcall J. N., 1997, Phys. Rev. Lett., 78, 2292
Woods E., Loeb A., 1999, ApJ, 523, 187
Woosley S. E., 1993, Astrophys. J., 405, 273
Yamazaki R., Yonetoku D., Nakamura T., 2003, Astrophys. J., 594, L79
Zhang B., 2018, *The Physics of Gamma-Ray Bursts*. Cambridge University Press, UK
Zhang B., Kumar P., 2013, Phys. Rev. Lett., 110, 121101

APPENDIX A: EFFICIENCY OF INTERNAL SHOCKS

Two sub-shells emitted from the central engine at times $t_1 < t_2$ with Lorentz factors $\Gamma_1 < \Gamma_2$ will eventually collide. The efficiency of converting bulk kinetic energy into internal energy E' can be estimated by energy and momentum conservation (Kobayashi et al. 1997):

$$E_{\rm tot} = \Gamma_1 M_1 + \Gamma_2 M_2 = \Gamma(M + E'), \tag{A1}$$

$$P_{\rm tot} = \sqrt{\Gamma_1^2 - 1}M_1 + \sqrt{\Gamma_2^2 - 1}M_2 = \sqrt{\Gamma^2 - 1}(M + E')\,. \tag{A2}$$

The efficiency of energy dissipation in internal collisions (IC) is then defined as

$$\eta_{\rm IC} = 1 - \frac{\Gamma M}{E_{\rm tot}}\,. \tag{A3}$$

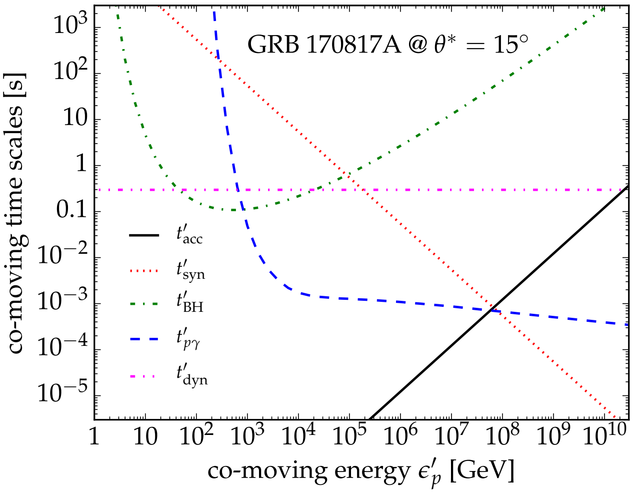

Figure A1. The acceleration time scale (solid) in comparison to the time scale of synchrotron loss (dotted), Bethe-Heitler pair production (dotted-dashed), hadronic interactions (dashed) and adiabatic losses (double-dotted-dashed) at jet angle $\theta^* \simeq 15°$.

In the relativistic limit, the Lorentz factor for the combined shells is

$$\Gamma \simeq \sqrt{\frac{\Gamma_1 M_1 + \Gamma_2 M_2}{M_1/\Gamma_1 + M_2/\Gamma_2}}\,. \tag{A4}$$

We will assume in the following that the variation of the central engine introduces variations in the energy of the form

$$\sqrt{E_{\rm tot}^2 - (\Gamma M)^2} \simeq x(\Gamma - 1)M\,, \tag{A5}$$

with $x = \mathcal{O}(1)$. In the relativistic limit and equal-mass shells, $M_1 \simeq M_2$, Eq. (A5) becomes equivalent to a condition on the variation of the Lorentz factors, $|\Gamma_2 - \Gamma_1| \simeq 2x\Gamma$, which is typically assumed in the internal shock model. On the other hand, Eq. (A5) ensures that the efficiency approaches zero for slow outflows in the tail of structured jets. The two Eqs. (A3) and (A5) define our model for the efficiency $\eta_{\rm IC}(\Gamma)$ of converting bulk kinetic energy to internal energy via colliding sub-shells. The efficiency rises with Γ and approaches the asymptotic value $\eta_\infty = 1 - 1/\sqrt{1+x^2}$ at high Lorentz factors. We can express the efficiency in terms of the combined Lorentz factor and the asymptotic efficiency as

$$\eta_{\rm IC}(\Gamma) = 1 - \frac{\Gamma}{\sqrt{2\Gamma - 1 + (\Gamma-1)^2/(1-\eta_\infty)^2}}\,. \tag{A6}$$

In this paper we will assume the asymptotic value $\eta_\infty \simeq 0.2$ that corresponds to $x \simeq 3/4$ in Eq. (A5).

APPENDIX B: COSMIC RAY SPECTRUM

We assume that cosmic ray protons in the sub-shell follow an $\epsilon_p'^{-2}$ spectrum with an exponential cutoff $\epsilon'_{p,\rm max}$. The jet model determines the local magnetic field and spectral photon density at different jet angles θ^*. Cosmic ray acceleration in internal shocks is expected to scale with the inverse of the Larmor radius or

$$t'^{-1}_{\rm acc} = \eta_{\rm acc}\frac{eB'}{\epsilon'_p}\,, \tag{B1}$$

where $\eta_{\rm acc}$ is the acceleration efficiency. In our calculation, we will assume high efficiencies of $\eta_{\rm acc} \simeq 1$. The maximal cosmic ray energy can be determined by comparing the acceleration rate to the combined rate of losses:
(i) Adiabatic cooling of the expanding shell can be estimated by the the dynamical time scale of the central engine,

$$t'^{-1}_{\rm dyn} = \frac{1}{\Gamma\Delta t_{\rm eng}}\,. \tag{B2}$$

(ii) The angular-averaged synchrotron loss of cosmic ray protons in the magnetized shell is given as

$$t'^{-1}_{\rm syn} = \frac{e^4 B'^2\epsilon'_p}{9\pi m_p^4}\,. \tag{B3}$$

(iii) The energy loss of $p\gamma$ interactions in the rest frame of the sub-shell is given by

$$t'^{-1}_{p\gamma} = \frac{\kappa}{2\gamma^2}\int {\rm d}\hat\epsilon\,\hat\epsilon\,\sigma_{p\gamma}(\hat\epsilon)\int_{\hat\epsilon/2\gamma}\frac{{\rm d}x}{x^2}n'_\gamma(x)\,, \tag{B4}$$

where κ is the average inelasticity of the interaction with background photons and $\hat\epsilon = \epsilon'_\gamma\gamma(1-\cos\theta)$ the photon's energy in the rest frame of the proton with Lorentz boost $\gamma \simeq \epsilon'_p/m_p$.
(iv) Bethe-Heitler (BH) e^+e^- pair production by cosmic ray scattering off background photons with time loss rate $t'^{-1}_{\rm BH}$ can be accounted for by the differential cross section calculated by Blumenthal (1970).

Our neutrino calculations are based on the Monte-Carlo generator `SOPHIA` (Mücke et al. 2000), that we modified to include synchrotron loss of *all* intermediate particles of the $p\gamma$-interaction cascade following Lipari et al. (2007). For a secondary particle with charge Z, mass m and proper lifetime τ_0, the ratio $x \equiv \epsilon'_f/\epsilon'_i$ of final to initial energy is following the probability distribution

$$p(x) = \frac{A}{x^3}\exp\left[\frac{A}{2}\left(1-\frac{1}{x^2}\right)\right]\,, \tag{B5}$$

with

$$A = \frac{9\pi}{(Ze)^4}\frac{m^5}{B'^2(\epsilon'_i)^2\tau_0}\,. \tag{B6}$$

After decay we determine the distribution functions ${\rm d}N/{\rm d}\epsilon$ of secondary neutrinos and nucleons (N). The local neutrino emissivity can the be estimated as

$$j'_{\nu_\alpha}(\epsilon'_\nu) \simeq \sum_\beta P_{\alpha\beta}\int {\rm d}\epsilon'_p\left(\frac{1-e^{-\kappa\tau_{p\gamma}}}{\kappa}\right)\frac{{\rm d}N_{\nu_\beta}}{{\rm d}\epsilon'_\nu}(\epsilon'_p,\epsilon'_\nu)j'_p(\epsilon'_p)\,. \tag{B7}$$

where $P_{\alpha\beta}$ is the oscillation-averaged probability matrix of neutrino flavor transitions; see, *e.g.*, Bustamante & Ahlers (2019). The inelasticity κ is here defined as

$$\kappa(\epsilon'_p) \equiv \int {\rm d}\epsilon''_N\frac{\epsilon'_p - \epsilon''_N}{\epsilon'_p}\frac{{\rm d}N_N}{{\rm d}\epsilon''_N}(\epsilon'_p,\epsilon''_N)\Big/\int {\rm d}\epsilon''_N\frac{{\rm d}N_N}{{\rm d}\epsilon''_N}(\epsilon'_p,\epsilon''_N)\,. \tag{B8}$$

The definition (B7) is consistent with energy relation of Eq. (28).

This paper has been typeset from a TEX/LATEX file prepared by the author.